KTH Engineering Sciences

Diode-pumped rare-earth-doped quasi-three-level lasers

Stefan Bjurshagen

Dissertation for the degree of Doctor of Technology

Department of Physics
Royal Institute of Technology

Stockholm, Sweden, November 2005

Laser Physics and Quantum Optics
Department of Physics
Royal Institute of Technology
Roslagstullsbacken 21
SE-106 91 Stockholm, Sweden

Akademisk avhandling som med tillstånd av Kungliga Tekniska Högskolan framlägges till offentlig granskning för avläggande av teknisk doktorsexamen i fysik, fredagen den 16 december 2005, kl. 10, sal FD 5, Albanova, Roslagstullsbacken 21. Avhandlingen kommer att försvaras på engelska.

TRITA-FYS 2005:70
ISSN 0280-316X
ISRN KTH/FYS/--05:70--SE
ISBN 91-7178-220-6

Diode-pumped rare-earth-doped quasi-three-level lasers

Printed by Universitetsservice US AB, Stockholm 2005

Bjurshagen, Stefan
Diode-pumped rare-earth-doped quasi-three-level lasers
Department of Physics, Royal Institute of Technology, SE-106 91 Stockholm, Sweden
TRITA-FYS 2005:70, ISSN 0280-316X, ISRN KTH/FYS/--05:70--SE, ISBN 91-7178-220-6

Abstract

Many rare-earth-doped materials are suitable for laser operation and this thesis focuses on diode-pumped solid-state lasers employing crystals doped with the trivalent rare-earth ions neodymium (Nd^{3+}), ytterbium (Yb^{3+}) and erbium (Er^{3+}). Especially, the quasi-three-level transitions in Nd and Yb have been studied as well as the eye-safe three-level transition around 1.5 μm in Er.

Quasi-three-level laser transitions in neodymium-doped crystals such as Nd:YAG, Nd:YLF and Nd:YVO_4 have received a great deal of interest because they allow for generation of blue light by frequency doubling. For solid-state blue laser sources, there exist numerous applications as in high-density optical data storage, colour displays, submarine communication and biological applications.

Efficient lasing on quasi-three-level transitions at 900–950 nm in Nd-doped crystals is considerably more difficult to achieve than on the stronger four-level transitions at 1–1.1 μm. The problems with these quasi-three-level transitions are a significant reabsorption loss at room temperature and a small stimulated emission cross section. This requires a tight focusing of the pump light, which is achieved by end-pumping with high-intensity diode lasers. Nd:YAG lasers at the 946 nm transition have been built and a maximum power of 7.0 W was obtained. By inserting a thin quartz etalon in the laser cavity, the 938.5 nm laser line could be selected and an output power of 3.9 W was then obtained.

By using nonlinear crystals, frequency-doubling of laser light at both 946 nm and 938.5 nm was achieved. Efficient generation of blue light at 473 nm has been obtained in periodically poled KTP, both in single-pass extra-cavity and intracavity configurations. More than 0.5 W was obtained at 473 nm by intracavity doubling. Intracavity second harmonic generation of the 938.5 nm transition gave slightly more than 200 mW at 469 nm.

During recent years, Yb-doped double-tungstate crystals like KGW and KYW have shown efficient laser operation. A comparative, experimental study of the laser performance and thermal-lensing properties between standard b-cut Yb:KGW and Yb:KGW cut along a novel athermal direction is presented. The results show that the thermal lens is about two times weaker and less astigmatic in the athermal-direction-cut crystal, for the same absorbed power. Also, Er-Yb-doped KGW and KYW have been investigated and the fluorescence dynamics have been measured for the Yb ($^2F_{5/2}$), Er ($^4I_{13/2}$) and Er ($^4S_{3/2}$) levels around 1 μm, 1.5 μm and 0.55 μm, respectively.

The influence of upconversion is a detrimental effect both in Nd-doped and Er-Yb-doped lasers. Analytical models starting from rate equations have been developed for these lasers including the influence of upconversion effects. The results of the general models have been applied to 946-nm Nd:YAG lasers and to Er-Yb-doped double-tungstate crystals in order to find the optimum doping concentrations for high gain for an eye-safe laser at 1.53 μm.

List of publications

I. S. Bjurshagen, D. Evekull, and R. Koch, "Generation of blue light at 469 nm by efficient frequency doubling of a diode-pumped Nd:YAG laser," Electron. Lett. **38**, 324–325 (2002).

II. S. Bjurshagen, D. Evekull, and R. Koch, "Efficient generation of blue light by frequency doubling of a Nd:YAG laser operating on $^4F_{3/2} \rightarrow {}^4I_{9/2}$ transitions," Appl. Phys. B **76**, 135–141 (2003).

III. S. Bjurshagen and R. Koch, "Modeling of energy-transfer upconversion and thermal effects in end-pumped quasi-three-level lasers," Appl. Opt. **43**, 4753–4767 (2004).

IV. S. Bjurshagen, R. Koch, and F. Laurell, "Quasi-three-level Nd:YAG laser under diode pumping directly into the emitting level," submitted to Opt. Commun., September 2005.

V. D. Evekull, S. Johansson, S. Bjurshagen, M. Olson, R. Koch, and F. Laurell, "Polymer encapsulated miniature Nd:YAG lasers," Electron. Lett. **39**, 1446–1448 (2003).

VI. D. Evekull, J. Rydholm, S. Bjurshagen, L. Bäcklin, M. Kindlundh, L. Kjellberg, R. Koch, and M. Olson, "High power Q-switched Nd:YAG laser mounted in a silicon microbench," Opt. Laser Tech. **36**, 383–385 (2004).

VII. J. E. Hellström, S. Bjurshagen, and V. Pasiskevicius, "Laser performance and thermal lensing in high-power diode pumped Yb:KGW with athermal orientation," submitted to Appl. Phys. B, October 2005.

VIII. S. Bjurshagen, J. E. Hellström, V. Pasiskevicius, M. C. Pujol, M. Aguiló, and F. Díaz, "Fluorescence dynamics and rate-equations analysis in Er^{3+}, Yb^{3+} doped double tungstates," submitted to Appl. Opt., November 2005.

Other publications, not included in this thesis

1. S. Bjurshagen, D. Evekull, F. Öhman, R. Koch, "High power diode-pumped Nd:YAG laser at 946 nm and efficient extra-cavity frequency doubling in periodically poled KTP," in *Conference Digest of CLEO/Europe-EQEC*, (Munich, Germany, 2001), p. 145.

2. S. Bjurshagen, D. Evekull, R. Koch, "Diode-pumped cw Nd:YAG laser operating at 938.5 nm and efficient extra-cavity frequency doubling," in *Advanced Solid-State Lasers*, M. E. Fermann and L. R. Marshall, eds., Vol. 68 of OSA Trends in Optics and Photonics (Optical Society of America, Washington D.C., 2002), pp. 37–40.

3. S. Bjurshagen, D. Evekull, R. Koch, "200 mW of blue light generated by intracavity frequency doubling of a diode-pumped Nd:YAG laser operating at 938.5 nm," in *Technical Digest of Conference on Lasers and Electro-Optics* (Long Beach, Calif., 2002), p. 92.

4. S. Bjurshagen, "Optimisation of 946 nm Nd:YAG lasers under direct pumping at 885 nm," in *EPS-QEOD Europhoton Conference* (Lausanne, Switzerland, 2004), paper WeC10.

5. S. Bjurshagen, F. Laurell, R. Koch, and H. J. Hoffman, "946-nm Nd:YAG laser under ground-state direct diode-pumping at 869 nm," in *Conference on Lasers and Electro-Optics* (Baltimore, Maryland, 2005), paper CMS4.

6. S. Bjurshagen, F. Laurell, R. Koch, and H. J. Hoffman, “946-nm Nd:YAG laser under direct diode-pumping at 869 nm,” in *CLEO/Europe-EQEC Conference* (Munich, Germany, 2005), paper CA2-4-MON.

7. Å. Claesson, J. Holm, M. Olson, C. Vieider, H. Åhlfeldt, S. Bjurshagen, L. Bäcklin, A. Olsson, R. Koch, F. Laurell, “Novel design for diode-pumped miniature lasers using microstructured silicon carriers,” in *Advanced Solid-State Lasers*, H. Injeyan, U. Keller, and C. Marshall, eds., Vol. 34 of OSA Trends in Optics and Photonics (Optical Society of America, Washington D.C., 2000), pp. 650–654.

8. D. Evekull, S. Bjurshagen, M. Gustafsson, L. Kjellberg, R. Koch, M. Olson, “Polymer encapsulated diode pumped Nd:YAG lasers,” in *Conference Digest of CLEO/Europe-EQEC*, (Munich, Germany, 2003), paper CA7-6-WED.

9. S. Johansson, S. Bjurshagen, F. Laurell, R. Koch, and H. Karlsson, “Advanced technology platform for miniaturised diode-pumped solid-state lasers,” in *EPS-QEOD Europhoton Conference* (Lausanne, Switzerland, 2004), paper FrB6.

10. J. E. Hellström, S. Bjurshagen, V. Pasiskevicius, and F. Laurell, “Experimental investigation of the athermal orientation in Yb:KGW,” in *Advanced Solid-State Photonics* (Lake Tahoe, Nevada, 2006), accepted October 2005.

Preface

When I started at Acreo in January 2001, it was to work with diode-pumped solid-state lasers (DPSSL) for high-power generation of blue light. The project was financed by The Knowledge Foundation (Stiftelsen för kunskaps- och kompetensutveckling). Most of the work on Nd:YAG lasers and blue light generation, which is the basis of this thesis was done in 2001 and the spring 2002. Then, thanks to KTH and the EU-project DT-CRYS, I could continue my research on solid-state lasers with a new direction into tungstate crystals in 2004 and 2005. The work at KTH has been supported in part by DT-CRYS, the Göran Gustafsson Foundation, the Carl Trygger Foundation and the Lars Hiertas Minne Foundation.

First of all, I would like to thank my supervisors: Ralf Koch, whose inspiring description of the project made me take the decision to start at Acreo and for always being supporting and encouraging during his management of the DPSSL activities at Acreo. Many thanks to Valdas Pasiskevicius for all the help in our work on tungstates and for discussions on physics and experiments, I have learnt a lot from you. Thanks to Fredrik Laurell for being my supervisor and for accepting me as a Ph.D. student in the autumn 2003 when times were tough at Acreo, and for the financial support from his group in 2004–2005.

Thanks to David Evekull for being my closest collaborator in the laboratory at Acreo and a good friend. Jacob Rydholm was also a good co-worker in the lab during his time at Acreo. At all times, Leif Kjellberg was always willing to solve any electronic or mechanical problem, and Sven Bolin did much mechanical work in his workshop.

Thanks to all people I have met during my time at Acreo, the “old” Photonics department with Ola Gunnarsson, Fredrik Carlsson, Niklas Myrén, Tove Gustavi, Åsa Claesson, Ingemar Petermann, Misha Popov and many more, the people at the old MIC department, the “new” Photonics department and everybody else.

Thanks to all the people at the Laser Physics group at KTH for making my time here pleasant: Jonas Hellström, Sandra Johansson, Anna Fragemann, Björn Jacobsson, Micke Tiihonen, Stefan Holmgren, Pär Jelger, Marcus Alm, Stefano Bertani, Junji Hirohashi, Carlota Canalias, Shunhua Wang and Stefan Spiekermann. A special thank to Jens Tellefsen for reading and improving this thesis.

Finally, thanks to my family with my father, mother and sister and to Jessica and Jennika, I love you!

Contents

1 Introduction

1.1 Rare-earth-doped solid-state lasers

Rare-earth ions incorporated in solids (crystals or glass) have the characteristics that optical transitions can take place between states of inner incomplete states. Many of these materials are suitable for laser operation, as they show sharp fluorescence lines in the spectra due to the fact that electrons involved in the optical transitions are shielded by the outer shells from the surrounding crystal lattice. Particularly important features of rare-earth-doped crystals are long radiative lifetimes and high absorption and stimulated-emission cross sections.

This thesis focuses on diode-pumped solid-state lasers in crystals doped with trivalent rare-earth ions such as neodymium (Nd^{3+}), ytterbium (Yb^{3+}) and erbium (Er^{3+}). It includes two major topics: first, the quasi-three-level transition in Nd:YAG and its frequency doubling to blue light, and second, Yb-doped and Er-Yb-doped double-tungstate crystals $KRE(WO_4)_2$ (RE = rear earths such as Y and Gd) for efficient 1-µm laser operation and spectroscopic investigations for 1.5-µm eye-safe lasers, respectively.

Throughout this work, a deeper insight of the experimental results have been achieved by developing theoretical models starting from rate-equations for the quasi-three-level transitions in Nd and Yb and the eye-safe three-level transition in Er, respectively.

1.2 Quasi-three-level neodymium lasers for blue light generation

After the laser was invented in 1960, a variety of applications emerged in the next decades that needed lasers at different wavelengths. However, some applications lacked a powerful, compact, inexpensive source of light in the blue portion of the spectrum. The first blue sources, gas lasers such as argon ion, could not satisfy the requirements of every application. Some applications required a wavelength that was not available from the fixed-wavelength gas lasers, other applications required a degree of tunability. In addition, the gas lasers had very low power efficiency. In the 1980s, the development of high-power semiconductor diode lasers at wavelengths around 810 nm opened up the possibility of efficient diode-pumping of solid-state lasers, such as those based on neodymium-doped crystals. Quasi-three-level lasers in Nd-doped crystals such as Nd:YAG, Nd:YLF and $Nd:YVO_4$ have received a great deal of interest because they allow for generation of blue light by frequency doubling [1–4]. In this thesis, high-power quasi-three-level lasers in Nd:YAG have been realised and then frequency-doubled to blue lasers. The highest blue output power achieved in solid-state lasers that has been published so far is 2.8 W [4].

For solid-state blue laser sources, there exist numerous applications [5] as in:

high-density optical data storage,

reprographic applications, where the laser is used to mark a medium as the photoconductor of a laser printer, or photographic film or paper,

colour displays, where red, green and blue lasers are attractive light sources because of their high brightness and complete colour saturation,

submarine communications, as seawater has a minimum attenuation for light at around 450 nm,

spectroscopic applications, for example laser cooling or process control of physical vapour deposition (PVD),

biotechnology, for example flow cytometry and DNA sequencing.

Efficient lasing on quasi-three-level transitions ($^4F_{3/2} \rightarrow {}^4I_{9/2}$) at 900–950 nm in Nd-doped crystals is considerably more difficult to achieve than on the stronger four-level transitions ($^4F_{3/2} \rightarrow {}^4I_{11/2}$) at 1–1.1 µm. The problems with these quasi-three-level transitions

are a significant reabsorption loss at room temperature and a very small stimulated emission cross section [1,2]. This requires a tight focusing of the pump light, which is achieved by end-pumping with high-intensity diode lasers.

In Chapter 2, the rate equations for four-level lasers and quasi-three-level lasers are derived. A number of papers [6–11] have shown that the influence of energy-transfer upconversion (ETU) is a detrimental effect in Nd-doped lasers. The ETU process involves two nearby ions in the $^4F_{3/2}$ upper laser level. One ion relaxes down to a lower lying level and transfers its energy to the other ion, which is thereby raised (upconverted) to a higher level. Consequently, ETU reduces the population of the upper laser level, hence degrading the laser performance. Due to the low gain, the degradation is more pronounced in quasi-three-level lasers. Therefore, an analytical model of the output performance of continuous-wave quasi-three-level lasers including the influence of energy-transfer upconversion was developed (Papers II and III). Starting from a rate equation analysis, the results of the general output modelling are applied to a laser with Gaussian beams, where results of the output performance in normalised parameters are derived. Especially, the influence of pump and laser mode overlap, reabsorption loss and upconversion effects on threshold, output power and spatial distribution of the population-inversion density is studied in Chapter 3. The presence of ETU effects also gives rise to extra heat load in the laser crystal due to the multiphonon relaxation from the excited level back to the upper laser level. The influence of ETU on the fractional thermal loading is modelled and studied under lasing conditions for different mode overlaps. Finally, the model is applied to a diode-pumped laser operating at 946 nm in Nd:YAG (Chapter 4), where the output power, thermal lensing and the degradation in beam quality are calculated. The dependence of the laser-beam size is investigated in particular, and a simple model for the degradation of laser beam quality from a transversally varying saturated gain is proposed.

Various resonator designs proposed to reduce the dependence of the thermal effects and to optimise the laser-beam size were evaluated. As highest, a multimode laser power of 7.0 W at 946 nm was obtained (Paper II). With another design, better beam quality was achieved (M^2 = 1.7) with an output power of 5.8 W. By inserting a thin quartz etalon, the 938.5 nm laser line could be selected (Paper I). An output power of 3.9 W with beam quality M^2 = 1.4 was then obtained.

By using nonlinear crystals, frequency-doubling of laser light at both 946 nm and 938.5 nm was achieved. Second harmonic generation (SHG) of the 946 nm transition gives blue light at 473 nm. Efficient generation of blue light has been achieved in periodically poled KTP, both in single-pass and intracavity configurations (Chapter 5). More than 0.5 W was obtained at 473 nm by intracavity doubling. Intracavity SHG of the 938.5 nm transition gave slightly more than 200 mW at 469 nm.

1.3 Nd:YAG lasers

The Nd:YAG crystal is a commonly used active medium for solid-state lasers, because of its high gain and good thermal and mechanical properties. The $Y_3Al_5O_{12}$ (yttrium aluminium garnet) host is hard, of good optical quality and has a high thermal conductivity. The cubic structure of YAG favours a narrow fluorescent linewidth, which results in high gain and low threshold for laser operation.

The strongest laser line in Nd:YAG is the four-level transition at 1064 nm as shown in Fig. 1.1. In a four-level system, the active ions (Nd^{3+} in this case) are excited from the ground state to the broad absorption band $^4F_{5/2}$ by the pump light at 808 nm. They then rapidly relax via multiphonon emission through nonradiative processes to the sharp upper metastable laser level $^4F_{3/2}$. The laser transition then proceeds to the lower laser level $^4I_{11/2}$, while photons are

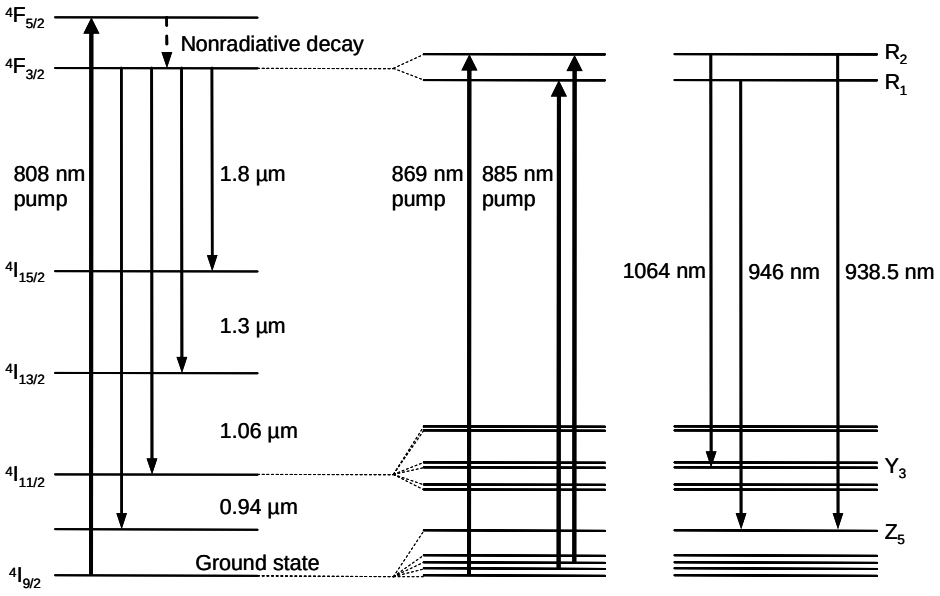

Fig. 1.1. Energy level scheme of Nd:YAG.

emitted. From here, the ions will again rapidly relax to the ground state. In order to get amplification of light by stimulated emission through the crystal, there have to be more ions in the upper laser level than in the lower, that is inverted population must be reached. In a four-level laser, the ions in the lower level are almost immediately transferred to the ground state. Inverted population is then reached as soon as there are ions in the upper level and the pump power needed to start the lasing process is low; the laser has a low threshold.

There are also three-level lasers (for example ruby), where the lower laser level is the same as the ground state, which is almost completely filled at thermal equilibrium. Intense pumping must therefore be used to reach threshold. Another type is the quasi-three-level laser, where the lower laser level is close to the ground state and thermally populated. The pump power needed to reach threshold is, however, much lower than for three-level-lasers. Efficient lasing on the quasi-three-level transitions ($^4F_{3/2} \rightarrow {}^4I_{9/2}$) at 900–950 nm in Nd-doped crystals is considerably more difficult to achieve than on the stronger four-level transitions ($^4F_{3/2} \rightarrow {}^4I_{11/2}$) at 1–1.1 µm. The problems with these quasi-three-level transitions are a significant reabsorption loss at room temperature and a very small stimulated emission cross section. This requires a tight focusing of the pump light, which is achieved by end-pumping with high-intensity diode lasers. An example of a quasi-three-level transition that can be used is the $^4F_{3/2} \rightarrow {}^4I_{9/2}$ transition at 946 nm in Nd:YAG (Fig. 1.1). The upper laser level is the lower (R_1) of the two crystal-field components of the $^4F_{3/2}$ level, and the lower laser level is the uppermost (Z_5) of the five crystal-field components of the $^4I_{9/2}$ level.

Traditional pumping at 808 nm into the $^4F_{5/2}$ pump band, above the upper laser level $^4F_{3/2}$, induces a parasitic quantum defect between the pump and the emitting laser levels. On the other hand, resonant pumping directly into the emitting level at either 869 nm (ground-state direct pumping) or 885 nm (thermally boosted pumping from thermally excited ground-state levels) reduces the total quantum defect between the pump and laser emission wavelengths (Fig. 1.1). This leads to a decrease in the heat generated in the laser material, thus reducing the thermal effects induced by optical pumping. Direct pumping at 869 nm of a quasi-three-level laser at 946 nm has been investigated in Paper IV.

1.4 Nonlinear materials and second harmonic generation

By using nonlinear crystals, frequency-doubling of laser light is possible and SHG of the 946 nm transition in Nd:YAG gives blue light at 473 nm. Quasi-phasematched (QPM) crystals are nonlinear materials that can be designed for SHG to arbitrary wavelengths within the crystal transparency range. QPM materials have been developed using periodic electric field poling of ferroelectrics, such as potassium titanyl phosphate ($KTiOPO_4$). Efficient generation of blue light has been made in periodically poled KTP, both in single-pass and in intracavity configurations (Chapter 5).

1.5 Miniature lasers using micro-structured carriers

As it is a goal to make the lasers compact, miniature Nd:YAG lasers in micro-structured carriers have been developed. Monolithic microchip lasers are compact, miniaturised lasers in a crystal or glass medium of lengths of a few millimetres. They have a flat-flat cavity with mirrors deposited directly on the crystal surfaces. As the cavity is flat-flat and no beam-shaping elements are present in the cavity that can confine the beam, the stability of the laser resonator will be determined by thermal effects and gain gradients. An optical microbench has been developed in collaboration between Acreo and KTH (Chapter 6). It consists of an etched V-groove in a silicon carrier, where laser crystals diced in rhombic shapes from mirror-coated wafers are used. Recently, this concept was expanded to carriers in polymer materials.

1.6 Q-switching

In the microbench concept (Chapter 6), Cr:YAG saturable absorbers were included for Q-switched laser operation. Q-switching is used to achieve giant laser pulses in a cavity. This is achieved by blocking the cavity from lasing through introduction of losses so that the laser threshold cannot be reached. The energy is stored as excited electrons until, suddenly, the losses are removed. Then, the gain, which is very high, will build up an oscillating field in the cavity. A passive Q-switch consists of a saturable absorber (for example Cr:YAG) in the resonator. As the energy builds up in the laser crystal, the laser approaches the threshold condition despite the extra losses introduced by the absorber. In the cavity, a weak field starts to build up, which successively becomes strong enough to bleach the saturable absorber to high transmission, releasing the pulse.

1.7 Double-tungstate laser materials

In an EU project, DT-CRYS (www.dt-crys.net), rare-earth-doped double-tungstate crystals $KRE(WO_4)_2$ (RE = rare earths like Gd, Y and Yb) have been studied. Our part at KTH has so far involved KGW and KYW doped by Er and Yb. The crystals have been grown by our EU-project partner at Universitat Rovira i Virgili (URV) in Tarragona (Chapter 7).

1.8 Ytterbium lasers

Like the 946-nm Nd:YAG laser, Yb^{3+}-doped hosts are quasi-three-level systems, but the energy-level diagram is very simple and consists of only two manifolds: the $^2F_{7/2}$ ground state and the $^2F_{5/2}$ excited state. With pump diodes around 940 nm and 980 nm, Yb-doped materials like Yb:YAG are used for highly efficient laser systems. The laser wavelength is around 1.03 µm, which gives a very small quantum defect and together with the absence of upconversion and excited state absorption, this can result in high slope efficiencies.

During recent years, a substantial interest has been shown in Yb^{3+}-doped double-tungstate crystals like KGW and KYW. The double-tungstate crystals exhibit an attractive set of parameters, which makes them one of the best choices for laser-diode end-pumped solid-

state lasers operating around 1 μm. Experiments with diode-pumped Yb:KGW lasers are described in Chapter 8 and Paper VII, where especially a laser crystal with a novel athermal orientation has been utilised.

1.9 Erbium-ytterbium eye-safe lasers

Erbium-doped solid-state lasers are widely used for generation of light in the eye-safe region around 1.5 μm. There are many applications including range finding, remote sensing, optical fibre communication, medicine and meteorology. As erbium-doped crystals operate as three-level lasers and have a rather poor absorption at pump-diode wavelengths around 980 nm, the laser efficiency is reduced, and for this reason, sensitiser ions such as ytterbium are added to the material which increase the pump absorption and, via excitation transfer to the erbium ions, will improve the laser performance. So far, the Er-Yb-doped phosphate glass has been the most efficient laser host in the 1.53 μm wavelength region. However, the phosphate glass is far from a perfect laser material. The main limitations are low thermal conductivity, low threshold for thermal stress-induced fracture as well as relatively low absorption and stimulated-emission cross sections for the Yb^{3+} and Er^{3+} ions, respectively.

For comparison, Er-Yb-doped double-tungstate crystals such as KGW and KYW offer definite advantages with respect to all these parameters, in particular when considering that the Yb^{3+} absorption cross section is an order of magnitude larger and that the Er^{3+} emission cross section is about twice as large in double tungstates than in phosphate glass. On the other hand, the spectroscopic properties and the dynamics in the Er^{3+}, Yb^{3+} system are substantially different in double-tungstate crystals. In Paper VIII described in Chapter 9, the objective is to find the optimum doping concentrations in double tungstates for eye-safe lasers. This objective is achieved by first investigating the relevant spectroscopic and dynamic properties of the Er^{3+}, Yb^{3+} system in double-tungstate hosts. This involves an experimental study of the excitation dynamics in the crystals with a variety of doping concentrations, which will allow us to deduce relevant dynamic parameters for a theoretical rate-equation model. As in Nd-doped materials, there are also upconversion processes present in Yb-Er systems. Upconversion processes result in strong green fluorescence at 0.55 μm, and these processes are especially studied and included in the modelling. As the excitation transfer from Yb reaches a level in Er with relatively long nonradiative lifetime, back transfer and the upconversion processes play an important role, degrading the laser performance. This makes it very challenging to find the optimum doping concentrations in these materials for high laser gain for the eye-safe transition at 1.53 μm.

2 Theoretical modelling of solid-state lasers

2.1 Introduction

In this chapter I will outline the basic theory of solid-state lasers and derive some useful equations for continuous wave four-level and quasi-three level lasers. The derivation follows textbooks by Siegman [12], Yariv [13] and Koechner [14]. Eventually, the model is extended to include the effect of energy-transfer upconversion for a diode-pumped quasi-three-level laser, and results are derived for threshold, output power, fractional thermal loading and thermal lensing.

Electrons in atomic systems such as atoms, ions and molecules can exist only in discrete energy states. A transition from one energy state to another is associated with either the emission or absorption of a photon. The frequency ν of the absorbed or emitted radiation is given by Bohr's frequency relation

$$E_2 - E_1 = h\nu, \tag{2.1}$$

where E_2 and E_1 are two discrete levels and h is Planck's constant. In solid-state lasers, the energy levels and the associated frequencies result from the different quantum energy levels or allowed quantum states of the electrons orbiting about the nuclei of atoms.

By combining Planck's law and Boltzmann statistics, Einstein could formulate the concept of stimulated emission. When electromagnetic radiation in an isothermal enclosure, or cavity, is in thermal equilibrium at temperature T, the distribution of blackbody radiation density is given by Planck's law:

$$\rho(\nu) = \frac{8\pi n^3 h\nu^3}{c^3} \frac{1}{e^{h\nu/kT} - 1}, \tag{2.2}$$

where $\rho(\nu)$ is the radiation density per unit frequency [Js/cm^3], k is Boltzmann's constant, c is the velocity of light in vacuum and n is the refractive index of the medium. When a large collection of similar atoms is in thermal equilibrium, the relative populations of any two energy levels E_1 and E_2 (as in Fig. 2.1) are related by the Boltzmann ratio

$$\frac{N_2}{N_1} = \frac{g_2}{g_1} \exp(-(E_2 - E_1)/kT), \tag{2.3}$$

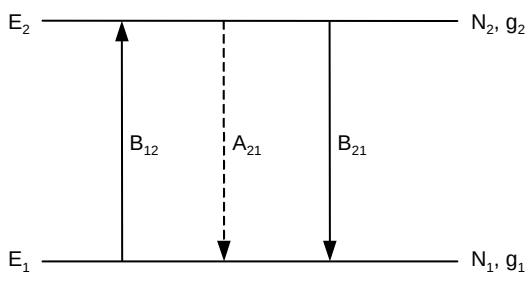

Fig. 2.1. Two energy levels with population N_1, N_2 and degeneracies g_1, g_2, respectively.

where N_1 and N_2 are the number of atoms in the energy levels E_1 and E_2, respectively. When two or more states have the same energy E_i, they are degenerated and the degeneracy g_i of the ith energy level must be taken into account.

2.2 Einstein's coefficients

We will now introduce the concept of Einstein's A and B coefficients for an idealised material with two energy levels. The total number of atoms in these two levels is assumed to be constant $N_1 + N_2 = N_{\text{tot}}$. We can identify three types of interaction between electromagnetic radiation and the two-level system:

Absorption. If electromagnetic radiation of frequency ν passes through an atomic system with energy gap $h\nu$, then the population of the lower level will be depleted proportional both to the radiation density $\rho(\nu)$ and to the lower level population N_1

$$\frac{dN_1}{dt} = -B_{12}\rho(\nu)N_1, \tag{2.4}$$

where B_{12} is a constant with dimensions cm^3/s^2 J.

Spontaneous emission. After an atom has been raised to the upper level by absorption, the population of that level decays spontaneously to the lower level at a rate proportional to N_2

$$\frac{dN_2}{dt} = -A_{21}N_2, \tag{2.5}$$

where A_{21} is a constant with dimensions s^{-1}. The phase of spontaneous emission is independent of that of the external radiation; the photons emitted are incoherent. Equation (2.5) has the solution

$$N_2(t) = N_2(0)\exp(-t/\tau_{21}), \tag{2.6}$$

where $\tau_{21} = A_{21}^{-1}$ is the lifetime for spontaneous radiation from level 2 to level 1.

Stimulated emission. Emission also takes place under stimulation by electromagnetic radiation of frequency ν and the upper level population N_2 decreases according to

$$\frac{dN_2}{dt} = -B_{21}\rho(\nu)N_2, \tag{2.7}$$

where B_{12} is a constant. The phase of the stimulated emission is the same as that of the stimulating external radiation. The photon emitted to the radiation field by the stimulated emission is coherent with it. The useful parameter for laser action is the B_{21} coefficient, whereas the A_{21} coefficient introduces photons that are not phase-related to the incident photons. Spontaneous emission represents a noise source in a laser.

If absorption, spontaneous and stimulated emission are combined, the resulting rate equation for the two-level model is

$$\frac{dN_1}{dt} = -\frac{dN_2}{dt} = -B_{12}\rho(\nu)N_1 + A_{21}N_2 + B_{21}\rho(\nu)N_2. \tag{2.8}$$

In thermal equilibrium

$$\frac{dN_1}{dt} = -\frac{dN_2}{dt} = 0\,, \tag{2.9}$$

and using the Boltzmann equation (2.3) gives

$$\rho(\nu) = \frac{A_{21}/B_{21}}{(g_1/g_2)(B_{12}/B_{21})e^{h\nu/kT} - 1}\,.$$

Comparing this expression with the blackbody radiation law (2.2) gives the Einstein relations:

$$\frac{A_{21}}{B_{21}} = \frac{8\pi n^3 h\nu^3}{c^3}\,, \tag{2.10}$$

$$B_{12} = \frac{g_2}{g_1}B_{21}\,. \tag{2.11}$$

2.3 Atomic lineshapes

In deriving Einstein's coefficients, we have assumed a monochromatic wave with frequency ν. A more realistic model introduces the concept of an atomic lineshape function $g(\nu)$. The distribution $g(\nu)$ is the equilibrium shape of the linewidth-broadened transitions. Express the radiation density as

$$\rho(\nu) = \rho_\nu g(\nu)\,, \tag{2.12}$$

where ρ_ν is the energy density of the electromagnetic field inducing the transitions [13]. In the following, the stimulated rate term (2.7) will be expressed with a stimulated-transition probability W_{21} as

$$W_{21}N_2 = B_{21}\rho(\nu)N_2\,. \tag{2.13}$$

With the intensity $I = c\rho_\nu / n$ [13], and Eqs. (2.10) and (2.13), the stimulated-transition probability is then written as

$$W_{21} = \frac{c^2 I}{8\pi n^2 h\nu^3 \tau_{21}}\,g(\nu)\,. \tag{2.14}$$

There are two main classes of broadening mechanisms, which lead to distinctly different atomic lineshapes:

Homogeneous broadening. In this case, the atoms are indistinguishable and have the same transition energy. A signal applied to the transition has exactly the same effect on all atoms in the collection. In a solid-state laser like Nd:YAG, the main homogenous broadening mechanism is thermal broadening, in which the atomic transition is influenced by the thermal vibrations of the lattice surrounding the active ions.

Inhomogeneous broadening. Here, the atoms are distinguishable and the broadening tend to displace the centre frequencies of individual atoms, thereby broadening the overall response of a collection without broadening the response of individual atoms. Solid-state lasers may be inhomogeneously broadened by crystal inhomogeneities. A good example is the line broadening of neodymium-doped glass lasers.

In the following calculations in this thesis, no broadening mechanisms or atomic lineshapes have been considered.

2.4 Gain and absorption

The gain and absorption coefficients are introduced, together with the emission cross section [12]. Consider a thin slab of thickness *dz*, where the atoms have a capture area or cross section σ, illuminated by photons with intensity *I* (Fig. 2.2). The power absorbed or emitted from one atom is then $\sigma \times I$. The slab is containing population *densities* (population number per volume) N_2 and N_1 in the upper and lower laser levels. If the atoms in the upper level has an effective cross section σ_{21} for power emission, the total intensity (power per area) emitted back to the wave is $N_2 \sigma_{21} dz \times I$. Similarly, if the atoms in the lower level have an effective cross section σ_{12} for power absorption, the total intensity absorbed from the wave is $N_1 \sigma_{12} dz \times I$. The net differential increase of the intensity is then

$$dI = (N_2\sigma_{21} - N_1\sigma_{12})\, I\, dz\,, \tag{2.15}$$

where σ_{21} is the stimulated-emission cross section and σ_{12} is the absorption cross section. With another approach from the rate equation (2.8), for the population density in the upper laser level (where spontaneous emission is ignored), expressed with the transition probabilities (2.13),

$$\frac{dN_2}{dt} = -(N_2W_{21} - N_1W_{12})\ , \tag{2.16}$$

the net intensity increase in the thin slab is then

$$dI = (N_2W_{21} - N_1W_{12})\, h\nu\, dz\,, \tag{2.17}$$

where $h\nu$ is the photon energy. Equating (2.15) and (2.17) then gives the relation

$$W_{21} = \frac{g_1}{g_2} W_{12} = \frac{\sigma_{21} I}{h\nu}. \tag{2.18}$$

Taking the derivative of (2.15) and using $\sigma = \sigma_{21} = g_1 / g_2 \times \sigma_{12}$ gives the net growth in intensity for a wave passing through the medium:

$$\frac{dI}{dz} = \sigma\, \Delta N \times I\,, \tag{2.19}$$

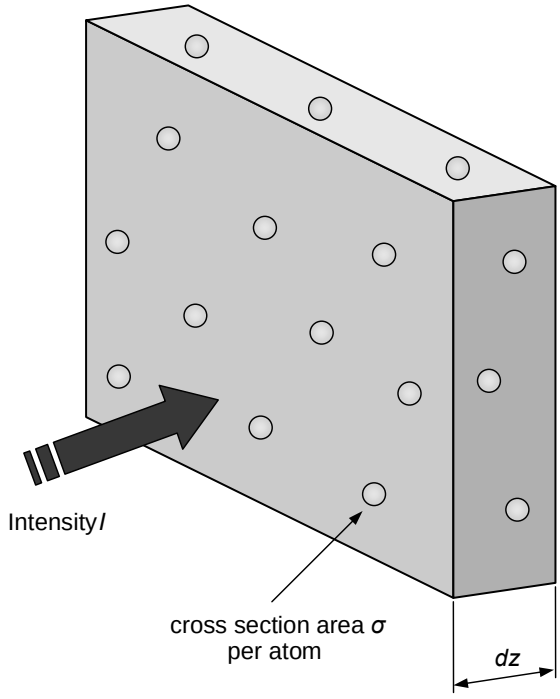

Fig. 2.2. A collection of atoms with absorption or emission cross sections distributed throughout a thin slab.

where the difference

$$\Delta N = \left(N_2 - \frac{g_2}{g_1} N_1 \right) \tag{2.20}$$

is the *population-inversion density*. The gain coefficient is defined as $g = \sigma \Delta N$ and if it is constant, the intensity grows as $I(z) = I(0)\exp(gz)$. If $N_1 > N_2$, we have a net power absorption in the medium and an absorption coefficient can be defined as

$$\alpha = \left(\frac{g_2}{g_1} N_1 - N_2 \right) \times \sigma . \tag{2.21}$$

2.5 Four-level lasers

We now extend the model to a four-level laser (Fig. 2.3), such as the 1064 nm laser transition in Nd:YAG, pumped at 808 nm. The ions (Nd^{3+} in this case) in the ground state 0 are excited to the broad absorption band 3 by the pump light. They then rapidly relax via multiphonon emission through nonradiative processes to the sharp upper metastable laser level 2. The laser transition proceeds then to the lower laser level 1, while a photon is emitted. From here, the ions will again rapidly relax to the ground state.

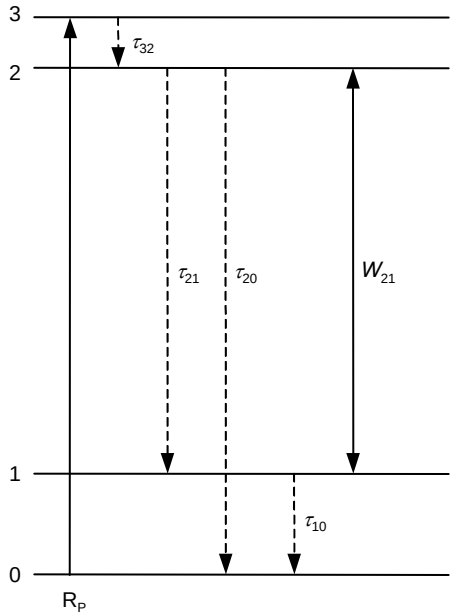

Fig. 2.3. Energy levels of a four-level laser.

The pump-rate density reaching the upper laser level is R_P. The lifetimes of the upper and lower laser levels are τ_2 and τ_1. The lifetime of level 2 is due to transitions to level 1 as well as to level 0:

$$\frac{1}{\tau_2} = \frac{1}{\tau_{21}} + \frac{1}{\tau_{20}}. \tag{2.22}$$

The rate equations for the upper and lower laser levels are then

$$\frac{dN_2}{dt} = R_P - \frac{N_2}{\tau_2} - \left(N_2 - \frac{g_2}{g_1} N_1 \right) W_{21}, \tag{2.23}$$

$$\frac{dN_1}{dt} = \frac{N_2}{\tau_{21}} - \frac{N_1}{\tau_1} + \left(N_2 - \frac{g_2}{g_1} N_1 \right) W_{21}. \tag{2.24}$$

2.6 Pump rate

The pump-rate distribution R_P in Eq. (2.23) is derived by considering a similar rate equation for level 3 as in Eq. (2.16):

$$\left. \frac{dN_3}{dt} \right|_{\text{pump}} \approx W_P N_0, \tag{2.25}$$

where W_P is the pumping-transition probability and it has been assumed that the population in level 3, N_3, is much smaller than the population in the ground state, N_0. By using (2.18), the pump-rate density, which reaches level 2, is then

$$R_P = \eta_P W_P N_0 = \frac{\eta_P \sigma_P N_0 I_P}{h\nu_P} = R r_P , \tag{2.26}$$

where η_P is the quantum efficiency of the pumping process, σ_P is pump-absorption cross section, I_P is the pump intensity distribution and $h\nu_P$ is the pump photon energy. The decay of pump intensity through an end-pumped medium is then given by the absorption coefficient α:

$$\frac{dI_P}{dz} = -\sigma_P N_0 I_P = -\alpha I_P . \tag{2.27}$$

If depletion of the ground-state population (pump saturation) is neglected, α is constant and the pump-intensity distribution decays as $I_P(z) = I_P(0)\exp(-\alpha z)$. The total pump rate R is defined as the total absorbed pump power reaching the upper laser level divided by the pump-photon energy:

$$R = \frac{\text{total pump power}}{h\nu_P} = \frac{\eta_P \eta_a P_P}{h\nu_P} , \tag{2.28}$$

where P_P is the incident pump power, $\eta_a = 1 - e^{-\alpha l}$ is the fraction of the pump power absorbed in an end-pumped crystal of length l. The function r_P,

$$r_P = \frac{\alpha I_P}{\eta_a P_P} , \tag{2.29}$$

is the spatial distribution of the pump beam and is normalised over the crystal:

$$\iiint_{\text{crystal}} r_p(x,y,z)\, dV = 1 . \tag{2.30}$$

2.7 Laser gain saturation

The solution for the population-inversion density (2.20) of the rate equations (2.23) and (2.24) at equilibrium (steady state, $d/dt = 0$) is [13]

$$\Delta N = \frac{\left(\tau_2 + \frac{\tau_1 \tau_2}{\tau_{21}} \frac{g_2}{g_1}\right) R_P}{1 + \left(\tau_2 + \frac{\tau_1 \tau_2}{\tau_{20}} \frac{g_2}{g_1}\right) W_{21}} . \tag{2.31}$$

In a four-level laser, the ions in the lower level are almost immediately transferred to the ground state, that is $N_1 \approx 0$. The rate equation for the upper laser level is then

$$\frac{dN_2}{dt} = R_P - \frac{N_2}{\tau_2} - N_2 W_{21} , \tag{2.32}$$

which has the solution

$$N_2 = \frac{\tau_2 R_P}{1+\tau_2 W_{21}} = \frac{\tau_2 R_P}{1+2I/I_{\text{sat}}} \tag{2.33}$$

at steady state, where 2*I* is the total two-way intensity in a standing-wave resonator and

$$I_{\text{sat}} = \frac{h\nu_L}{\tau_2 \sigma_{21}} \tag{2.34}$$

is called the saturation intensity ($h\nu_L$ is the laser photon energy). In a standing-wave laser cavity, there are two oppositely travelling waves $I_+(z)$ and $I_-(z)$. Suppose now that the gain and loss are sufficiently small for one pass of the laser beam through the cavity. In this low-loss, low-gain approximation, the one-way intensity then remains nearly constant: $I = I_+ = I_-$, and the total intensity is $2I = I_+ + I_-$. The behaviour of the denominator in Eq. (2.33) is called *gain saturation* and can reduce the population in the upper laser level significantly if the circulating intensity I is high. The effect of gain saturation will be discussed for the simulations in Chapter 3.

2.8 Cavity rate equation

To analyse how fast the coherent oscillation in a laser cavity builds up from noise when the laser is first turned on, we follow a small packet of signal energy through one complete round trip within the cavity [12]. For simplicity, the cavity (Fig. 2.4) has two mirrors with reflectivity R_1 and R_2, and a pumped crystal of length l and refractive index n with a constant gain coefficient g and an intrinsic absorption-loss coefficient α_i. The round-trip time is $t_R = 2l_c^*/c$, where l_c^* is the optical path length of the cavity, and the one-way intensity I after one round trip, starting with intensity I_0 at time $t = 0$, is then

$$I(t_R) = I_0 R_1 R_2 \exp(2gl - 2\alpha_i l) = I_0 \exp(2gl - \delta), \tag{2.35}$$

where $\delta = 2\alpha_i l - \ln R_1 R_2$ is the total round trip loss; $\delta = L - \ln(1-T) \approx L + T$, where T is the transmission of the out-coupling mirror and L is the residual round-trip loss. The approximation is valid for small values of T. The net growth after N round trips is given by

$$I(N t_R) = I_0 \exp(N(2gl - \delta)), \tag{2.36}$$

which can be rewritten as

$$I(t) = I_0 \exp\left(\frac{2gl - \delta}{t_R} t\right) \tag{2.37}$$

at time $t = N t_R$. If we define the cavity growth rate $\gamma = cgl/l_c^*$, and the cavity photon lifetime $\tau_c = 2l_c^*/c\delta$, we get

$$I(t) = I_0 \exp\left(\gamma t - \frac{t}{\tau_c}\right). \tag{2.38}$$

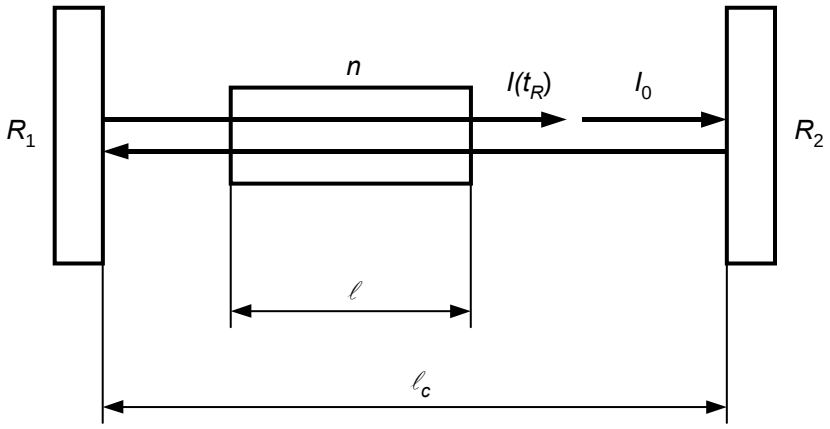

Fig. 2.4. Intensity after one round-trip in a laser cavity.

If γ is time-varying, for example because the gain coefficient saturates, then we must convert this equation to the more general differential form

$$\frac{dI}{dt} = \left(\gamma - \frac{1}{\tau_c} \right) I \, . \tag{2.39}$$

In the situation with an end-pumped crystal, where we have a spatially varying saturated-gain coefficient $G(x, y, z) = \sigma \, \Delta N(x, y, z)$, and the increase in the *one-way* laser intensity $I(x, y, z)$ through the crystal is

$$\frac{dI(x, y, z)}{dz} = G(x, y, z) \, I(x, y, z) \, , \tag{2.40}$$

we will use a method where the number of laser photons in the cavity at steady state can be calculated if the shape of the photon distribution is known [15]. The saturated population-inversion density $\Delta N(x, y, z)$ is of the form (2.33) for a four-level laser.

The one-way laser power at location *z* along the laser axis is given by integrating the intensity over the crystal cross section:

$$P(z) = \iint I(x, y, z) dx dy \, . \tag{2.41}$$

The increase in power after one round-trip is given by integrating over the cavity length twice:

$$2 \int \frac{dP(z)}{dz} dz = 2 \iiint \frac{dI(x, y, z)}{dz} dx dy dz \, . \tag{2.42}$$

In the low-loss, low-gain approximation, the condition that the round-trip gain equals the round-trip loss at steady state gives

$$2 \iiint G(x, y, z) I(x, y, z) \, dx dy dz = P \, \delta \, , \tag{2.43}$$

where P is the average total power in the cavity. The total number of photons in the cavity is defined as the total laser energy after one round trip (total power times the round-trip time) divided by the laser photon energy:

$$\Phi = \frac{\text{total energy}}{h\nu_L} = \frac{P\,t_R}{h\nu_L} = \frac{2l_c^* P_{\text{out}}}{ch\nu_L T}, \tag{2.44}$$

where $P_{\text{out}} = T \times P$ is the laser output power through the output coupler with transmission T. The photon density (number of photons per volume) ϕ is calculated by considering a thin slab with thickness dz. The number of photons per area in the slab, $\phi\,dz$, is then the total intensity $2I$ times the time it takes the light to pass through the slab $dt = n\,dz/c$ divided by the laser photon energy:

$$\phi\,dz = \frac{\text{total intensity} \times dt}{h\nu_L} = \frac{2I\,n\,dz}{ch\nu_L}. \tag{2.45}$$

This gives the photon density

$$\phi = \frac{2nI}{ch\nu_L} = \Phi\frac{nI}{l_c^* P} = \Phi\phi_0. \tag{2.46}$$

Note that the photon density in the laser crystal with refractive index n is n times higher than that of free space. The function ϕ_0,

$$\phi_0 = \frac{nI}{l_c^* P}, \tag{2.47}$$

is the spatial distribution of the laser photons and is normalised over the entire cavity:

$$\iiint_{\text{cavity}} \phi_0(x,y,z)\,dV = 1. \tag{2.48}$$

From (2.46) the intensity is expressed as

$$I = \frac{ch\nu_L}{2n}\Phi\phi_0, \tag{2.49}$$

and the power is

$$P = \frac{ch\nu_L}{2l_c^*}\Phi. \tag{2.50}$$

Thus, inserting (2.49) and (2.50) into (2.43) gives

$$h\nu_L\frac{c\sigma}{n}\iiint_{\text{crystal}} \Delta N(x,y,z)\Phi\phi_0(x,y,z)\,dV - h\nu_L\frac{\Phi}{\tau_c} = 0. \tag{2.51}$$

For a four-level laser, the population-inversion density is given by (2.33):

$$N_2(x,y,z) = \frac{\tau R r_P(x,y,z)}{1 + \dfrac{c\sigma\tau}{n}\Phi\phi_0(x,y,z)}, \tag{2.52}$$

where we have used

$$W_{21} = 2\frac{\sigma I}{h\nu} = \frac{c\sigma}{n}\Phi\phi_0. \tag{2.53}$$

If Eq. (2.52) is put into Eq. (2.51), it is possible to solve for the photon number in the denominator of (2.52) if the pump and photon distributions are known.

Since the power P is the time-derivative of the energy E, which is the number of photons Φ times the photon energy,

$$P = \frac{dE}{dt} = h\nu_L \frac{d\Phi}{dt}, \tag{2.54}$$

it is reasonable to interpret the net growth of power (2.51) as the time-derivative of the photon number times the photon energy. In summary, the rate equations, (2.32) with (2.53) and (2.51) with (2.54), for a four-level laser including the spatial distributions of the pump and laser beams have been derived, as presented by Kubodera and Otsuka in Ref. [16]:

$$\frac{dN_2(x,y,z)}{dt} = Rr_P(x,y,z) - \frac{N_2(x,y,z)}{\tau} - \frac{c\sigma}{n}N_2(x,y,z)\Phi\phi_0(x,y,z), \tag{2.55}$$

$$\frac{d\Phi}{dt} = \frac{c\sigma}{n}\iiint_{\text{crystal}} \Delta N(x,y,z)\Phi\phi_0(x,y,z)\,dV - \frac{\Phi}{\tau_c}, \tag{2.56}$$

where Eq. (2.56) is the *cavity rate equation*. It is seen that the population inversion averaged over the laser-mode distribution is clamped above threshold at steady state. The spatial distribution of the inversion varies, however, according to Eq. (2.52) and gets saturated where the laser field is strong.

2.9 Laser threshold and output power

From the rate equations, well-known results for the threshold pump power

$$P_{P,\text{th}} = \frac{\pi h\nu_P \delta(w_P^2 + w_L^2)}{4\sigma\tau\eta_P\eta_a} \tag{2.57}$$

and the slope efficiency

$$\eta = \frac{T}{\delta}\frac{\nu_L}{\nu_P}\eta_P\eta_a\eta_{PL} \tag{2.58}$$

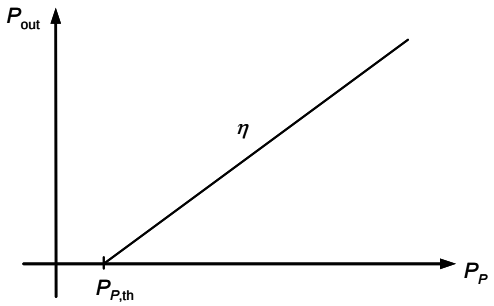

Fig. 2.5. Linear output power from a four-level laser.

for four-level lasers with Gaussian pump and laser beams (Sect. 3.1) have been derived [17]. Here, w_P is the pump-beam radius, w_L is the laser-beam radius and η_{PL} is the overlap efficiency between the pump mode and the laser mode. At low power, η_{PL} can be approximated as

$$\eta_{PL} \approx \frac{w_L^2(2w_P^2 + w_L^2)}{(w_P^2 + w_L^2)^2}. \tag{2.59}$$

The output power from the laser in this approximation is $P_{\text{out}} = \eta(P_P - P_{P,\text{th}})$ as depicted in Fig. 2.5.

2.10 Energy-transfer upconversion

A number of papers [6–11] have shown that the influence of energy-transfer upconversion (ETU) is a detrimental effect in Nd-doped lasers. In Fig. 2.6, a simplified energy-level scheme for Nd:YAG involving relevant levels and processes is shown. All dashed lines indicate heat-generating processes. Pump radiation is absorbed from the ground state $^4I_{9/2}$ to the pump level $^4F_{5/2}$ from where it relaxes via multiphonon emission to the upper laser level $^4F_{3/2}$. Next, the four fluorescent processes and the cascaded multiphonon relaxations (dashed lines) to the ground state are shown. The three upconversion processes UC_1–UC_3 involve two nearby ions in the upper laser level. One ion relaxes down to a lower lying level and transfers its energy to the other ion, which is thereby raised (upconverted) to a higher level. Consequently, ETU reduces the population of the upper laser level, hence degrading the laser performance.

Rigorous numerical modelling of upconversion effects in four-level lasers has been done by Pollnau *et al.* [9,10]. The rate equations including all nine energy levels are presented in Appendix A. The rate-equation scheme can be simplified by considering that the decay rate via multiphonon processes from levels 1–3 and 5–8 is fast compared with the lifetime of the upper laser level 4. The combined effect of the different upconversion process can then be expressed by a single rate parameter $W = W_1 + W_2 + W_3$, and the net effect is that only one excitation is removed from the upper laser level by each upconversion process, since the upconverted ion will decay rapidly back to level 4. Thus, only two energy levels are considered [6,9]: the population in the upper laser level 4 has the rate equation

$$\frac{dN_4}{dt} = Rr_P - \frac{N_4}{\tau} - \frac{c\sigma}{n} N_4 \Phi \phi_0 - W N_4^2, \tag{2.60}$$

and the population in the ground state 0 is taken from conservation of the doping concentration $N_d = N_0 + N_4$.

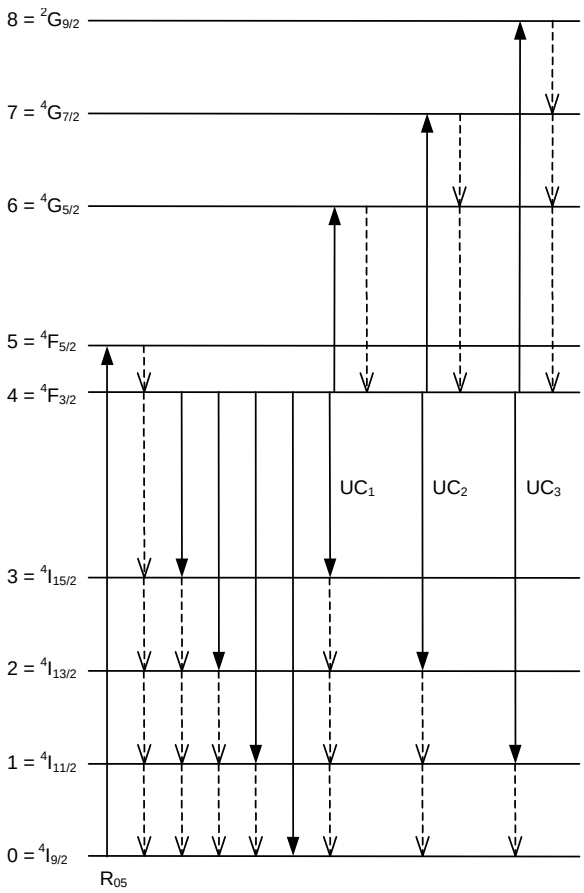

Fig. 2.6. Energy level scheme of Nd:YAG including upconversion processes (UC_1–UC_3).

Analytical modelling including ETU effects on four-level lasers under nonlasing and lasing conditions has previously been done in the literature [11,20,21].

2.11 Quasi-three-level lasers

In a quasi-three-level laser, the lower laser level is in the thermally populated ground state. Efficient lasing on quasi-three-level transitions ($^4F_{3/2} \rightarrow {}^4I_{9/2}$) at 900–950 nm in Nd-doped crystals is considerably more difficult to achieve than on the stronger four-level transitions ($^4F_{3/2} \rightarrow {}^4I_{11/2}$) at 1–1.1 μm (Fig. 1.1). The problems with these quasi-three-level transitions are a significant reabsorption loss at room temperature and a very small stimulated-emission cross section [1,2]. This requires a tight focusing of the pump light, which is achieved by end-pumping with high-intensity diode lasers.

In the past, several studies have included reabsorption loss in the modelling of longitudinally pumped lasers including the effect of overlap of the pump and laser field [15,18,19]. An example of an energy-level scheme that can be modelled is the $^4F_{3/2} \rightarrow {}^4I_{9/2}$ lasing transition at 946 nm in Nd:YAG. The upper laser level is the lower (R_1) of the two crystal-field components of the $^4F_{3/2}$ level, and the lower laser level is the uppermost (Z_5) of the five crystal-field components of the $^4I_{9/2}$ level.

The fraction of the total $^4F_{3/2}$ population density N_4 residing in the upper laser level is denoted f_b; that is, the actual population density is $N_b = f_b N_4$ where

$$f_b = \frac{g_b \exp(-\Delta E_{4b} / kT)}{Z_4} \tag{2.61}$$

and

$$Z_4 = \sum_{i=1}^{m} g_i \exp(-\Delta E_{4i} / kT) \tag{2.62}$$

is the partition function of level 4, ΔE_i is the energy of sublevel i relative to the lowest sublevel of that manifold and g_i is the degeneracy of sublevel i. Similarly, the fraction of the total $^4I_{9/2}$ population density N_0 in the lower laser level is denoted f_a, and the actual population density is $N_a = f_a N_0$. If depletion of the ground-state population is neglected, the rate equation for the population density in $^4F_{3/2}$ can then be written as [15,18]

$$\frac{dN_b(x,y,z)}{dt} = f_b R r_P(x,y,z) - \frac{N_b(x,y,z) - N_b^0}{\tau} - \frac{c\sigma}{n} f_b \Delta N(x,y,z) \Phi \phi_0(x,y,z), \tag{2.63}$$

$$\frac{dN_a(x,y,z)}{dt} = -f_a R r_P(x,y,z) - \frac{N_a(x,y,z) - N_a^0}{\tau} + \frac{c\sigma}{n} f_a \Delta N(x,y,z) \Phi \phi_0(x,y,z), \tag{2.64}$$

where N_a^0 and N_b^0 are the unpumped population-inversion densities, τ is the lifetime of the upper state, and σ is the stimulated emission cross section for the quasi-three-level laser transition. The population-inversion density is expressed as $\Delta N = f_b N_4 - (g_b / g_a) f_a N_0$, and it should be noted that here, the *spectroscopic* stimulated-emission cross section σ is used between individual crystal-field levels, whereas for the previously presented four-level lasers, the *effective* stimulated-emission cross section $\sigma_{\text{eff}} = f_b \sigma$ was used for the entire manifold population. In Nd:YAG, each level has a degeneracy of 2, and solutions for (2.63) and (2.64), as well as the output performance have been calculated by Fan and Byer [18] and Risk [15].

2.12 Quasi-three-level lasers including energy-transfer upconversion

In order to model quasi-three-level lasers including reabsorption loss and energy-transfer upconversion, we start from the space-dependent rate equations, which describe population inversion and photon density in the steady-state case of a laser cavity. The rate-equation analysis in this section has been presented in Papers II–III. As before, the rate-equation scheme is simplified from including nine energy levels to only two: the upper laser level in $^4F_{3/2}$ and the lower laser level in the thermally populated ground state $^4I_{9/2}$. If depletion of the ground-state population is neglected, the rate equation (2.60) for the population density in $^4F_{3/2}$ can then be written as

$$\begin{aligned} \frac{dN_4(x,y,z)}{dt} = R r_P(x,y,z) - \frac{N_4(x,y,z) - N_4^0}{\tau} - \frac{c\sigma}{n} \Delta N(x,y,z) \Phi \phi_0(x,y,z) \\ - W\left(N_4(x,y,z) - N_4^0\right)^2 = 0, \end{aligned} \tag{2.65}$$

with a single upconversion parameter W. The population-inversion density is expressed as $\Delta N = N_b - N_a$, and is calculated by using the fact that the doping concentration N_d is conserved: $N_d = N_0 + N_4 = N_0^0 + N_4^0$, where N_0^0 and N_4^0 are the unpumped population densities. It is then shown that

$$\Delta N - \Delta N^0 = (f_a + f_b)(N_4 - N_4^0), \tag{2.66}$$

and the resulting rate equation for the population-inversion density is

$$\begin{aligned}\frac{d\Delta N(x,y,z)}{dt} = (f_a + f_b)Rr_P(x,y,z) - \frac{\Delta N(x,y,z) - \Delta N^0}{\tau} \\ - \frac{c\sigma}{n}(f_a + f_b)\Delta N(x,y,z)\Phi\phi_0(x,y,z) \\ - \frac{W}{(f_a + f_b)}\left(\Delta N(x,y,z) - \Delta N^0\right)^2 = 0,\end{aligned} \tag{2.67}$$

where ΔN^0 is the unpumped population-inversion density. The pumping process is assumed to have unity quantum efficiency ($\eta_P = 1$).

In thermal equilibrium $N_a^0 >> N_b^0$, so the unpumped population inversion is written $\Delta N^0 \approx -N_a^0$ and the solution for the population-inversion density at steady state is then calculated from Eq. (2.67):

$$\Delta N = \frac{2\tau f Rr_P + 2\dfrac{c\sigma\tau}{n} fN_a^0\Phi\phi_0}{1 + \dfrac{c\sigma\tau}{n} f\Phi\phi_0 + \sqrt{\left(1 + \dfrac{c\sigma\tau}{n} f\Phi\phi_0\right)^2 + 4W\tau^2 Rr_P + 4W\tau^2 \dfrac{c\sigma}{n} N_a^0\Phi\phi_0}} - N_a^0, \tag{2.68}$$

where $f = f_a + f_b$. The expression in the numerator is the total absorption rate, including reabsorption, times τ. From Eq. (2.68), it is seen that the positive part of the population inversion is reduced by the fraction of excited ions F_{ETU} that involve the ETU processes:

$$\Delta N = (\Delta N_{\text{no ETU}} + N_a^0)(1 - F_{\text{ETU}}) - N_a^0, \tag{2.69}$$

where $\Delta N_{\text{no ETU}}(x,y,z)$ is the population-inversion density without any ETU effects present given by

$$\Delta N_{\text{no ETU}}(x,y,z) = \frac{\tau f Rr_P(x,y,z) + \dfrac{c\sigma\tau}{n} fN_a^0\Phi\phi_0(x,y,z)}{1 + \dfrac{c\sigma\tau}{n} f\Phi\phi_0(x,y,z)} - N_a^0, \tag{2.70}$$

and the fraction of excited ions that involve the ETU processes is then

$$F_{\mathrm{ETU}}(x,y,z) = 1 - \frac{2}{1+\sqrt{1+\dfrac{4W\tau^2 R r_P(x,y,z) + 4W\tau^2 \dfrac{c\sigma}{n} N_a^0 \Phi \phi_0(x,y,z)}{\left(1+\dfrac{c\sigma\tau}{n} f\Phi\phi_0(x,y,z)\right)^2}}}, \qquad (2.71)$$

which can also be taken from the rate equation (2.67), as the fraction between the last term involving the population inversion going to ETU and the total absorption rate.

Below threshold ($\Phi = 0$), the resulting expression for the population inversion is

$$\Delta N_{\mathrm{th}}(x,y,z) = \frac{2\tau f R_{\mathrm{th}} r_P(x,y,z)}{1+\sqrt{1+4W\tau^2 R_{\mathrm{th}} r_P(x,y,z)}} - N_a^0, \qquad (2.72)$$

which can be written as Eq. (2.69) where the population-inversion density below threshold without any ETU effects present is given by

$$\Delta N_{\mathrm{no\,ETU,th}}(x,y,z) = \tau f R_{\mathrm{th}} r_P(x,y,z) - N_a^0, \qquad (2.73)$$

and the fractional reduction $F_{\mathrm{ETU,th}}$ below threshold is

$$F_{\mathrm{ETU,th}}(x,y,z) = 1 - \frac{2}{1+\sqrt{1+4W\tau^2 R_{\mathrm{th}} r_P(x,y,z)}}. \qquad (2.74)$$

The population-inversion density (2.68) can be inserted directly into the rate equation of the cavity photon number (2.56), to obtain an implicit relation between the pump rate R and the total laser-cavity photon number Φ:

$$\frac{2\sigma l_c^*}{n} \iiint_{\mathrm{crystal}} \Delta N(x,y,z)\phi_0(x,y,z)\,dV = \delta, \qquad (2.75)$$

$$\frac{2\sigma l_c^*}{n} \iiint_{\mathrm{crystal}} \frac{2\tau f R r_P \phi_0 + 2\dfrac{c\sigma\tau}{n} f N_a^0 \Phi \phi_0^2}{1+\dfrac{c\sigma\tau}{n} f\Phi\phi_0 + \sqrt{\left(1+\dfrac{c\sigma\tau}{n} f\Phi\phi_0\right)^2 + 4W\tau^2 R r_P + 4W\tau^2 \dfrac{c\sigma}{n} N_a^0 \Phi \phi_0}}\,dV = \delta + \delta_l, \qquad (2.76)$$

where $\delta_l = 2N_a^0\sigma(l_c^*/n)\iiint \phi_0\,dV$ $(= 2N_a^0\sigma l$ if ϕ_0 is constant in the z-direction) is the loss term due to the population in the lower laser level. The relation (2.76) can then be solved to determine the output power of the laser. Equation (2.75) indicates that the total gain integrated over the laser distribution, which includes the pumped gain and reabsorption loss with ETU

effects, is equal to the round-trip loss. If the population-inversion density at threshold (2.72) is inserted into Eq. (2.56), the pump rate at threshold can be solved from

$$R_{\text{th}} = \frac{\delta + \delta_l}{2\sigma\tau f l_c^*} \left(\iiint_{\text{crystal}} \frac{2 r_P \phi_0}{1 + \sqrt{1 + 4W\tau^2 R_{\text{th}} r_P}} dV \right)^{-1} . \tag{2.77}$$

2.13 Thermal loading

The presence of ETU effects will give rise to extra heat load in the laser crystal due to the multiphonon relaxation from the excited level back to the upper laser level. The fractional reduction F_{ETU} of the population-inversion distribution due to upconversion is taken from Eq. (2.71). The fractional thermal loading distribution is then expressed as [11,21]

$$\xi(x, y, z) = \xi_0 (1 - F_{\text{ETU}}(x, y, z)) + F_{\text{ETU}}(x, y, z) , \tag{2.78}$$

where ξ_0 is the thermal loading when upconversion is absent, which under lasing conditions is taken as the quantum defect $1 - \lambda_P / \lambda_L \approx 0.15$, where λ_P = 808 nm is the pump wavelength and λ_L = 946 nm is the laser wavelength. The first term in Eq. (2.78) is the thermal loading caused by the quantum defect and the second term is the contribution from the upconversion. For operation under nonlasing conditions, the thermal loading $\xi_{0,\text{NL}}$ has been determined to 0.29 [10] (multiphonon processes to the ground state have been included) and the fractional reduction $F_{\text{ETU,NL}}$ is taken from Eq. (2.74). The situation under nonlasing conditions, where significant extra heat load is generated compared to under lasing conditions has previously been analysed in detail in the literature [10,11].

2.14 Heat generation and thermal lensing

When the fractional thermal loading has been determined from Eq. (2.78) with the extra contribution from ETU processes, the heat-source density $Q(r, z)$ in the crystal (here, a cylindrical rod) is assumed to have the same shape as the absorbed pump light weighted by the thermal-loading distribution:

$$Q(r, z) = \xi(r, z) P_P \eta_a r_P(r, z) . \tag{2.79}$$

In order to calculate the thermal lensing, we start by solving the steady-state temperature distribution $T(r, z)$ in the rod from the heat-conduction equation

$$\nabla \cdot (-K(T) \nabla T(r, z)) = -Q(r, z) , \tag{2.80}$$

where the heat conductivity $K(T)$ is given in the first approximation by [22]

$$K(T) = K_0 \frac{T_0}{T} , \tag{2.81}$$

where K_0 is the heat conductivity at a reference (room) temperature T_0. With boundary conditions, the heat equation can be solved numerically in a finite element (FE) analysis.

The thermal lensing is an effect of the inhomogeneous distributions of temperature, strain and displacement in the laser crystal. They cause a change of the refractive index at

each point in it. For light propagating through the crystal, this results in a variation of the phase fronts. The optical path difference (OPD) in the crystal is expressed as an equivalent distance in free space, and for a paraxial beam propagating in the *z*-direction it is defined as [23,24]

$$\mathrm{OPD}(r) = \int_0^l \chi(T)\,T(r,z)\,dz\,, \tag{2.82}$$

where χ is the thermooptic coefficient

$$\chi(T) = \frac{dn}{dT}(T) + C_\alpha (n-1)(1+\nu)\,\alpha_T(T) + n^3 \alpha_T(T)\,C_{r,\varphi}\,. \tag{2.83}$$

The first term is the thermal dispersion dn/dT and the second term is due to the thermal expansion along the *z*-axis, where ν is Poisson's ratio and α_T is the thermal-expansion coefficient. The parameter C_α is varying in the range (0,1) and takes into account that the crystal cannot freely expand in the longitudinal direction, if a transversely localised temperature increase occurs [10]. The third term is the stress-induced birefringence, where $C_{r,\varphi}$ is the photoelastic coefficient. It is often small and can be neglected.

The focal length f_{th} of the thermal lens associated with the optical path difference OPD(r) is given by [25]

$$\mathrm{OPD}(r) - \mathrm{OPD}(0) = -\frac{r^2}{2 f_{th}}\,. \tag{2.84}$$

For a cylindrical laser crystal, end-pumped with a Gaussian beam (Sect. 3), the result is

$$f_{th} = \frac{\pi K w_P^2}{\xi P_P \eta_a \chi}\,, \tag{2.85}$$

if upconversion effects are ignored. Under nonlasing conditions, significant extra heat is generated and the thermal lensing has been shown to be much stronger [10,11], at least a factor 2 in Nd:YAG at 1064 nm.

3 Simulations of end-pumped quasi-three-level lasers including energy-transfer upconversion

3.1 Gaussian beam pumping

In order to study the influence of upconversion on the performance of the laser in the simplest case, we assume that the transverse modes of the pump and laser modes are TEM_{00} Gaussian beams with negligible diffraction in the gain medium. Then the normalised pump distribution in Eq. (2.29) is given by

$$r_P(r,z) = \frac{2\alpha}{\eta_a \pi w_P^2} \exp\left(\frac{-2r^2}{w_P^2}\right) \exp(-\alpha z), \tag{3.1}$$

where w_P is the pump-beam radius, and the normalised photon density in free space from Eq. (2.47) is given by

$$\phi_0(r,z) = \frac{2}{\pi w_L^2 l_c^*} \exp\left(\frac{-2r^2}{w_L^2}\right), \tag{3.2}$$

where w_L is the laser-beam radius. The photon density in the laser crystal with refractive index n is n times higher than that of free space.

We will use the same normalised parameters as in Risk [15] and Moulton [26]:

$$a = \frac{w_P}{w_L}, \tag{3.3}$$

$$x = \frac{2r^2}{w_P^2}, \tag{3.4}$$

$$F = \frac{4\tau\sigma R}{\pi w_L^2 \delta}, \tag{3.5}$$

$$S = \frac{2c\sigma\tau\Phi}{\pi w_L^2 l_c^*}, \tag{3.6}$$

$$B = \frac{2N_a^0 \sigma l}{\delta}. \tag{3.7}$$

In addition, we define the following parameter in order to include the upconversion effects:

$$U = \frac{2W\tau\delta}{f\sigma l}, \tag{3.8}$$

Substituting these parameters (3.3)–(3.8) into Eq. (2.77) gives an implicit expression for F:

$$F = \frac{1 + B - \dfrac{2Ba^2}{l} \int_0^{\infty} \int_0^{l} \dfrac{fSe^{-2a^2 x}}{1 + fSe^{-a^2 x} + \sqrt{(1 + fSe^{-a^2 x})^2 + \alpha l / \eta_a a^2 \times fUFe^{-x} e^{-\alpha z} + fUBSe^{-a^2 x}}} dzdx}{2f \dfrac{\alpha}{\eta_a} \int_0^{\infty} \int_0^{l} \dfrac{e^{-(a^2+1)x} e^{-\alpha z}}{1 + fSe^{-a^2 x} + \sqrt{(1 + fSe^{-a^2 x})^2 + \alpha l / \eta_a a^2 \times fUFe^{-x} e^{-\alpha z} + fUBSe^{-a^2 x}}} dzdx}. \tag{3.9}$$

where a is the ratio of pump- and laser-beam waists, F is a normalised variable proportional to pump power, S is a normalised variable proportional to internal laser power, B is the ratio of reabsorption loss to fixed cavity loss, and U is a normalised variable proportional to upconversion loss.

The laser threshold is determined by letting $S = 0$ in Eq. (3.9) and can then be solved from:

$$F_{\text{th}} = \frac{1 + B}{2f \dfrac{\alpha}{\eta_a} \int_0^{\infty} \int_0^{l} \dfrac{e^{-(a^2+1)x} e^{-\alpha z}}{1 + \sqrt{1 + \alpha l / \eta_a a^2 \times fUF_{\text{th}} e^{-x} e^{-\alpha z}}} dzdx}. \tag{3.10}$$

We can now use the analysis above with the five normalised key parameters: beam overlap a, pump power F, laser power S, reabsorption loss B and upconversion effects U, in order to get an understanding of the laser performance.

3.2 Output performance

In Paper III, I have calculated how the laser threshold and laser power is influenced by the combined effect of reabsorption loss and upconversion effects. Especially, the effect of varying the ratio of pump- and laser-beam waists a was studied in order to find optimum pump-focusing conditions. In the definitions of normalised pump power F (3.5) and normalised laser power S (3.6), it is seen that the laser-mode radius w_L is included. For fixed parameters F and S, it is thus clear that it is rather the pump-mode radius w_P that is changed when $a = w_P / w_L$ is varied. In this section, the pump mode's influence on the laser performance is studied, whereas the dependence of laser-mode size will be studied in Sect. 4.1.

The threshold F_{th} is determined by solving Eq. (3.10) numerically and is plotted versus the pump-to-laser-mode ratio a for different degrees of upconversion effects U. In Fig. 3.1, the result is shown for a laser experiencing reabsorption loss ($B = 1$). With no upconversion present ($U = 0$), it is well known that the optimum laser performance is achieved when $a \to 0$. When $U > 0$, the threshold is increased dramatically when $a \to 0$ ($a \lesssim 0.3$) because the upconversion is very strong at high pump intensity. This will degrade the population in the upper laser level, causing extra heat generation when a is low; the optimum seems to be around $a = 0.5$. The increase on threshold due to ETU effects is larger when $B = 1$ than when $B = 0$. The explanation for this behaviour is that below threshold, the positive part of the population-inversion density (2.68) is decreasing depending on the strength of upconversion. In addition, if a constant lower level density N_a^0 is present, that reduction in population

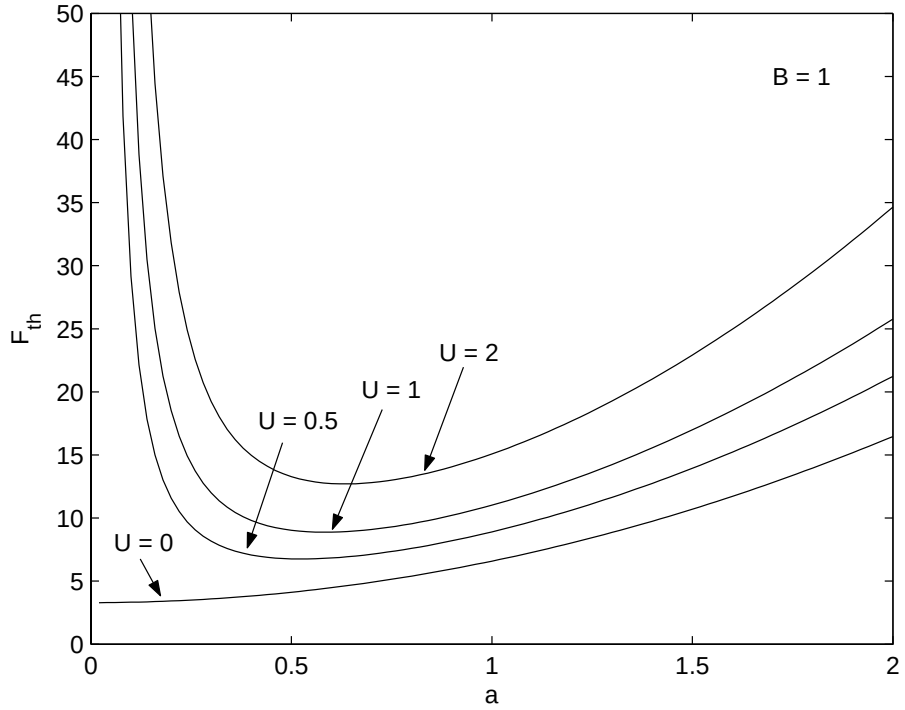

Fig. 3.1. Normalised threshold as function of the mode waist ratio $a = w_P / w_L$ for different values of the upconversion parameter U for a laser experiencing reabsorption loss $B = 1$.

inversion gets more significant. Hence, less positive gain is available, which leads to a higher threshold.

To calculate the normalised laser power S, it is necessary to solve Eq. (3.9) numerically at a particular pump power F. In Fig. 3.2, the laser power is plotted versus the pump-to-laser-mode ratio a for different U, $F = 200$ and $B = 1$. The optimum performance seems to be for values of a between around 0.3 and 1. In this area, the laser power is only slightly reduced by upconversion effects. How upconversion influences the population-inversion density for some values of a is discussed in Sect. 3.3.

Conclusions are that the impact of upconversion is large particularly on the threshold, and that there is a significant difference between a four-level laser and a quasi-three-level laser. Choosing the right pump-to-laser-mode ratio is crucial for optimum output performance of an end-pumped laser when ETU effects are included.

3.3 Extra heat generated by energy-transfer upconversion

We will now give some numerical examples of how extra heat is generated by the ETU processes. First, we study how the spatial distribution of the population-inversion ΔN (and hence the gain) is influenced by ETU for two cases of pump-to-laser-mode ratio a. In Fig. 3.3, the normalised radial distributions of the population inversion are shown for different values of U and $F = 200$, $S = 200$ and $B = 1$. Upconversion is reducing ΔN in all cases, but the distribution is strongly dependent of a and saturation of gain is strong for $a \gtrsim 1$. For $a = 0.2$, there is hardly any change in shape of the gain but it is reduced due to the strong pump intensity when upconversion is included. For $a = 2$, the gain is heavily saturated by the laser mode, primarily in the centre of the gain distribution. Unsaturated gain is still available essentially outside the laser distribution, which may cause higher-order transverse modes to oscillate as is further investigated in Sect. 4.2. When upconversion is present, the unsaturated

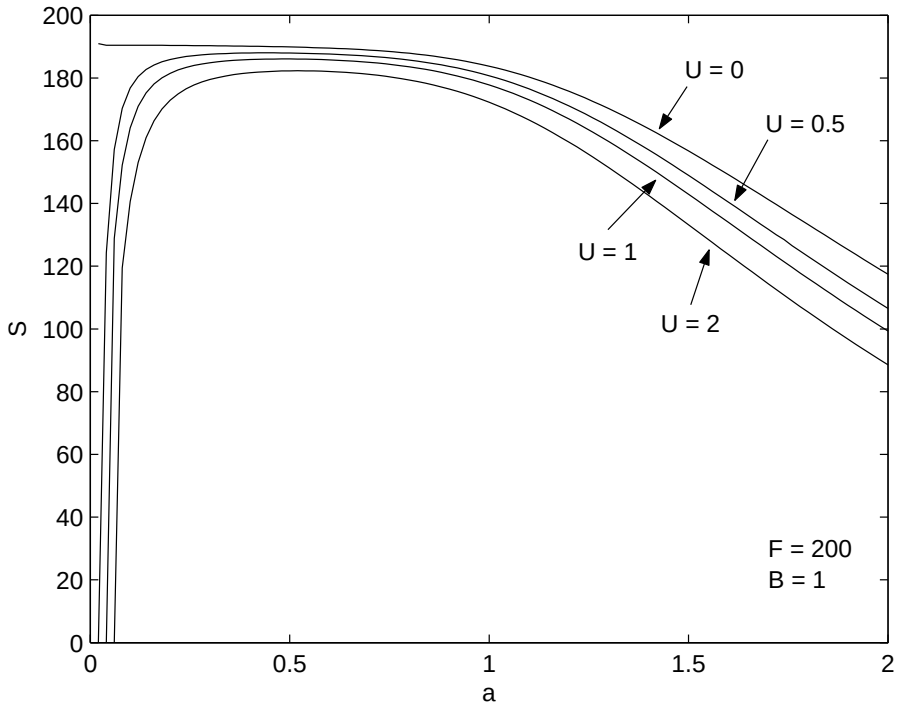

Fig. 3.2. Normalised internal laser power as function of the mode waist ratio $a = w_P / w_L$ for different values of the upconversion parameter U for a laser experiencing reabsorption loss $B = 1$. The normalised pump power is $F = 200$.

gain in the wings is decreasing considerably. Aside from being saturated from the laser field, the gain is also reduced from the upconversion distribution proportional to the absorbed pump, which is likewise saturated by the laser field in the centre, and hence ETU is strongest away from centre. This explains why the saturated gain is primarily reduced in the wings by ETU processes.

Equation (2.69) shows that it is interesting to study the ratio of the positive parts of ΔN and $\Delta N_{\text{no ETU}}$, since the fractional reduction of excited ions F_{ETU} is one minus this ratio. From Fig. 3.3, one can get an idea of how the radial distributions of F_{ETU} should look like, by studying the curves where ETU is included and compare them to the curve where $U = 0$. The calculated result of F_{ETU} is shown in Fig. 3.4. In each plot, the radial pump distribution is displayed for comparison, since the final generated heat is a multiplication between F_{ETU} and the pump distribution. For $a = 0.2$, F_{ETU} is distributed in the centre and will contribute to extra heat significantly. For $a = 2$, F_{ETU} in the centre is low, but is increasing rapidly in the wings, which are partly overlapping the laser distribution, resulting in extra heat.

The conclusion is that under lasing conditions extra heat is generated in the presence of ETU processes. This extra heat generation is particularly strong in the wings of a saturated gain profile when the pump mode is larger than the laser mode.

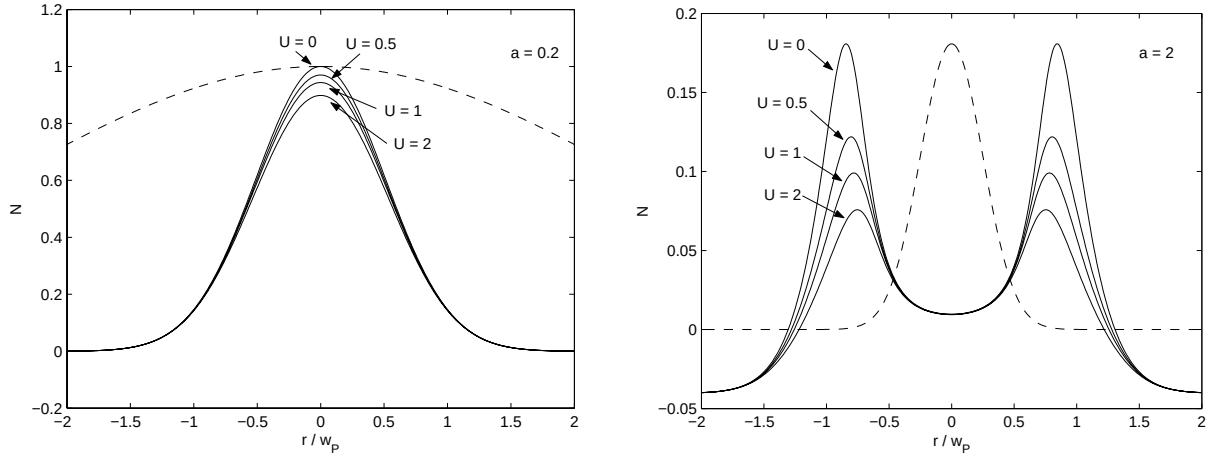

Fig. 3.3. Radial distribution of the normalised population-inversion density (integrated over *z*) under lasing conditions for $F = 200$, $S = 200$, $B = 1$, and different values of U: (a) $a = 0.2$, (b) $a = 2$. Units on vertical axis are arbitrary, but consistent from figure to figure. The laser field profile is indicated by the dashed line.

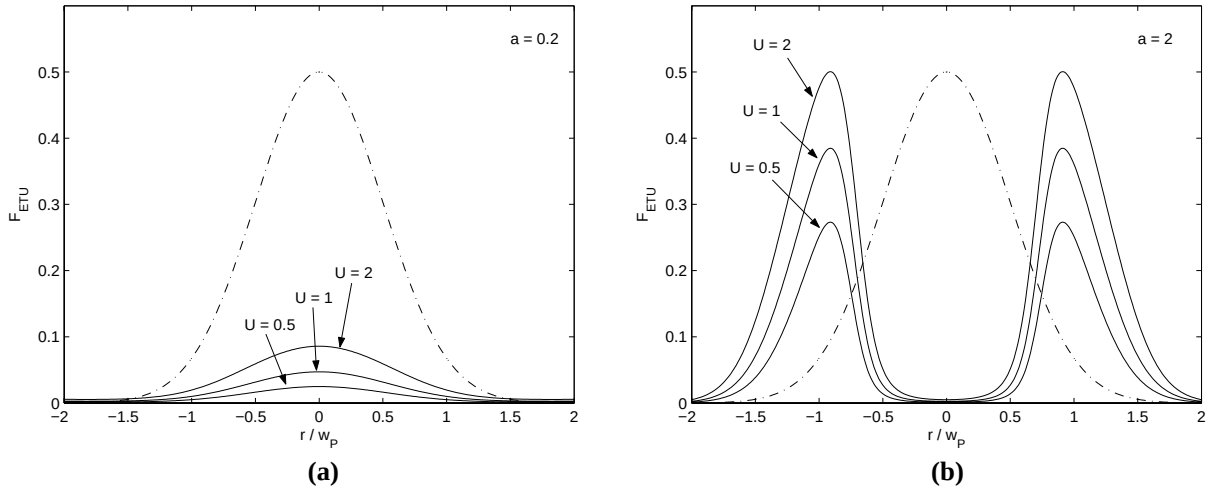

Fig. 3.4. Radial distribution of F_{ETU} (integrated and taken as mean over *z*) under lasing conditions for $F = 200$, $S = 200$, $B = 1$, and different values of U: (a) $a = 0.2$, (b) $a = 2$. The pump field profile is indicated by the dash-dotted line and is shown constant for all figures.

4 Application to quasi-three-level Nd:YAG lasers

4.1 Output performance of 946 nm Nd:YAG lasers

Here, we apply the foregoing model in Sect. 2.12 to a laser that exhibit reabsorption loss and the influence of energy-transfer upconversion. The laser studied is operating on the ${}^4F_{3/2} \rightarrow {}^4I_{9/2}$ transition at 946 nm in Nd:YAG. The results were presented in Papers II and III, and are summarised here.

The laser rod is a transversally directly water-cooled composite rod with a diameter of 3 mm, a 5 mm long doped middle section and with two undoped end-caps each 5 mm in length. The end-caps allow for a longitudinal heat flow when the crystal is heated by the pump, which reduces the thermal effects. The pump was a high-brightness fibre-coupled laser diode array. The maximum power at 808 nm reaching the laser rod after the pump optics and the in-coupling mirror was slightly above 20 W. The laser was built as a simple plane-plane cavity with an out-coupling mirror of 6% transmission. With this resonator design, the pump threshold was about 4 W and the average slope efficiency was 37% with respect to incident power. The maximum output power was 6.5 W with a beam-quality factor (beam-propagation factor) of $M^2 = 4.6$.

Using an M^2 factor, the higher order transverse-mode beam from the diode-pump laser is described as a Gaussian beam with the distribution (3.1), where the pump-beam radius $w_P(z)$ in the crystal is given by

$$w_P(z) = w_{P0}\sqrt{1+\left(\frac{\lambda_P M_P^2 (z - z_{P0})}{\pi n w_{P0}^2}\right)^2}\,, \tag{4.1}$$

where w_{P0} = 100 µm is the pump beam waist, λ_P = 808 nm is the pump wavelength, $M_P^2 = 54$ is the beam-quality factor of the pump source and z_{P0} is the focusing distance of the pump beam from the entrance surface of the active medium. The laser-beam distribution is given by Eq. (3.2) where the beam radius w_L of the laser beam with Gaussian intensity profile is approximated to be constant throughout the active medium.

The output power P_{out} is solved from the implicit expression for the photon number Φ (2.76) at different pump powers with the use of Eqs. (2.28) and (2.44). When the pump distribution is fixed, the output performance of the laser is strongly dependent on the laser-mode size. In Fig. 4.1, the output power has been calculated versus w_L for four different pump powers: 6.9, 11.6, 16.3 and 20.6 W. For these pump levels, we have experimental data on output power, beam quality and focal length of the thermal lens. The following parameters have been used in the calculations: $f_a = 0.0074$, $f_b = 0.6$, $N_d = 1.5 \times 10^{-20}$ cm^{-3} (1.1% doping concentration) [18], $n = 1.82$, $\tau = 230$ µs [14], $\sigma = 5.1 \times 10^{20}$ cm^2 [27], $W = 2.8 \times 10^{-16}$ cm^{3}s^{-1} [6], $l = 5$ mm, $l_c = 17$ mm, $l_c^* = 29.3$ mm, $T = 6\%$, $L = 2\%$ and $z_{P0} = 0$ mm. The reabsorption-loss term is calculated to $\delta_l = 5.7\%$ and the total round-trip loss including the reabsorption-loss term is then 13.7%. We determined the absorption coefficient α experimentally to about 3 cm^{-1} and the fraction of the pump power absorbed in the crystal is then 78%. The output power in Fig. 4.1 is reaching its maximum value for a laser-beam radius in the range of 100–200 µm, with an increasing trend for higher powers. For every pump level, there seems to exist a preferred laser beam size w_L, which maximises the output power. It is interesting to compare this behaviour with the calculations in Sect. 3.2. If the pump-beam radius (4.1)

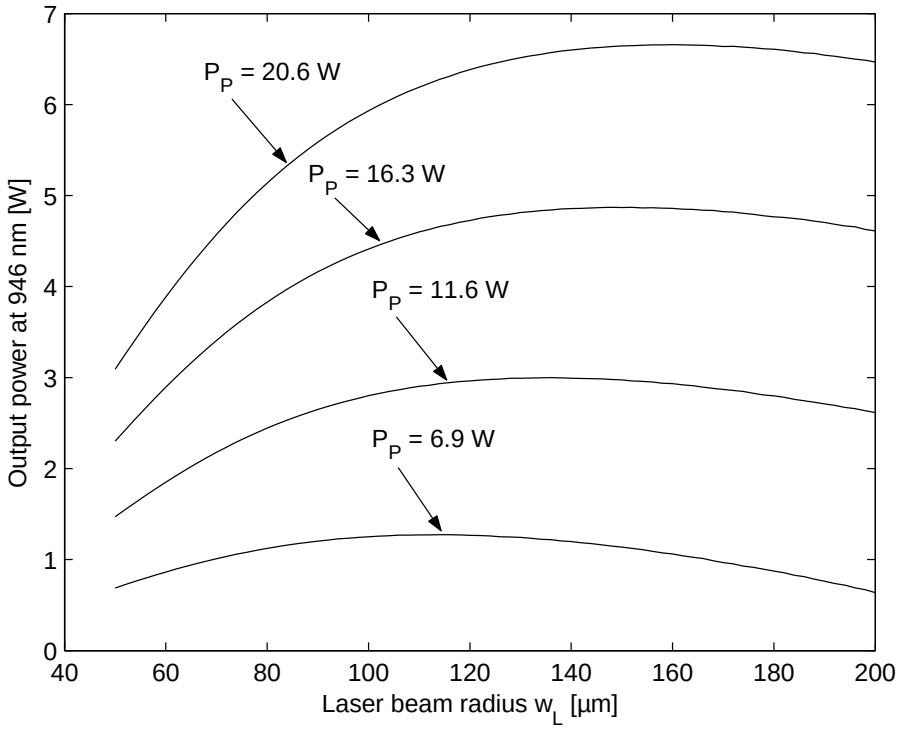

Fig. 4.1. Calculated output power including the influence of ETU at 946 nm versus laser mode radius w_L for different pump powers P_P.

through the crystal is weighted with $\exp(-\alpha z)$, the average pump-beam radius gets w_P = 187 µm. If we compare with Fig. 3.2, we can se that the predicted case where the output power approaches zero when a is low is not reached, unless the laser-beam radius is kept very high. In order to study this effect, we need a pump source with better beam quality that allows tighter focusing throughout the crystal. If the laser beam radius is set to w_L = 150 µm, the normalised parameters are calculated as a = 1.25, B = 0.71, U = 0.67, F = 54 and S = 34. It should be pointed out, that in Sect. 3.2, the variation of the pump-mode size was studied, whereas here the pump-mode size is kept constant and the dependence of the laser-mode size is investigated.

4.2 Thermal lensing and laser beam quality degradation

In a plane-plane cavity, the laser-beam size is strongly dependent of the thermal lensing. We will here study thermal lensing, its dependence of the laser-mode size and its influence on the laser beam quality. A simple model for the degradation in beam quality from saturated gain effects is also proposed.

In order to calculate the thermal lensing, we start by solving the steady-state temperature distribution $T(r,z)$ in the composite rod from the heat-conduction equation (2.80) with Eqs. (2.79) and (2.81), where K_0 = 13 $\mathrm{Wm^{-1}K^{-1}}$ [22] is the heat conductivity at the reference temperature T_0 = 300 K. The boundary conditions at the end surfaces are defined by a heat flow to the stagnant ambient air with the heat-transfer coefficient set to 27.5 $\mathrm{Wm^{-2}}$ [28]. The temperature of the air and the cooling water was assumed to be the same, that is 293 K, and the heat transfer at the cylindrical surface in contact with the cooling water was assumed to be so efficient that the temperature was set to a constant 293 K as the boundary condition. The heat-conduction equation is then solved numerically in a two-dimensional finite element (FE) analysis (radius r and length z as co-ordinates).

As the maximum temperature in the crystal at intense pumping is believed to deviate greatly from the surrounding, temperature-dependent data of dn/dT is included (Paper III). At the reference temperature 300 K, dn/dT is then equal to 8.7×10^{-6} K^{-1}. In our example with a composite rod with undoped end-caps, the thermal expansion close to the end-surfaces is very low. Thus, the end-effect is neglected and the thermooptic coefficient in (2.83) is set equal to the thermal dispersion dn/dT.

Two different causes for degradation of beam quality in a laser medium are studied: first, an aberrated thermal lens, and then, a transversally varying saturated gain. In order to study an aberrated thermal lens and its influence on the degradation of beam quality, the effect of quartic phase aberrations on beam quality in a spherical lens is analysed. According to Siegman [29], when a laser beam with initial beam-quality factor M_i^2 propagates through a thermal lens of focal length f_{th} and quartic-aberration coefficient C_4, where the optical path difference OPD(r) from Eq. (2.82) is given by

$$\mathrm{OPD}(r) - \mathrm{OPD}(0) = -\frac{r^2}{2f_{th}} + C_4 r^4, \tag{4.2}$$

then the degradation in beam quality is given by the resultant beam-quality factor

$$M_r^2 = \sqrt{(M_i^2)^2 + (M_q^2)^2}, \tag{4.3}$$

where M_q^2 is the additional contribution to the beam-quality factor caused by the quartic phase-aberration effects. For a laser beam with Gaussian intensity profile it is given by

$$M_q^2 = \frac{4\pi C_4 w_L^4}{\lambda_L \sqrt{2}}. \tag{4.4}$$

Strictly, the analysis above is valid for a single-pass of a beam through a laser rod. In a laser resonator, the situation is more complicated with a double-pass per round-trip and with the gain profile acting as a spatial filter. Still, this model gives a rough estimation of the beam quality degradation caused by thermally induced phase aberrations.

With the standard *ABCD* method [30], the beam radius $w_{L,00}$ of the fundamental TEM_{00} mode in the laser cavity can be determined for a given focal length f_{th} of the thermal lens, calculated from the resulting OPD (4.2) from the finite element analysis. To treat the multimode behaviour in the same manner as the fundamental mode, the concept of the embedded fundamental mode is used. The multimode beam radius w_L is defined from the beam radius of the embedded fundamental mode $w_{L,00}$ as [30]

$$w_L = w_{L,00}\sqrt{M_L^2}, \tag{4.5}$$

where M_L^2 is the beam-quality factor of the multimode beam. In order to model how the laser beam is degraded when passing through a transversally varying saturated gain in the laser crystal, rather complicated calculations in a Fox and Li iteration procedure [12] could be done, where fast Fourier transform (FFT) methods are used and the saturated gain is acting as a soft spatial aperture [31]. Instead, a very simple method is suggested here. By studying Fig. 4.1, it is clear that it exists a preferred radius of the laser beam, which maximises the output power. On the other hand, if this laser-beam radius is small (smaller than the pump

radius), we know from Fig. 3.3 that higher-order modes are likely to oscillate due to gain saturation; that is the beam-quality factor is greater than one and hence from Eq. (4.5), the (multimode) laser-beam radius is increasing. Therefore, at steady-state, the laser mode is assumed to approach its preferred beam radius w_L, which maximises the output power, and then the beam-quality factor is calculated as

$$M_L^2 = \left(\frac{w_L}{w_{L,00}} \right)^2 , \tag{4.6}$$

where the fundamental mode radius $w_{L,00}$ is determined by the resonator design (and the power of the thermal lens). If the fundamental mode radius is greater than the preferred beam radius, only the fundamental mode is assumed to oscillate at $w_L = w_{L,00}$, and the beam-quality factor is set to one. The above model gives quite accurate results for the plane-plane cavity, since the optimum laser-mode size is increasing and the fundamental mode size is decreasing at high pump powers; that is the beam-quality factor is increasing in agreement with the experiments.

So far in this section, we have performed a theoretical investigation how to calculate the thermal lensing and the beam quality degradation in a laser crystal. Let us now return to the experimental example in Sect. 4.1 and start by investigating the radial dependence of the thermal properties in the laser crystal at maximum pump power 20.6 W (absorbed pump power 16.0 W), and for three different laser-beam radii w_L: 50, 100 and 200 µm. The population-inversion density is more saturated in the centre for smaller laser modes. Fig. 4.2 shows the corresponding fractional thermal loading ξ from Eq. (2.78). For a large laser mode w_L = 200 µm, the extra heat load from ETU is large in the centre (total generated heat 3.1 W).

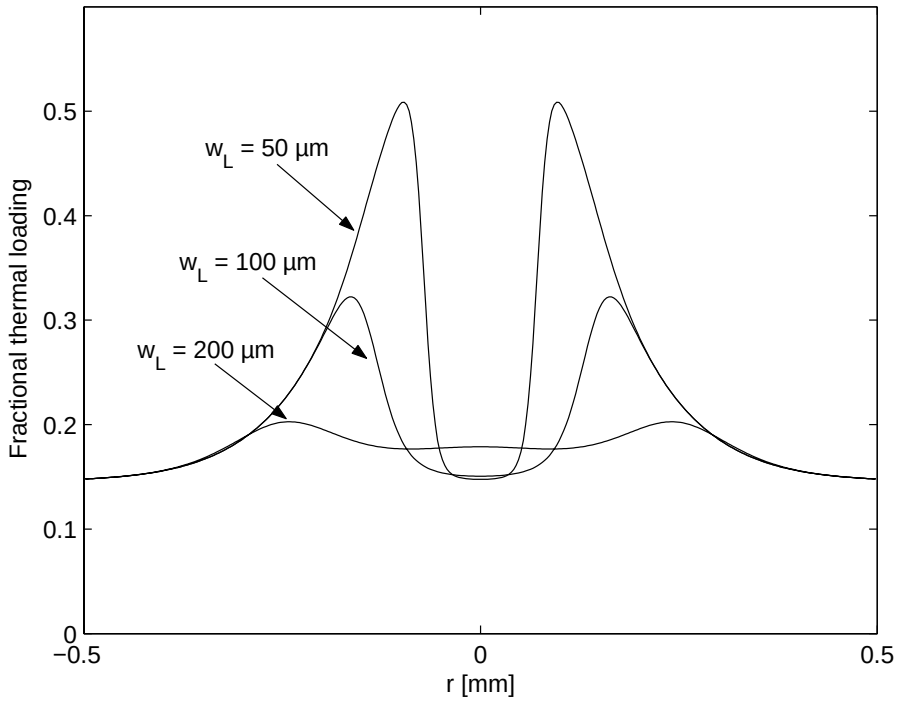

Fig. 4.2. Radial distribution of the fractional thermal loading ξ (integrated and taken as mean over z) under lasing conditions for 20.6 W of pump power and different values of laser mode radius w_L.

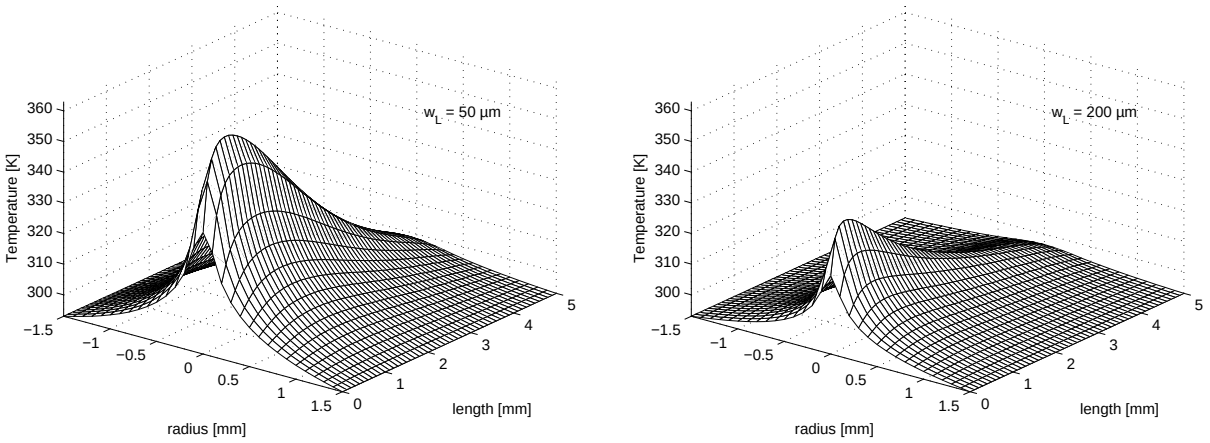

Fig. 4.3. Temperature distributions in the Nd:YAG crystal at 20.6 W pump power: (a) w_L = 50 µm, $T_{\max}$ = 361 K, (b) w_L = 200 µm, $T_{\max}$ = 334 K.

For w_L = 100 µm, the extra heat load is small in the centre and large in the wings quite far out from the pump distribution and the influence on the heat source density is therefore rather small (total generated heat 3.4 W). For a small laser mode w_L = 50 µm, the extra heat load is very large in the wings closer to the centre of the pump distribution, which gives a significant contribution to the heat source density in the wings (total generated heat 5.7 W). The heat conduction equation (2.80) was solved and the resulting temperature distributions are plotted for two cases in Fig. 4.3 (a)–(b). The temperature rise is greatest for w_L = 50 µm as expected from the high heat load (maximum temperature 361 K). For w_L = 200 µm, the maximum temperature is 334 K. The thermal lensing is calculated by using the optical path difference from Eq. (2.82), and making the polynomial fit in Eq. (4.2) over the range of the average pump radius w_P = 187 µm (dashed lines). The results for the focal lengths of the thermal lens are: f_{th} = 21 mm for w_L = 50 µm, f_{th} = 40 mm for w_L = 100 µm, and f_{th} = 30 mm for w_L = 200 µm. The measured thermal focal length was 35 mm at full power. The thermal lensing for w_L = 200 µm is stronger than for w_L = 100 µm, because OPD(r) gets more curved near the centre of the crystal, although the OPD in the centre is a little smaller in this case. Notice that the above polynomial fit gives slightly varying results for f_{th} and C_4 depending on how the radial range of OPD(r) is chosen. The interval over the average pump radius was chosen in order to cover as much as possible of the range where the thermal lensing is strong, while still keeping an accurate fit to the OPD.

We can now study the performance of the laser as a function of the laser-beam radius for different pump levels. We have already simulated the output power in Fig. 4.1. The corresponding thermal focal lengths are shown in Fig. 4.4. According to these calculations, for all pump levels there seems to exist a point where the thermal lens is weakest when there are ETU effects present. If ETU effects were not included, the thermal lensing would not have been dependent of the laser-mode size. The beam radius of the fundamental mode is calculated from the thermal lens and the resonator configuration with the *ABCD* method. From these calculations and Eq. (4.6), the degradation in beam quality from saturated gain effects is calculated and the result is shown in Fig. 4.5 (solid lines). The degradation in beam quality from thermally induced quartic phase aberrations, Eqs. (4.3) and (4.4), is shown as dashed lines, and it is seen that this effect gives a smaller influence on the beam-quality factor for moderate sizes of the laser beam. Thus, according to these calculations, the saturated gain profile is the cause for higher-order modes to oscillate, rather than thermally induced phase aberrations.

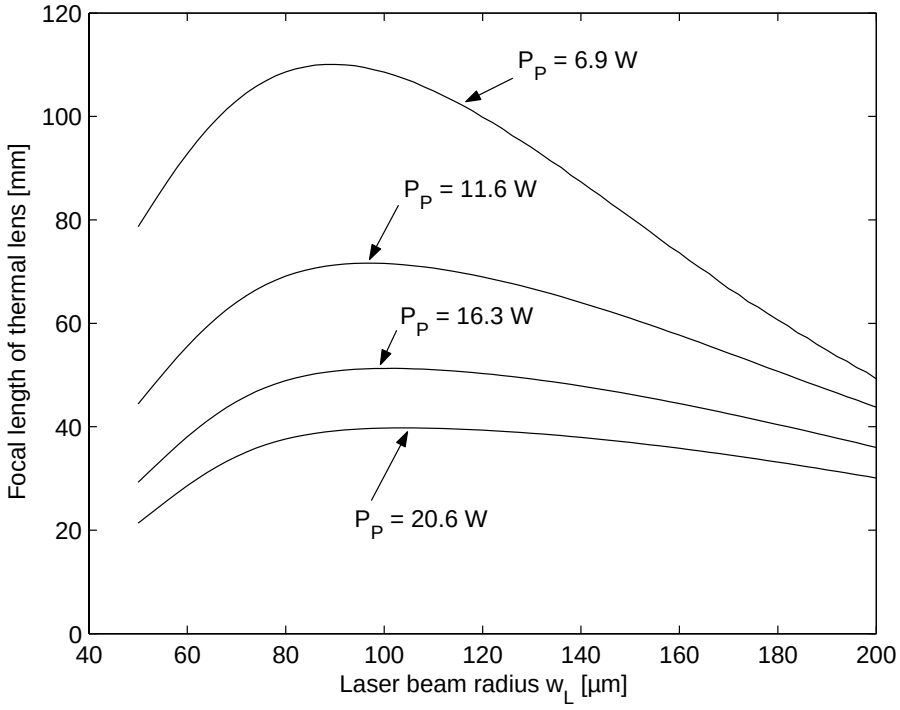

Fig. 4.4. Calculated focal length f_{th} of the thermal lens including ETU under lasing conditions at 946 nm versus laser mode radius w_L for different pump powers P_P.

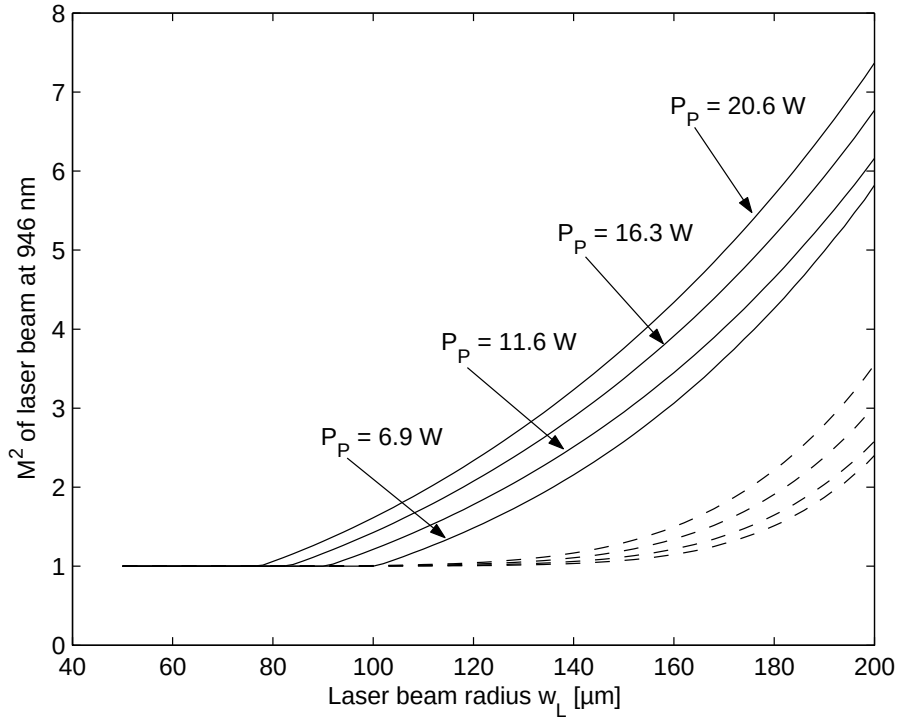

Fig. 4.5. Calculated beam-quality factor M^2 of the laser beam at 946 nm versus laser mode radius w_L for different pump powers P_P. *Solid lines*: degradation in beam-quality from saturated gain effects; *dashed lines*: degradation in beam-quality from thermally induced quartic phase aberrations.

We now have the tools to simulate the output performance and thermal effects of the laser at steady state as a function of pump power. For every pump level, the output power and thermal lensing are calculated for a range of laser-beam radii. Then, the multimode laser-beam radius is selected such that it optimises the output power (if the thermal lens is strong enough to accomplish this beam radius) and the corresponding thermal lens and beam quality are determined. In Fig. 4.6, the calculated output power is shown, together with the measured power from the experiments (circles) and a comparison with the calculated power where ETU effects are not included (dashed line). The simulations are in excellent agreement with the experiment with rather little difference from the case where ETU effects are not included. Figure 4.7 shows the dioptric power D_{th} of the thermal lens ($D_{th} = f_{th}^{-1}$). When upconversion is included, the thermal lensing is clearly stronger. The agreement with the experiments is quite good, at least for high powers. For low powers, the model presented might have overestimated the thermal lensing, but there were only four points measured, so the conclusions are quite uncertain. In addition, the slope of the measured thermal dioptric power seems to be steeper than the one calculated here. The modelling of the beam quality is in very good agreement with the measurements of this plane-plane resonator, as seen in Fig. 4.8. The calculations were made with a step of 2 W for the pump power and a step of 2 μm for finding the optimum multimode beam radius in Fig. 4.1, and there is a numerical error in the calculated output power of about ±0.005 W. If the optimum multimode beam radius w_L is determined within ±5 μm, the resulting error in the calculated beam quality is about ±0.3, explaining the roughness of the curve in Fig. 4.8.

In order to reduce the dependence of the thermal lensing and to control the laser-beam size, a linear cavity with a curved out-coupling mirror of radius 200 mm and transmission 6% was built (Paper II). The laser-beam size for this cavity is closer to the optimum size at high power (Fig. 4.1), than for the plane-plane cavity. While giving a high maximum laser power of 5.8 W at 946 nm, the beam-quality factor was improved to $M^2 = 1.7$.

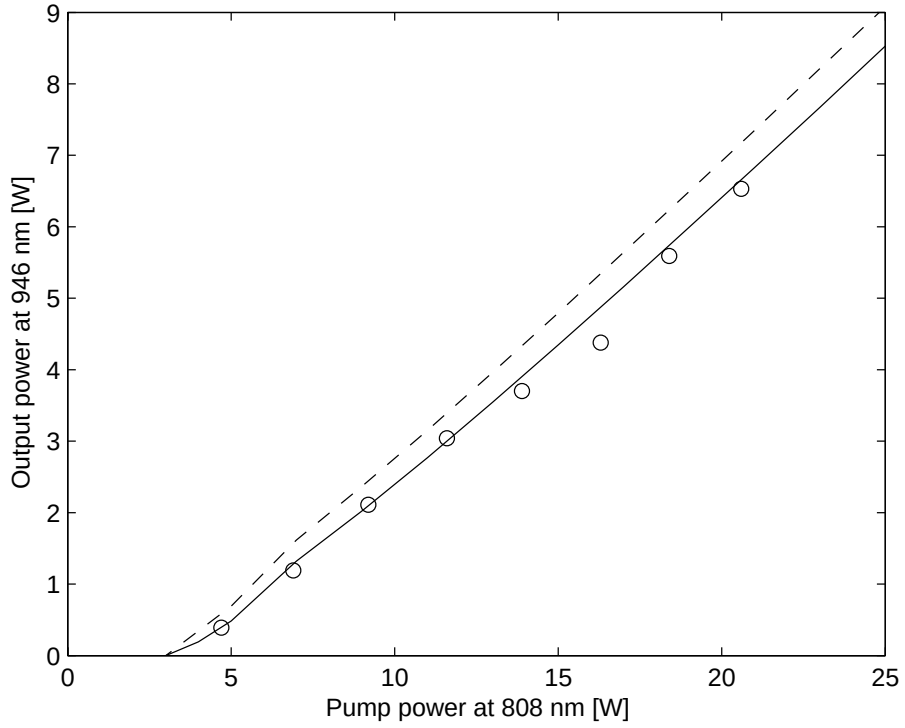

Fig. 4.6. Output power at 946 nm versus input power. *Circles*: measured power; *solid line*: calculated power including ETU; *dashed line*: calculated power not including ETU.

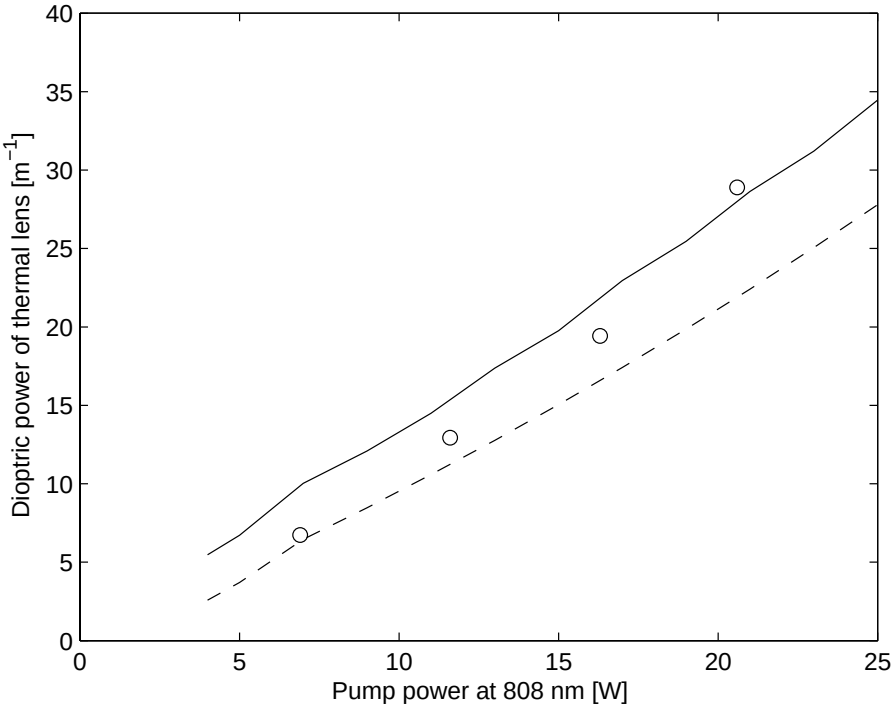

Fig. 4.7. Dioptric power D_{th} of the thermal lens under lasing conditions at 946 nm versus input power. *Circles*: measured values; *solid line*: calculated values including ETU; *dashed line*: calculated values not including ETU.

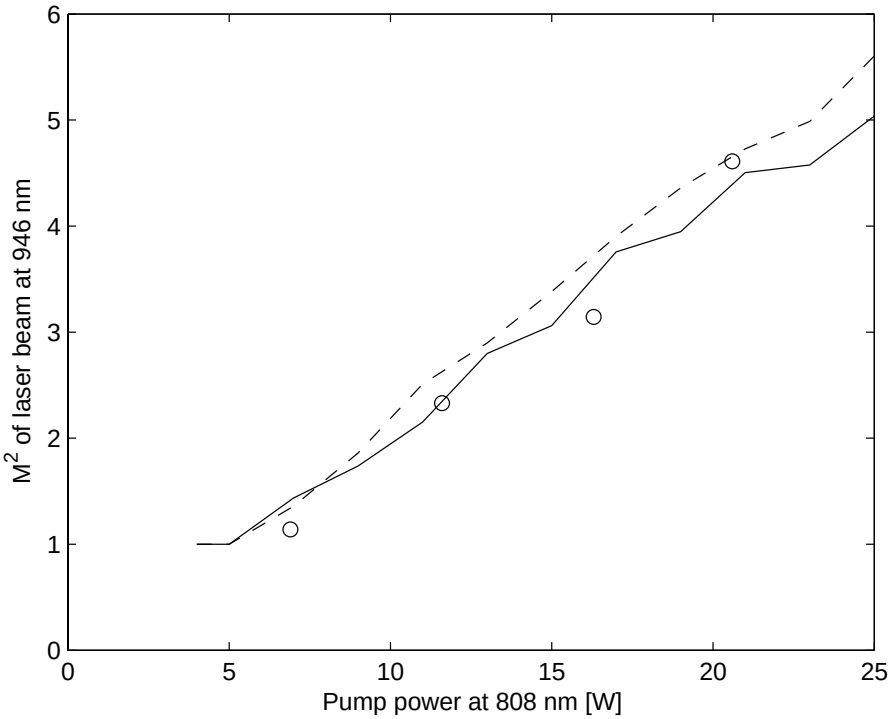

Fig. 4.8. Beam-quality factor M^2 of laser beam at 946 nm versus input power. *Circles*: measured values; *solid line*: calculated values including ETU; *dashed line*: calculated values not including ETU.

4.3 Frequency selection of the 938.5 nm transition in a Nd:YAG laser

Efficient operation of a Nd:YAG laser at 938.5 nm was reported in Paper I. The 938.5 nm and the 946 nm laser lines in Nd:YAG both have the same lower laser level (Fig. 1.1). The 938.5 nm line has a stimulated emission cross section of about 4.8×10^{-20} cm^2 [27], which is about 0.9 times that of the 946 nm line. Suppression of the much stronger transition at 1.06 µm can be achieved by using appropriate dielectric mirrors. To suppress lasing at the 946 nm line in favour of the 938.5 nm line, we have used frequency selection provided by an uncoated quartz etalon, inserted into the laser resonator as suggested in [32]. Selection of 938.5 nm (or 946 nm) laser operation was performed by simply tilting the 150 µm thick fused quartz etalon. Simultaneous operation of both laser lines at 938.5 nm and 946 nm could also be observed for certain tilt angles of the etalon.

The highest output power was achieved using a linear cavity with a concave output mirror with radius of curvature 200 mm and transmission 6%. Fig. 4.9 shows the output power for the 938.5 nm transition versus the incident pump power at room temperature. The average slope efficiency is 24% with respect to incident power. At high pump power at around 15 W, higher order modes started to lase, causing a slight degradation in beam quality. However, at maximum output power of 3.9 W (18.5 W of pump power) the beam was still close to diffraction limited ($M^2 = 1.4$). At even higher pump power above 18.5 W, the stronger laser lines 946 nm and 1064 nm started to oscillate, instead of the 938.5 nm.

The laser emission spectrum was investigated with an optical spectrum analyser and it was confirmed that there was no emission on the much higher gain transitions around 1.06 µm. The spectra showed a FWHM of ~ 0.3 nm for the 938.5 nm line (quite independent on the tilt angle of the etalon) as well as for the 946 nm laser with and without the etalon, with no significant change over the range of powers covered. This indicates that the etalon with a free spectral range (FSR = $\lambda^2 / 2nd$; n – refractive index, d – etalon thickness) of about 2 nm has acted as expected only as a line selector and not as a mode selector.

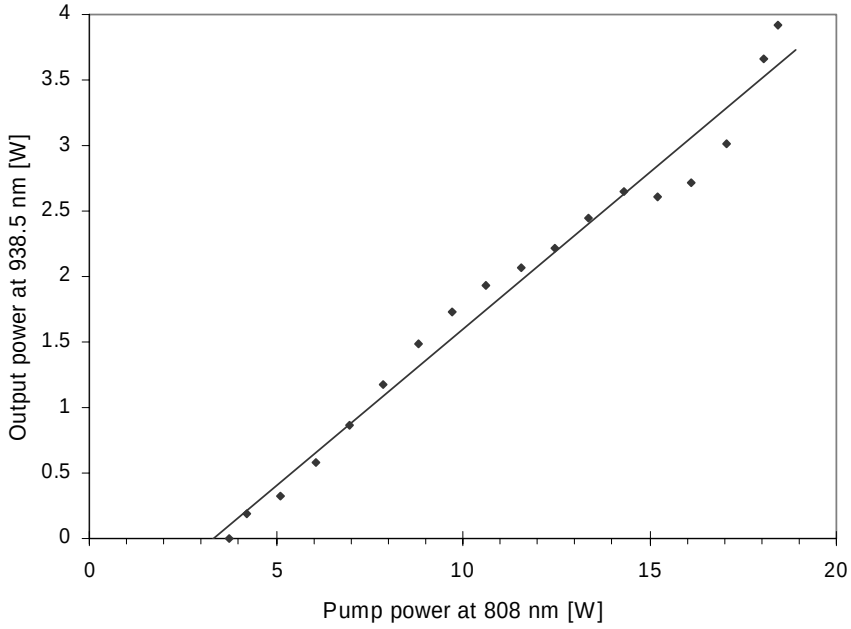

Fig. 4.9. Generated power at 938.5 nm versus input power.

4.4 Direct pumping of a 946 nm Nd:YAG laser

Traditional pumping at 808 nm into the $^4F_{5/2}$ pump band, above the upper laser level $^4F_{3/2}$, induces a parasitic quantum defect between the pump and the emitting laser levels. On the other hand, resonant pumping directly into the emitting level at either 869 nm (ground-state direct pumping) or 885 nm (thermally boosted pumping from thermally excited ground-state levels) reduces the total quantum defect between the pump and the laser emission wavelengths. This leads to a decrease in the heat generated in the laser material, thus reducing the thermal effects induced by optical pumping. Direct pumping of a 946 nm Nd:YAG laser provides an attractive alternative, because it reduces these thermal effects by a factor of around two compared to traditional pumping, as the quantum defect is 0.15 for 808-nm pumping, 0.08 for 869-nm pumping and 0.065 for 885-nm pumping, respectively.

For the four-level transition at 1064 nm in Nd:YAG, efficient laser emission has been reported in the last years for ground-state direct pumping at 869 nm and thermally boosted pumping at 885 nm under both Ti:sapphire and diode-laser pumping [33–36]. However, directly pumped lasers operating on the quasi-three-level transition at 946 nm have been reported under Ti:sapphire pumping only [37,38]. Here, we demonstrate for the first time a 946-nm Nd:YAG laser under direct pumping by diodes (Paper IV).

A fibre-bundle-coupled 869-nm diode laser from Spectra-Physics Lasers was used, in order to examine the performance of a 946-nm Nd:YAG laser under direct diode pumping. The fibre bundle consists of 19 fibres with a diameter of about 200 μm resulting in a total bundle diameter of 1.1 mm. The numerical aperture (NA) is 0.12, the maximum pump power after the pump optics is about 23 W, M^2 is about 160 and the spectral bandwidth is about 3 nm (FWHM) at 869 nm. The main disadvantage of resonant pumping is the lower absorption coefficient compared to that for traditional pumping at 808 nm. For a similar composite rod with a 5 mm long 1.1% Nd:YAG middle section used in Sect. 4.1, we measured the absorption coefficient of the pump diode at 869 nm to be 0.97 cm^{-1} (38%

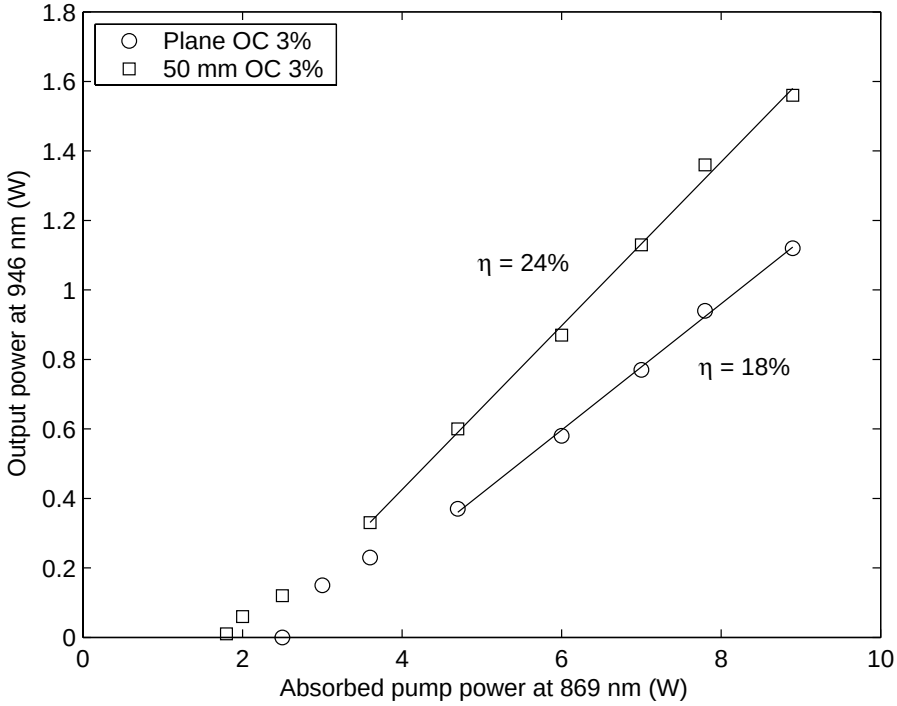

Fig. 4.10. Output power at 946 nm vs. absorbed pump power for direct pumping at 869 nm.

absorption). The reabsorption loss in a quasi-three-level laser makes longer crystals aiming at an enhanced absorption of the pump unsuitable for the 946-nm laser. The reabsorption loss at threshold for this 5 mm long crystal is 5.7% (Sect 4.1).

We focused the pump beam to around 200 µm inside the water-cooled composite crystal and a two-mirror cavity with a plane in-coupling mirror was employed. The results are presented in Fig. 4.10 for the two out-coupling mirrors we tested. The resonator length was 28 mm for both OC mirrors. For a plane OC with 3% transmission at 946 nm, the absorbed power threshold was about 2.5 W and the maximum output power at 946 nm was 1.1 W. The slope efficiency with respect to absorbed pump power was about 18%. For a concave OC with 50 mm radius of curvature and 3% transmission, the absorbed power threshold was about 1.8 W and a maximum output power of 1.6 W at 946 nm was achieved. The slope efficiency with respect to absorbed power is now about 24%.

The slope efficiencies are rather low, much lower than the Stokes efficiency $\eta_S = \lambda_P / \lambda_L$ (0.92), and the reason for this is that the round-trip loss of these cavities (about 1.5%) is quite high with respect to the relatively low out-coupling (3%) and that the mode overlap is not optimised. The slope efficiency for a quasi-three-level laser with respect to absorbed power η_{o-a} can be written with a similar expression to Eq. (2.58) as [15]

$$\eta_{o-a} = \frac{T}{T+L}\eta_S \frac{dS}{dF}, \tag{4.7}$$

where dS / dF is the normalised slope efficiency with respect to the normalised F (3.5) and S (3.6) parameters. dS / dF depends on the overlap between the pump mode and the laser mode, the saturable reabsorption loss and the pump intensity. From Eq. (4.7), we can calculate dS / dF to 39% for the direct-pumped laser with highest output power. For comparison, we see that the 946-nm laser pumped at 808 nm in Sect. 4.1 with $\eta_{o-a} = 48\%$ has a normalised slope efficiency of 74%. The tighter focusing of the 808-nm pump diode resulted in an almost two times higher dS / dF, which shows the importance of a high-brightness pump diode.

5 Generation of blue light by second harmonic generation

5.1 Introduction

In this chapter, the quasi-three-level laser at 946 nm in Nd:YAG is used for generation of blue light in periodically poled $KTiOPO_4$ (PPKTP). A summary of nonlinear optics, second harmonic generation and quasi-phasematching in PPKTP is presented here. A more detailed description of the nonlinear optics and the manufacturing of PPKTP can be found in [39,40].

5.2 Nonlinear optics

The interaction between an electromagnetic wave and a dielectric material results in an induced polarisation field in the material. Normally, the response is linear, so that several waves can propagate through the material without any interaction with each other. However, at high field intensities, the waves will disturb the electron cloud and the induced polarisation will exhibit nonlinear properties, the polarisation Cartesian components P_i are then expressed as a series expansion

$$P_i = \varepsilon_0 \chi_{ij}^{(1)} E_j + \varepsilon_0 \chi_{ijk}^{(2)} E_j E_k + \varepsilon_0 \chi_{ijkl}^{(3)} E_j E_k E_l + \ldots, \tag{5.1}$$

where E_j is the electric field components, ε_0 is the permittivity in vacuum, $\chi_{ij}^{(1)}$ is the linear susceptibility tensor and $\chi_{ijk\ldots}^{(n)}$ are the higher order nonlinear susceptibility tensors. The second-order nonlinear susceptibility $\chi_{ijk}^{(2)}$, which can only exist in materials that lack a centre of inversion, is responsible for many interesting effects. Several waves of different frequencies can interact with each other in the material, under the condition of energy conservation. In this way, it is possible to obtain frequency conversion. There are mainly two types of frequency-conversion processes (Fig. 5.1): (1) two input photons are added or subtracted into one photon of higher or lower energy; this process includes second harmonic generation (SHG), sum frequency generation (SFG) and difference frequency generation (DFG), (2) one input photon results in two photons of lower energies; this process includes optical parametric oscillation (OPO), optical parametric amplification (OPA) and optical parametric generation (OPG). In this thesis, only second harmonic generation is used.

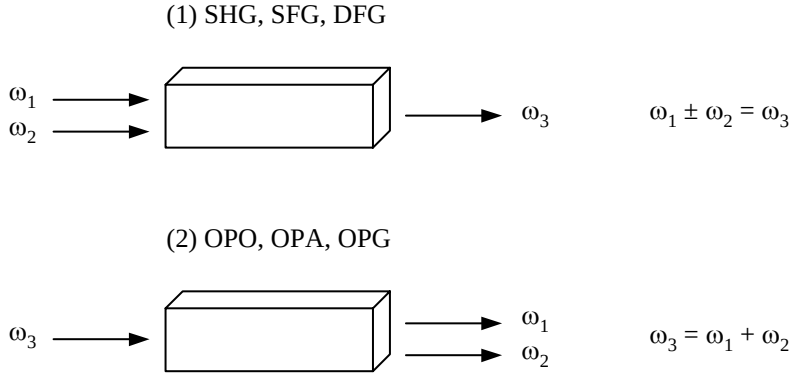

Fig. 5.1. Frequency conversion processes in a second-order nonlinear medium.

The second-order susceptibility is often replaced by the second-order nonlinear *d*-tensor:

$$\chi_{ijk}^{(2)} = 2d_{ijk}\,. \tag{5.2}$$

The d_{ijk}-tensor can be reduced to a 3 × 6-element matrix [13]. Assuming plane waves in the *z*-direction in the material and invoking the slowly varying envelope approximation, Maxwell's equation for an electromagnetic wave will be reduced to [13]

$$\frac{dE_1}{dz} = -\alpha_1 E_1 - \frac{i\omega_1}{2n_1 c} d_{\text{eff}} E_3 E_2^* e^{-i\Delta k\, z}\,, \tag{5.3}$$

$$\frac{dE_2}{dz} = -\alpha_2 E_2 - \frac{i\omega_2}{2n_2 c} d_{\text{eff}} E_3 E_1^* e^{-i\Delta k\, z}\,, \tag{5.4}$$

$$\frac{dE_3}{dz} = -\alpha_3 E_3 - \frac{i\omega_3}{2n_3 c} d_{\text{eff}} E_1 E_2 e^{i\Delta k\, z}\,, \tag{5.5}$$

where E_1 and E_2 are two incident fields at frequencies ω_1 and ω_2, generating a third field E_3 at frequency $\omega_3 = \omega_1 \pm \omega_2$, α_i are the loss coefficients, n_i are the refractive indices at frequency ω_i, d_{eff} is the effective nonlinear coefficient and Δk is the *phase mismatch*

$$\Delta k = \frac{n_3\omega_3}{c} - \frac{n_2\omega_2}{c} - \frac{n_1\omega_1}{c}, \tag{5.6}$$

which is a key factor for the efficiency of a nonlinear process.

5.3 Second harmonic generation

In the case of second harmonic generation (SHG), the generated frequency is twice the fundamental frequency, $\omega_{SH} = 2\omega_F$, and Eq. (5.5) then becomes in a loss-less medium

$$\frac{dE_{SH}}{dz} = -\frac{i\omega_{SH}}{2n_{SH} c} d_{\text{eff}} E_F^2 e^{i\Delta k\, z}\,, \tag{5.7}$$

which has the solution for the generated power ($P_{SH} = n_{SH}\varepsilon_0 c E_{SH} E_{SH}^* / 2 \times A$)

$$P_{SH} = \frac{8\pi^2 d_{\text{eff}}^2 L^2}{n_F^2 n_{SH} \lambda_F^2 \varepsilon_0 c A} P_F^2 \,\text{sinc}^2\left(\frac{\Delta k\, L}{2}\right), \tag{5.8}$$

where L is the length of the crystal, A is the beam spot area and λ_F is the wavelength of the fundamental wave. The second harmonic power is quadratic to the fundamental power and to the length of the crystal and has the sinc^2 dependence as shown in Fig. 5.2.

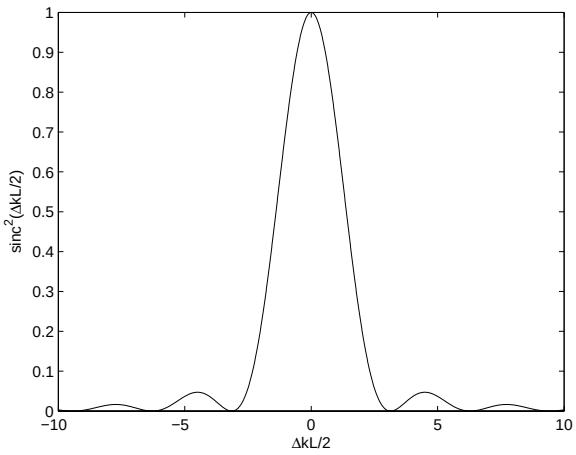

Fig. 5.2. Second harmonic power dependence of phasematching.

For Gaussian beams, the optimal focusing can be obtained by using the Boyd-Kleinman analysis for SHG with circular beams [41]. With the focusing parameter ξ, this analysis imposes that the beam waist w_0 inside the crystal should be

$$w_0^2 = \frac{\lambda_F L}{2\pi n_F \xi}. \tag{5.9}$$

If there is no birefringent beam walk-off in the crystal, the optimal focusing for maximum SHG power is when $\xi = 2.84$.

5.4 Quasi-phasematching

The sinc^2 behaviour of the second harmonic power (5.8) requires that the phase mismatch Δk is zero for optimum conversion efficiency. For SHG, the phase mismatch (5.6) is

$$\Delta k = \frac{2\omega_F (n_{SH} - n_F)}{c}, \tag{5.10}$$

and the phasematching condition $\Delta k = 0$ is normally not fulfilled due to material dispersion. The length L_c inside the crystal, which yields a phase mismatch of π is called the coherence length

$$L_c = \left| \frac{\pi}{\Delta k} \right|. \tag{5.11}$$

At this point forward, the energy will start to flow from the second harmonic wave back to the wave at the fundamental frequency. One way to obtain high conversion efficiency over long crystal lengths is to use anisotropic materials' birefringence properties in birefringent phasematching. In this thesis, *quasi-phasematching* in periodically poled KTP has been used instead. A strong applied modulated electric field can flip the ferroelectric domains inside the crystal so that the effective nonlinearity alters between $-d_{\text{eff}}$ and $+d_{\text{eff}}$. When the accumulated phase mismatch reaches π, the sign of the driving nonlinear susceptibility is reversed so that the phase mismatch is set to zero. This creates a stepwise growth in the output power along the crystal length as can be seen in Fig. 5.3.

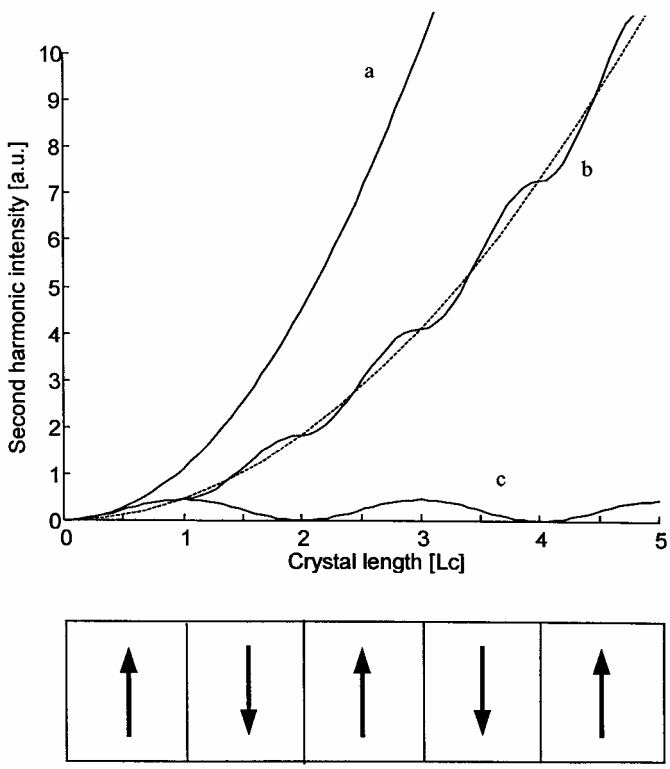

Fig. 5.3. Second harmonic generation in a material with different phasematching conditions: (a) perfect phasematching, $\Delta k = 0$, throughout the entire crystal; (b) first-order quasi-phasematching in a crystal where the spontaneous polarisation is reversed every coherence length; (c) the material has no phasematching at all. The dotted line is "line (a)" multiplied by the appropriate factor $(2/\pi)^2$ for first order QPM [40].

Quasi-phasematching is obtained when the period Λ of the modulation is chosen such that one of the spatial harmonics compensates for the phase mismatch [33]:

$$\Lambda = m\frac{2\pi}{\Delta k}, \tag{5.12}$$

where $m = 1, 2, \ldots$ is the order of the QPM process. There are two types of phasematching: in type-I, both the incident photons have the same polarisation; in type-II, the polarisation vectors are orthogonal. The effective nonlinear coefficient for type-I QPM in PPKTP is given by

$$d_{\text{eff}} = \frac{2}{m\pi} d_{33} \sin m\pi D, \tag{5.13}$$

where $D = L_p / \Lambda$ is the duty-cycle of a rectangular structure, where L_p is the length of the section that has a positive sign of the nonlinear coefficient. Obviously, the largest value d_{eff} is obtained for first-order QPM with a duty-cycle of 50%. Such crystals were used in this thesis.

QPM crystals are normally temperature-tuned, since both the crystal length L and the phase mismatch (5.10) in the sinc^2 function in Eq. (5.8) are temperature dependent. According

to Fejer *et al.* [42], the SHG power of the temperature-tuned crystal follows the sinc^2 shape of Fig. 5.2 with a FWHM acceptance bandwidth

$$\Delta T = \frac{0.4429\lambda_F}{L}\left[\frac{\partial n_{SH}}{\partial T} - \frac{\partial n_F}{\partial T} + \alpha_T (n_{SH} - n_F)\right]^{-1}, \qquad (5.14)$$

where α_T is the thermal expansion coefficient of the material.

5.5 Intracavity second harmonic generation

Instead of SHG with a single pass of the fundamental laser beam through the nonlinear crystal, it is of interest to make SHG in an intracavity configuration in order to utilise the high internal intensity and enhance the conversion efficiency. A *Z*-folded four-mirror cavity as shown in Fig. 5.5, enables the necessary separate optimisation of the laser resonator mode in the laser crystal and in the nonlinear crystal. A problem reported with intracavity-doubled lasers with several longitudinal modes is large amplitude fluctuations and longitudinal mode instabilities, known as the "green problem" [43]. The instabilities arise from coupling of the longitudinal modes by sum-frequency generation in the nonlinear crystal.

5.6 Frequency doubling of Nd:YAG lasers to 473 nm

For efficient frequency doubling to blue light at 473 nm of the laser light at 946 nm, we used periodically poled KTP (Paper II). In an early experiment, single-pass extra-cavity second harmonic generation was done. By inserting a thin Brewster plate polariser into a simple plane-plane cavity, we selected a linear polarised output with a maximum power of 2.75 W. The output mirror transmission was 6%. The rather low output power could be due to the poor optical quality of the glass plate used as a Brewster plate at this time.

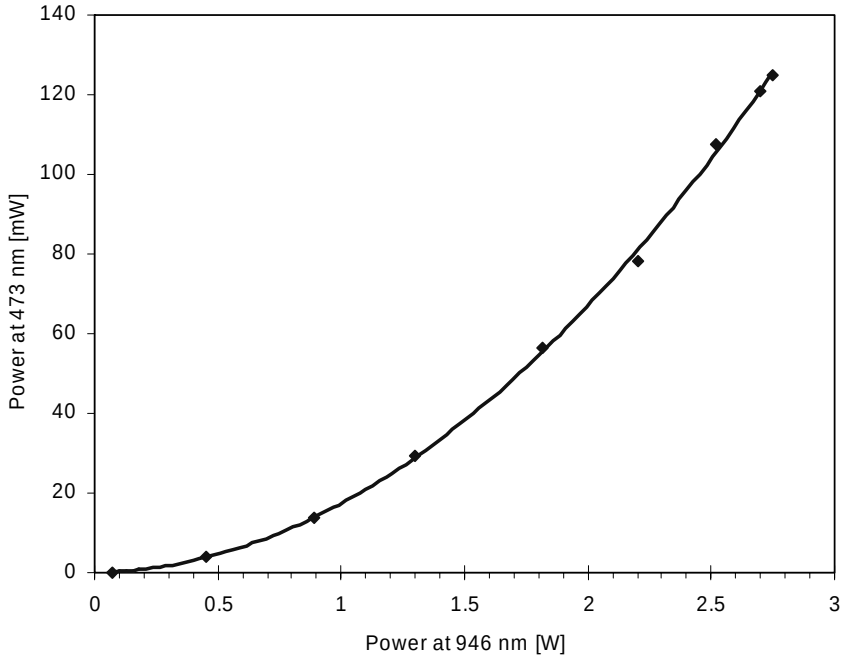

Fig. 5.4. Generated power at 473 nm versus fundamental power for single-pass extra-cavity frequency doubling.

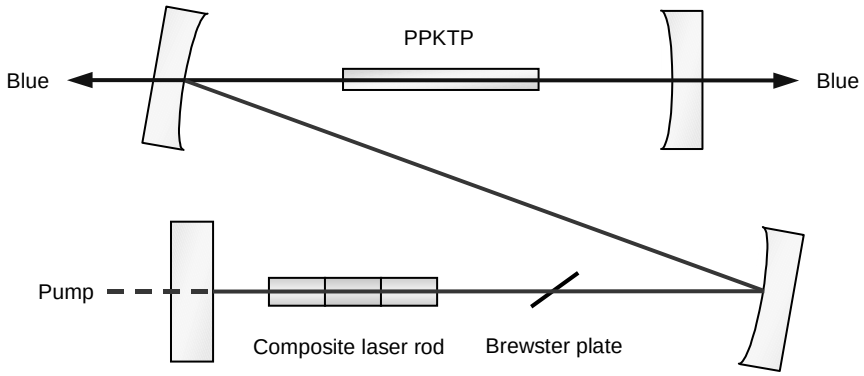

Fig. 5.5. Schematic laser resonator design for intracavity frequency doubling.

The uncoated PPKTP crystal had dimensions $20 \times 5 \times 1$ mm (Cobolt AB). The 946 nm radiation was focused in the doubling crystal using an $f = 100$ mm lens. Fig. 5.4 shows the CW power at 473 nm versus incident fundamental power, revealing a dependence close to the expected quadratic behaviour. The operating temperature for first-order quasi-phasematching was about 29 °C. Taking into account the Fresnel losses, the maximum internal power at the fundamental wave was 2.4 W (2.6 W incident) and the maximum internal power at 473 nm was 135 mW (125 mW external). From these values, a normalised conversion efficiency of 1.2% $W^{-1}cm^{-1}$ can be deduced.

For intracavity frequency doubling, we used a four-mirror cavity as schematically depicted in Fig. 5.5. This cavity type enables the necessary separate optimisation of the laser-resonator mode in the laser crystal and in the nonlinear crystal. A thin quartz etalon was used as a Brewster plate for selection of polarised light. The frequency doubling crystal used this time was a PPKTP crystal with dimensions $20 \times 2 \times 1$ mm (period $\Lambda = 6.09$ µm for first-order QPM) and it was AR-coated at both 946 nm and 473 nm (Cobolt AB). We achieved a CW power of more than 0.5 W at 473 nm in total output from two mirrors operating the PPKTP at a temperature of about 24 °C. We measured the beam-quality to $M^2 = 5$. The output light showed a quite stable behaviour (about 7% maximum power deviation over a few minutes) and did not show any large amplitude fluctuations on the very short time scale ("green problem") [43]. The length of the resonator was in the order of 30 cm.

We believe that the laser mode neither in the nonlinear crystal, nor in the laser crystal was fully optimised. This resulted in a relatively low SHG power compared to the unpolarised 6–7 W at 946 nm we have achieved in two-mirror cavities (Paper II). The work with blue lasers was done in 2001, but then we had a failure of our pump source and after that, the work with blue lasers has not been continued.

5.7 Frequency doubling of Nd:YAG lasers to 469 nm

By single-pass extra-cavity frequency doubling of the laser from Sect. 4.3 in a periodically poled KTP crystal, we achieved a maximum CW power of 88 mW at 469 nm (Paper I). The PPKTP had dimensions $15 \times 2 \times 1$ mm and was AR-coated at both 938.5 nm and 469 nm (Cobolt AB). The unpolarised 938.5 nm radiation was focused in the doubling crystal using an $f = 100$ mm lens. The operating temperature for first-order quasi-phasematching (period $\Lambda = 5.90$ µm) was about 45 °C. The SHG power as a function of crystal temperature followed the expected sinc^2 shape, and the bandwidth FWHM was about 3 K. From the fundamental power having the proper polarisation for type-I SHG (2 W), the SHG power, and the crystal length, a normalised conversion efficiency of 1.4% $W^{-1}cm^{-1}$ can be deduced.

For intracavity frequency doubling, we used a similar four-mirror cavity as in Fig. 5.5, but with the etalon line selector present instead of the Brewster plate. The frequency-doubling crystal was a PPKTP crystal from the same batch as the one described above (period $\Lambda = 5.90$ µm, AR-coating at both 938.5 nm and 469 nm) but it was shorter than the one used for single-pass frequency doubling. The PPKTP had dimensions $5 \times 2 \times 1$ mm. We achieved a CW power of slightly more than 200 mW at 469 nm in total output from two mirrors operating the PPKTP at room temperature.

6 Miniature lasers using silicon and polymer microbenches

As it is a goal to make the our lasers compact, miniature Nd:YAG lasers in micro-structured carriers have been developed. Monolithic microchip lasers are compact, miniaturised lasers in a crystal medium, originally about 0.5 mm in length to achieve single-mode operation (as the mode separation is then longer than the spectral gain bandwidth), but have later been extended to lengths of several millimetres. They have a flat-flat cavity with mirrors deposited directly on the crystal surfaces. The monolithic microchip laser concept was invented by Zayhowski and Mooradian at Lincoln Laboratory, MIT around 1988 [44]. As the cavity is flat-flat and no beam-shaping elements are present in the cavity that can confine the beam, the stability of the laser resonator will be determined by thermal effects and gain gradients. Especially for high pump powers, the thermal effects will be significant, leading to distortion of the laser mode and even fracture of the crystal. Therefore, the laser must be efficiently cooled at high powers.

An optical microbench concept has been developed at Acreo and KTH [45]. It consists of an etched V-groove in a silicon carrier, where crystals diced from mirror-coated wafers in rhombic shapes to fit in the V-groove are used. Using wet-etching, the V-grooves have a bottom angle of 70.5º. The crystals are 3 to 4 mm long and has a cross-section of 1 mm (Fig. 6.1). For good thermal contact, an evaporated indium-film is used to fix the crystal in the V-groove. The large heat conductivity of silicon (160 $Wm^{-1}K^{-1}$) provides efficient thermal management. A second silicon carrier with a matching V-groove is placed on top. Using this concept, a continuous-wave power of 6.7 W at 1064 nm has been achieved. Several optical elements can be placed and aligned in a silicon carrier, which provides for a cost-effective way of passive alignment and compact integration. Nd:YAG crystals diffusion-bonded with undoped end-caps at the in-coupling side and Cr^{4+}:YAG saturable absorbers bonded at the out-coupling side were used in Paper VI for Q-switched operation. An average power of 2 W and a pulse length of 1.4 ns were obtained.

Recently, the concept was expanded to carriers in polymer materials by Evekull *et al.* in Paper V. The advantages of a polymer carrier over the silicon carrier are the low cost of the material itself and the simplified processing. Since standard injection moulding techniques can be used for the handling, large production volumes at a very low cost are possible at the same time as there is total design freedom of the carrier structure in terms of complexity. The drawback of using polymers compared to silicon is the somewhat lower heat conductivity,

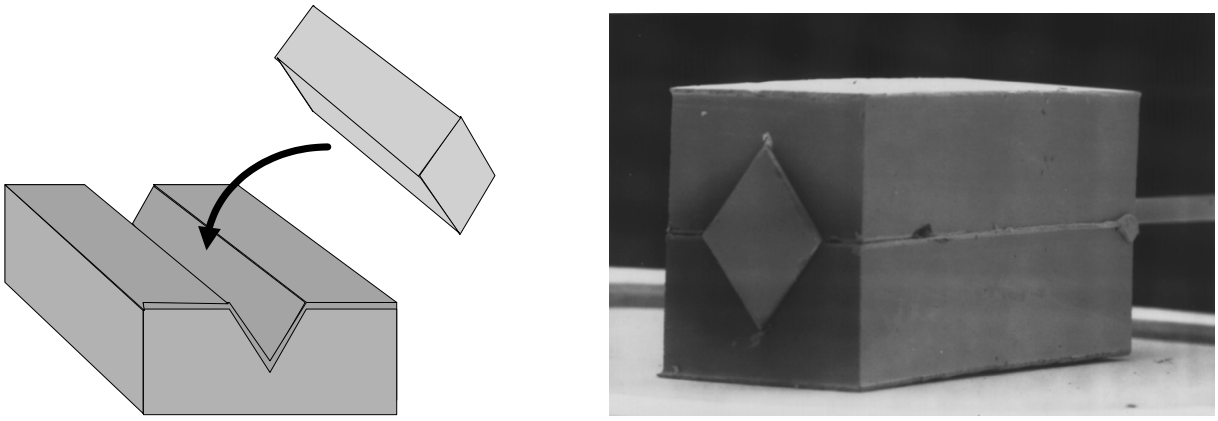

(a) **(b)**

Fig. 6.1. (a) Mounting of rhombic laser crystal in silicon V-grooves. (b) SEM photograph of rhombic Nd:YAG crystal mounted in silicon carrier.

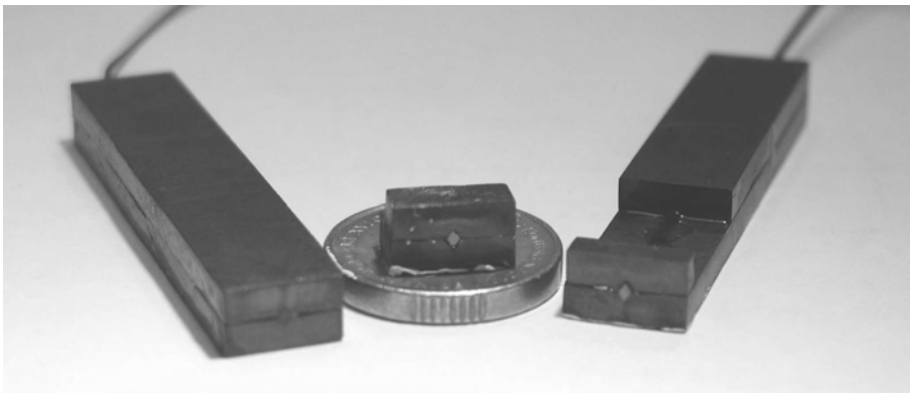

Fig. 6.2. Three different polymer carrier lasers.

which increases the thermal stress on the laser crystal. But still, the heat conductivity for the specific polymer used for the carrier is considerably larger (20 $Wm^{-1}K^{-1}$) than for traditional polymers (0.2 $Wm^{-1}K^{-1}$). Polycarbonate carriers with single V-grooves along the long-axis were manufactured. The rhombic-cut Nd:YAG laser crystal used for the experiments was 3 mm long. The fibre from the pump diode was also encapsulated in the polymer carrier and the end of the fibre was placed as close to the facet of the Nd:YAG crystal as possible. The result is a compact and robust miniature laser, as shown in Fig. 6.2. An output power of 2 W at 1064 nm was achieved.

7 $KRE(WO_4)_2$ double-tungstate crystals

In the EU project DT-CRYS, rare-earth-doped double-tungstate crystals $KRE(WO_4)_2$ (RE = rare earths like Gd, Y and Yb) are studied. Our part at KTH, has so far involved KGW and KYW with some of the Gd or Y substituted by Er and Yb. The crystals have been grown by our EU-project partner in Prof. F. Díaz's group at Universitat Rovira i Virgili (URV) in Tarragona. A short description of the growth procedure is described below.

The rare-earth potassium tungstates KREW crystallise in the monoclinic system with space group *C*2/*c*. Their unit cell parameters are reported in Table 7.1. Er^{3+}-doped and Er^{3+}, Yb^{3+} codoped KGW, KYW and undoped KYbW crystals with several doping concentrations used in this work were grown at URV by means of the Top-Seeded Solution Growth slow-cooling method (TSSG) as described in [46]. The solutions used, weighting about 195–200 g, were prepared in a cylindrical platinum crucible. The axial and radial temperature gradients in the solution were 0.1 K/mm and the saturation temperatures were in the range of 1170–1200 K. The crystals grew by a seed parallel to the **b** crystallographic direction, without inclusions or any macroscopic defects. During the growth, the seed rotates at 60 rpm, without pulling. The crystals were removed slowly from the solution and cooled to room temperature at 15 K/h after 8 days of growth. The average growth rate was around 2×10^{-2} g/h. Inclusion-free crystals of around 5 g and average dimensions of 10.5 mm × 6 mm × 14 mm along the **a*** × **b** × **c** crystallographic directions, were obtained with the described conditions. Some commercial Yb-doped KGW and KYW crystal were also included in the experiments.

The double-tungstate monoclinic crystals have a rather large anisotropy in the optical and thermal characteristics. The three orthogonal optical axes N_m, N_p and N_g are characterised by strongly differing emission and absorption spectra, refractive indices and thermooptic coefficients. The largest absorption and emission cross sections are observed for light polarised along the N_m axis, which for KYbW is rotated 19° clockwise from the crystallographic **c** axis (Fig. 7.1).

Host crystal	*a* (Å)	*b* (Å)	*c* (Å)	*β* (°)	Ref.
KGW	10.652(4)	10.374(6)	7.582(2)	130.80(2)	[47]
KYW	10.64	10.35	7.54	130.5(2)	[48]
KYbW	10.590(4)	10.290(6)	7.478(2)	130.70(2)	[49]

Table 7.1. Unit cell parameters of KREW (RE = Gd, Y and Yb).

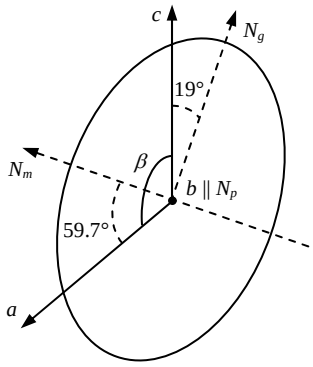

Fig. 7.1. Optical ellipsoid for KYbW [49].

8 Efficient diode-pumped Yb:KGW lasers

8.1 Yb-doped double tungstates

With the development of powerful InGaAs laser diodes emitting around 940 nm and 980 nm [14], Yb^{3+}-doped materials like Yb:YAG have been recognised as candidates for highly efficient laser systems. Like the 946-nm Nd:YAG laser, the Yb-doped hosts are quasi-three-level systems, but the energy-level diagram is very simple and consists of only two manifolds: the $^2F_{7/2}$ ground state and the $^2F_{5/2}$ excited state. The laser wavelength is around 1.03 μm, which gives a very small quantum defect and this, together with the absence of upconversion and excited-state absorption, results in high slope efficiencies.

During recent years, a substantial interest has been shown in Yb^{3+}-doped double-tungstate crystals like KGW and KYW. The double-tungstate crystals exhibit an attractive set of parameters, which makes them one of the best choices for laser-diode end-pumped solid-state lasers operating around 1 μm [50–53]. Moreover, the broad gain bandwidth obtainable in these crystals enables both a significant tuning range [53] and mode-locked femtosecond pulse generation [54,55]. The possibility to achieve high doping concentrations opens up the possibility for thin-disc laser applications [56,57]. Although the thermal conductivity in Yb:KGW and Yb:KYW is about three times lower than in Yb:YAG, it is nevertheless higher than in Yb:glass or many borate hosts such as GdCOB and YCOB [58]. This indicates quite good prospects for output power scalability. In Paper VII described in the next section, a comparative study between Yb:KGW crystals with crystallographic **b** orientation and a novel athermal orientation [59,60] is performed.

8.2 Laser performance and thermal lensing in Yb:KGW with athermal orientation

One of the major issues for end-pumped solid-state lasers is the management of thermal lensing and thermal beam distortions. The thermal expansion in Yb:KGW is anisotropic with eigenvalues of 6.3×10^{-6} K^{-1}, 2.4×10^{-6} K^{-1} and 21.7×10^{-6} K^{-1} [60], along the axes X_1', X_2' and X_3', respectively, where X_3' is rotated 12° counter-clockwise from the crystallographic **c** axis [47]. Considering this anisotropy, the orientation of the laser crystals becomes an important issue for optimisation in these systems.

Many of the Yb:KGW crystals earlier reported in laser systems have been cut for propagation along the **b** crystallographic direction, which is parallel to N_p, giving access to the largest absorption and emission cross sections. However, based on recent measurements of the thermooptic coefficients dn/dT and thermal-expansion coefficients α (Table 8.1) using homogeneous heating, Biswal *et al.* [59,60] proposed some possible athermal propagation directions, where the thermooptic and thermal-expansion effects approximately cancel each other. One of the proposed directions for light polarised along the N_p axis is in the m-g plane, 15°–17° clockwise from the optical axis N_m [60,61]. The uncertainty in the athermal direction stems primarily from the uncertainty in the reported directions of the thermal-expansion axes.

Optical axis	α (10^{-6} K^{-1}) with **k** ‖	dn/dT (10^{-6} K^{-1}) with **E** ‖
p	2.4	–15
m	11	–10
g	17	–16

Table 8.1. Thermal-expansion coefficients α and dn/dT in the anisotropic crystal KGW [60].

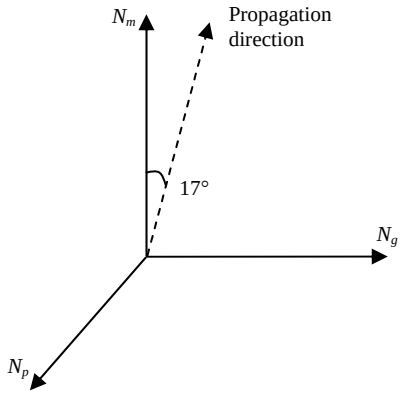

Fig. 8.1. The direction of athermal propagation in the frame of KGW crystallooptic axes.

We have investigated the properties of thermal lensing and thermal beam distortions in high-power diode-end-pumped Yb:KGW crystals cut for beam propagation along the b-axis and along the above mentioned athermal direction. Two 5 at.% doped Yb:KGW crystals used were cut in 3 × 3 × 3 mm cubes with AR-coated end faces in the respective propagation directions. The first crystal, the *b-cut* crystal, was cut with the crystallographic direction **b** as the propagation direction. The second crystal, the *ad-cut* (athermal-direction cut) crystal, was cut with the propagation direction at an angle of 17° clockwise from the optical direction N_m as shown in Fig. 8.1. The optical surfaces of the crystals were antireflection coated at the pump and the laser wavelengths, and the crystals were contacted using indium-foil with a water-cooled copper heat sink. The pump laser-diode bar (LIMO GmbH) produced a maximum output power of 23.4 W at a wavelength of 979.5 nm with a FWHM spectral width of 2.4 nm. The output of the pump laser was 95% linearly polarised. The pump beam was focused through a plane in-coupling mirror to $1/e^2$ widths of 200 μm × 150 μm in the laser crystal. The intensity distribution of the pump was almost Gaussian along the 150 μm dimension and close to a top-hat along the other dimension. The IC mirror was coated for high reflectivity in the 1020–1200 nm wavelength region and AR-coated for the 810–980 nm range. The complete set of optics transmitted a maximum power of 19.3 W into the laser crystal. The linear laser cavity was completed by a concave, 50 mm radius of curvature output coupler with 95% reflectivity. The length of the laser cavity was 17 mm.

The b-cut crystal was pumped by the diode beam polarised along the optical direction N_m, which has the highest absorption cross section. The ad-cut crystal, on the other hand, had maximum absorption for the laser diode polarised parallel to the N_p direction. Under nonlasing conditions the maximum absorption in the b-cut crystal was about 84%, while in the ad-cut crystal it reached only 42%. Under lasing conditions, however, the fraction of absorbed pump increases due to increased population of the ground-state manifold, brought by the stimulated emission, as expected in a quasi-three-level system. Under these conditions, the maximum pump absorption levels were 94% (18.1 W) and 55% (10.4 W) in the b-cut and ad-cut crystals, respectively. Importantly, the lasing condition also leads to an increased thermal loading due to larger quantum defect associated with the laser photons as compared to the average photons generated in spontaneous emission.

The dependence of the laser output on the absorbed pump power is shown in Fig. 8.2. The output characteristics for both crystals were very similar, at least up to 10 W of absorbed power, which was the maximum power for the ad-cut crystal. The maximum output powers obtained with the b-cut and the ad-cut crystals were 9 W and 4 W, respectively. The laser emission was linearly polarised for both crystals with the polarisation parallel to the N_m and

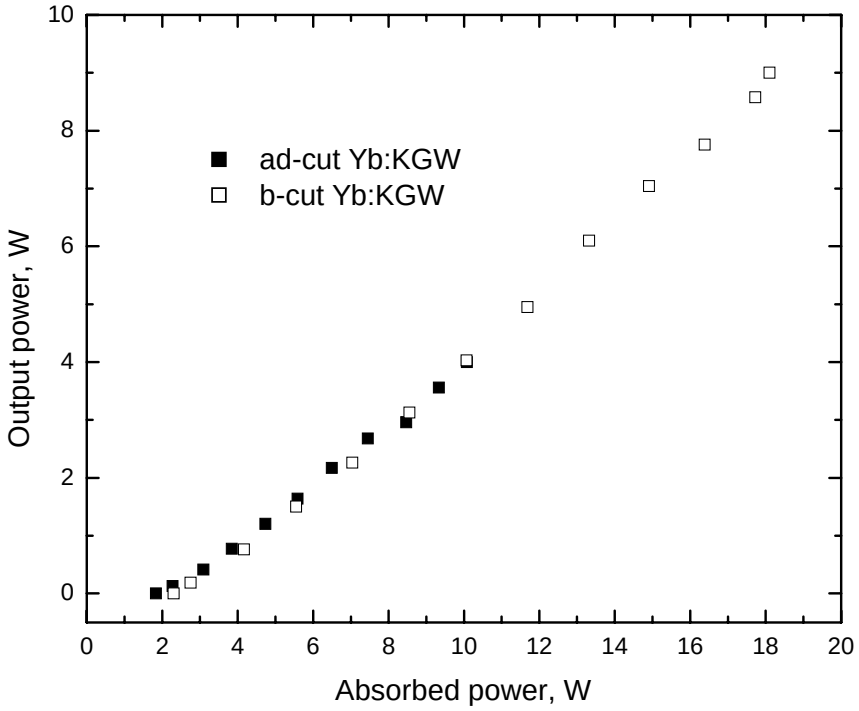

Fig. 8.2. Output power vs. absorbed power for the ad-cut (*solid squares*) and the b-cut (*open squares*) crystals.

N_p axes for the b-cut and the ad-cut crystals, respectively. In order to obtain higher output powers, higher Yb^{3+} concentrations should be used in order to compensate for the lower absorption cross section in the ad-cut geometry.

Due to the quasi-three-level nature of the Yb^{3+} system, the laser wavelength depends on the gain (losses). With the 95% output coupler, the free-running laser wavelength for the b-cut crystal was 1041 nm and for the ad-cut crystal it was 1043 nm. By inserting a 50 μm thick sapphire etalon into the cavity, the wavelength could be tuned. For the b-cut crystal, the laser was tuned this way between 1023 nm and 1040 nm, while the laser with ad-cut crystal was operated between 1038 nm and 1044 nm. The laser wavelength is substantially longer than the average fluorescence wavelength of 993 nm in Yb:KGW, which results in a substantial increase in the thermal loading when the laser cavity is aligned. Also, an additional thermal load is generated by the increased pump absorption under lasing conditions. A rough estimate of this thermal-load increase can be obtained from the ratio

$$\frac{P_{\mathrm{abs},L}}{P_{\mathrm{abs},NL}} \times \frac{1-\lambda_P/\lambda_L}{1-\lambda_P/\lambda_F}, \tag{8.1}$$

where $P_{\mathrm{abs},L}$ and $P_{\mathrm{abs},NL}$ are the absorbed pump powers under lasing and nonlasing conditions, while λ_L, λ_P and λ_F are the central wavelengths of the laser, the pump and the fluorescence, respectively. For the b-cut crystal, the thermal load increases 5 times while for the ad-cut crystal, it becomes 5.6 times larger under lasing conditions. This estimate does not take into account possible changes in the fraction of the nonradiative decay processes or the spectral distribution of the fluorescence, so we can only view the numbers as upper-limit estimates for the thermal-load increase. In any case, the effect was very pronounced in the thermal lens measurements. Consequently, all the thermal lens and beam distortion measurements have been performed in a carefully aligned laser cavity.

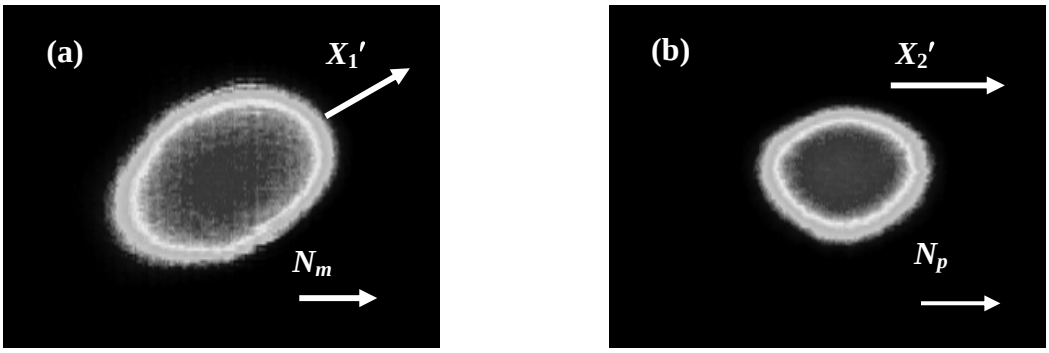

Fig. 8.3. The far-field profile of the beam at 10 W of absorbed power for (a) b-cut crystal and (b) ad-cut crystal. X_1' and X_2' are the thermal expansion axes, N_m and N_p are the crystallooptic axes, respectively.

The thermal lens was measured directly by use of a probe beam at 532 nm with the same polarisation as the laser emission. The probe beam was generated by a frequency-doubled Nd:YVO_4 ring laser generating 30 mW in a TEM_{00} intensity-stabilised mode. The probe beam was introduced collinearly to the pump beam by a dichroic mirror before the laser cavity. The $1/e^2$ beam diameter of the probe beam inside the crystal was 150 µm. This beam size was chosen in order to overlap the pump size. A lens pair was used to image the near and far fields of the probe beam onto a CCD camera to determine the thermal-lens parameters.

The far-field profiles of the laser beams for the b-cut and the ad-cut crystals at 10 W of absorbed pump power are shown in Figs. 8.3 (a) and (b), respectively. Also in the figures are indicated the directions of the crystallooptic axes N_m and N_p, parallel to the laser polarisation for each crystal. There is a clear astigmatism in both beam profiles, especially pronounced for the laser with the b-cut crystal. With this crystal, the long axis of the beam cross-section ellipse, corresponding to the direction of the stronger thermal lens, is rotated an angle of about 32° from the crystallooptic axis N_m. This direction approximately corresponds to the X_1' axis of the thermal expansion tensor, as shown in Fig. 8.3 (a) [47,60]. At higher absorbed powers in the b-cut crystal, the astigmatism further increases without changing the orientation of the ellipse. The weak astigmatism in the laser beam with the ad-cut crystal can be explained by the geometry of the pump beam. The elliptical pump-beam focus is wider and has a top-hat intensity distribution in the direction perpendicular to the direction of polarisation, which is perpendicular to the N_m and N_p directions in Figs. 8.3 (a) and (b), respectively. In this direction, we should expect lower thermal lensing, as compared to the perpendicular direction where the pump-beam waist is smaller and has a Gaussian intensity distribution. The direction of the thermal-expansion axis X_2' in the ad-crystal coincides with the short axis of the elliptical pump beam, or in other words, the axes of the output-beam cross-section ellipse correspond to those of the pump. Thus, we attribute the astigmatism of the laser output beam with the ad-cut crystal to the presence of inhomogeneous heating and elliptical pump focus.

The thermal lens as a function of the pump power was measured using the circular TEM_{00} probe beam at 532 nm described above. The measurements revealed that both crystals gave astigmatic thermal lenses, as expected. In the strong direction, the radius of the beam was reduced, while in the weak direction it was not affected enough for a reliable measurement. In the ad-cut crystal, the strong direction followed N_p, which is parallel to the thermal-expansion direction X_2', as is evident from the output-beam cross section in Fig. 8.3 (b). Also, it was confirmed that in the b-cut crystal, the strong thermal-lens direction was parallel to the thermal-expansion direction X_1'. The results of the thermal lens measurements are summarised in Fig. 8.4. It is evident that the thermal-lens power of the ad-cut crystal is approximately two times smaller as compared to the b-cut crystal for the same

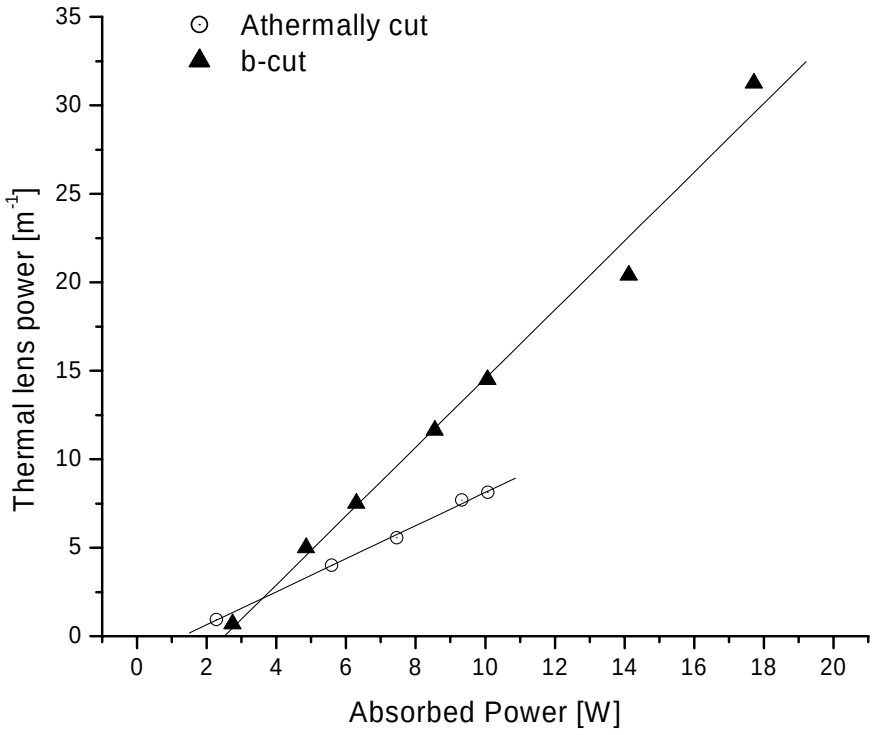

Fig. 8.4. Dependence of the thermal lens power on the absorbed pump power in ad-cut (*open circles*) and b-cut (*solid triangles*) Yb:KGW.

absorbed pump powers. From the thermal-lens measurements and from the far-field laser-intensity distribution, we can conclude that, at least in the case of the b-cut crystal, thermal deformation of the crystal due to thermal expansion should be the dominant effect in determining the geometry of the thermal lens. This is understandable, because in this configuration the positive thermal expansion coefficient is larger that the negative dn / dT [60].

The different strength and astigmatism of the thermal lenses in the b-cut and ad-cut Yb:KGW have a profound effect on the laser beam quality. By using near-field and far-field images, we measured the dependence of M^2 along the thermal lens axes as a function of the absorbed pump power. The results for both crystals are shown in Fig. 8.5. Two observations can be made from this measurement: first, the laser with the ad-cut Yb:KGW always exhibited better beam quality for the same absorbed pump powers; second, the beam for this crystal was to a large degree stigmatic, that is the M^2 values along orthogonal directions were very similar. This is in contrast to the b-cut crystal, where higher-order modes were preferentially generated along the strong thermal-lens axis (axis X_1').

The tests show that the investigated ad-cut direction can be a very useful alternative in applications where the thermal lens needs to be reduced. It would also be interesting to investigate an athermal direction in Yb:KYW, where higher Yb^{3+} doping concentrations can be more readily obtained or in Yb:KLuW, which is characterised by a smaller anisotropy of the thermal properties [61].

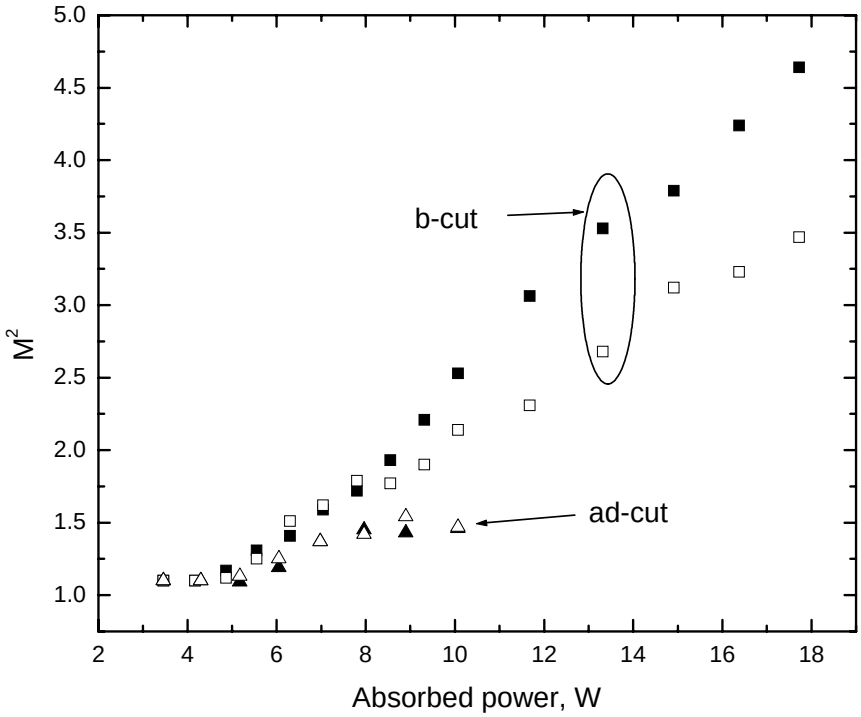

Fig. 8.5. Dependence of the beam quality factor M^2 on the absorbed pump power for the b-cut (*squares*) and ad-cut (*triangles*) Yb:KGW measured along two orthogonal thermal lens axes.

9 Er-Yb-doped double tungstates

9.1 Er-Yb eye-safe lasers

Erbium-doped solid-state lasers are widely used for generation of light in the eye-safe region around 1.5 μm. There are many applications including range finding, remote sensing, optical fibre communication, medicine and meteorology. A survey of eye-safe lasers and their applications is found in Ref. [63]. As erbium-doped crystals have rather poor absorption at pump-diode wavelengths around 980 nm, the laser efficiency is reduced, and for this reason, sensitiser ions such as ytterbium are added to the material which increase the pump absorption and, via excitation transfer to the erbium ions, improve the laser performance. So far, the Er-Yb-doped phosphate glass [64–66] has been the most efficient laser host in the 1.53 μm wavelength region with the optimum doping concentrations rather well established. Other materials, which have shown efficient laser operation recently are $GdCa_4O(BO_3)_3$ (GdCOB) [67,68] and $YCa_4O(BO_3)_3$ (YCOB) [69]. However, both the phosphate glass, the GdCOB and the YCOB are far from being perfect laser materials. The main limitations are low thermal conductivity, low threshold for thermal stress-induced fracture as well as relatively low absorption and stimulated-emission cross sections for the Yb^{3+} and the Er^{3+} ions, respectively. For comparison, Er-Yb-doped double-tungstate crystals such as $KGd(WO_4)_2$ (KGW) [70] and $KY(WO_4)_2$ (KYW) [71,72] offer definite advantages with respect to all these parameters, in particular considering that the Yb^{3+} absorption cross section is an order of magnitude larger and that the Er^{3+} emission cross section is about twice as large in double tungstates than in phosphate glass or GdCOB. On the other hand, the spectroscopic properties and the dynamics in the Er^{3+}, Yb^{3+} system are substantially different in double-tungstate crystals. This means that the optimum doping concentrations and their proportions, which are critical for efficient laser action, are substantially different in the double tungstate crystals from those in glass or GdCOB.

Laser action around 1.5 μm has been demonstrated before in Er:Yb:KYW [50], but the laser slope efficiency was extremely low, only 1% with respect to absorbed power, which compares unfavourably with phosphate glass [64,65] or GdCOB [67,68]. In Paper VIII described in this chapter, the objective is to find the optimum doping concentrations in double tungstates for eye-safe lasers. This objective is achieved by first investigating relevant spectroscopic and dynamic properties of the Er^{3+}, Yb^{3+} system in double-tungstate hosts. This involves an experimental study of the excitation dynamics in the crystals with a variety of doping concentrations, which will allow us to deduce relevant dynamic parameters for the theoretical rate-equation model. The modelling then allows for mapping of the expected fluorescence and gain versus doping concentrations and will be used to predict the optimum concentrations.

9.2 Energy levels in Er-Yb double tungstates

In Fig. 9.1, the energy-level diagram for Er:Yb:KGW and Er:Yb:KYW is shown with relevant processes, including the pump at 0.94 μm (in our case), Yb fluorescence around 1 μm, Er fluorescence around 1.5 μm, forth transfer (FT) and back transfer (BT). As in Nd-doped materials (Sect. 2.10), there are also upconversion processes present in the Er-Yb systems. Two possible processes called cumulative (UC_1) and cooperative (UC_2) upconversion result in strong green fluorescence at 0.55 μm. The indexed numbers of Yb (i) and Er (j) are used according to the labelled energy levels in the figure.

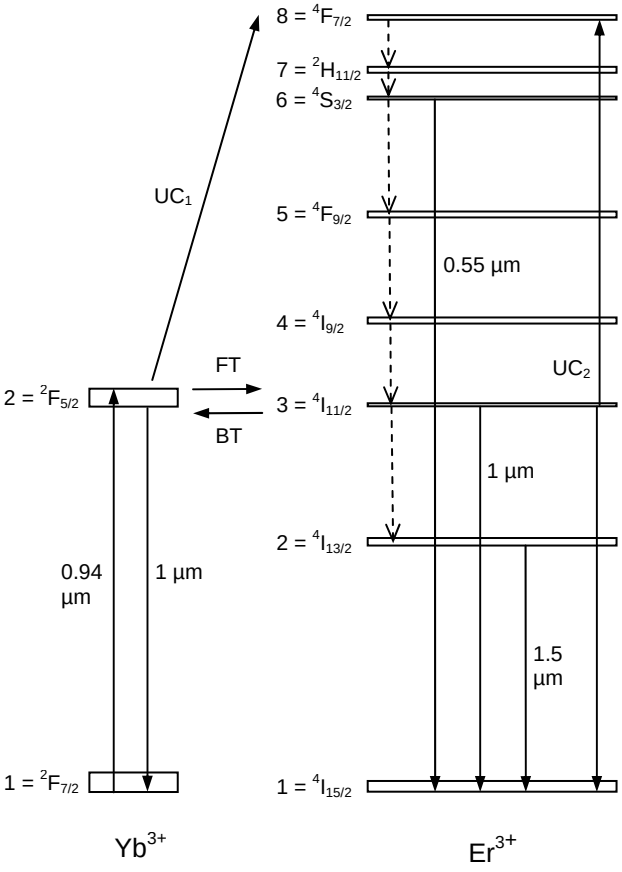

Fig. 9.1. Energy-level diagram of Er-Yb double-tungstate system.

During the pumping stage in Yb, corresponding to the $^2F_{7/2} \rightarrow {}^2F_{5/2}$ absorption at 900–1040 nm, the population inversion build-up in Er is mainly dependent on the energy transfer Yb ($^2F_{5/2}$) + Er ($^4I_{15/2}$) $\rightarrow$ Yb ($^2F_{7/2}$) + Er ($^4I_{11/2}$), followed by radiative and nonradiative relaxation to the upper laser level $^4I_{13/2}$. A short nonradiative relaxation lifetime of the $^4I_{11/2}$ level is important, as the nonradiative decay depopulates this level and makes the energy back transfer Yb ($^2F_{7/2}$) + Er ($^4I_{11/2}$) $\rightarrow$ Yb ($^2F_{5/2}$) + Er ($^4I_{15/2}$) less likely. The back-transfer process, on the other hand, wastes pump energy due to the predominantly radiative decay of the Yb ($^2F_{5/2}$) level. At the same time, fast depopulation of the $^4I_{11/2}$ level is essential for reducing both the cumulative upconversion involving one Yb ion and one Er ion: Yb ($^2F_{5/2}$) + Er ($^4I_{11/2}$) $\rightarrow$ Yb ($^2F_{7/2}$) + Er ($^4F_{7/2}$), and the cooperative upconversion involving two Er ions: Er ($^4I_{11/2}$) + Er ($^4I_{11/2}$) $\rightarrow$ Er ($^4F_{7/2}$) + Er ($^4I_{15/2}$). These processes divert the excitation from the lasing level, thus reducing pumping efficiency. Upconverted Er^{3+} ions in the $^4F_{7/2}$ level experience a fast nonradiative decay to the $^4S_{3/2}$ manifold. A large part of the upconversion $^4S_{3/2}$ level population relaxes nonradiatively, generating excess heat in the laser crystal. The remainder decays as $^4S_{3/2} \rightarrow {}^4I_{15/2}$ green emission at 550 nm.

Efficient lasing in the eye-safe region employing the Er ($^4I_{13/2} \rightarrow {}^4I_{15/2}$) transition around 1530 nm requires efficient resonant energy transfer from level $^2F_{5/2}$ of the Yb^{3+} ion subsystem to level $^4I_{11/2}$ of the Er^{3+} ion subsystem, followed by a fast nonradiative relaxation to the upper laser level $^4I_{13/2}$. The nonradiative relaxation of the Er ($^4I_{11/2}$) level is determined by the phonon spectrum of the host material, especially the high-energy phonon modes which give the fastest nonradiative relaxation in the multiphonon process. For instance, the relaxation in phosphate glass is determined by the high-density-of-states phonon mode at

Host crystal	Er conc. (mol %)	$^4S_{3/2}$ lifetime (μs)	$^4I_{11/2}$ lifetime (μs)
KGW	1%	26	148
	3%	23	153
	5%	19	151
KYW	5%	14	123
glass	0.9%		2.5 [65]
GdCOB	2.5%		0.25 [67]

Table 9.1. Lifetimes of the $^4S_{3/2}$ and $^4I_{11/2}$ levels in singly Er-doped crystals.

1200 cm^{-1} [72]. In GdCOB the predominant phonon energies are around 943 cm^{-1} and 1300 cm^{-1} [73,74], while the phonons with frequencies of 901 cm^{-1} and 528 cm^{-1} in KGW [75], 530 cm^{-1} in KYW, and 908 cm^{-1} and 534 cm^{-1} in KYbW [76] would contribute the most. Consequently, phosphate glass and GdCOB should have the fastest nonradiative relaxation, while the relaxation in KGW should be rather slow, leading to the requirement of careful optimisation of the doping concentrations in the codoped crystals.

9.3 Fluorescence dynamics

In order to measure the decay rates of the Er ($^4S_{3/2}$) and the Er ($^4I_{11/2}$) levels, predominantly due to multiphonon relaxations, we used singly Er-doped crystals, excited by a frequency-doubled pulsed Nd:YAG laser at 532 nm. A beam with 3 ns pulse length and 20 Hz repetition frequency was focused into the Er:KGW and Er:KYW crystals in a 200 μm diameter spot. The fluorescence was collected perpendicularly from the excitation direction, passed through an imaging system and appropriate band-pass and pump-rejection filters, and was detected by a Si p-i-n diode. The temporal signal was digitised with 5 Gs/s sampling rate, by a 1-GHz analogue bandwidth oscilloscope. We measured the dynamics of the 0.55 μm and 1 μm fluorescence for KGW crystals with Er doping concentrations of 1%, 3% and 5%, respectively, and for a 5% Er-doped KYW crystal. Due to noise in the fluorescence dynamics measurements, an error margin of less than 5% is estimated for the lifetimes measured in our system. The measured lifetimes of the $^4S_{3/2}$ and $^4I_{11/2}$ levels are shown in Table 9.1. It is evident that the $^4I_{11/2}$ lifetimes in KGW (151 μs on average) and KYW (123 μs) are much longer than those in glass (2.5 μs) [65] and GdCOB (0.25 μs) [67]. The long lifetime of KGW and KYW causes significant back transfer and green upconversion in codoped Er-Yb crystals, in contrast to glass and GdCOB, which experience Yb-Er energy transfer followed by rapid relaxation from $^4I_{11/2}$ to $^4I_{13/2}$.

To measure the Er^{3+} and Yb^{3+} fluorescence dynamics in the codoped samples, which can be used to determine the rates of the energy exchange and relaxation processes, we used an experimental setup employing a nanosecond optical parametric oscillator that generated 3 ns pulses and was tunable between 800 nm and 1000 nm. The beam was focused in a 200 μm diameter spot and the fluorescence was again collected perpendicularly from the excitation direction and was detected by Si and InGaAs p-i-n diodes. The excitation wavelength was tuned to 935 nm where only the Yb^{3+} subsystem was excited, thus giving direct access to the resonant energy transfer dynamics. With this detection system, we could observe the fluorescence dynamics of the Yb ($^2F_{5/2}$), Er ($^4I_{13/2}$) and Er ($^4S_{3/2}$) levels. The maximum density of the excited Yb^{3+} ions constituted only about 5% of the Yb^{3+} concentration in the KGW and the KYW crystals and at these excitation levels we can largely neglect absorption saturation and stimulated emission. We could also measure the upconversion luminescence's dependence on pump power in Er 5%:Yb 5%:KGW and saw an approximate quadratic behaviour, indicating that the upconversion rate is not so large at these

Host crystal	Er conc. (mol %)	Yb conc. (mol %)	Yb ($^2F_{5/2}$) lifetime (μs)	Er ($^4S_{3/2}$) rise time (μs)	Er ($^4S_{3/2}$) lifetime (μs)	Er ($^4I_{13/2}$) rise time (μs)	Er ($^4I_{13/2}$) lifetime (ms)
KGW	–	5%	438	–	–	–	–
	0.5%	5%	273		126	252	3.3
	0.5%	2.5%	229		101	24	3.3
	2.5%	7.5%	222		95	222	3.8
	1.4%	2.5%	212		92	207	3.2
	5%	5%	170	4	71	173	3.6
KYW	–	5%	440	–	–	–	–
	0.5%	5%	341	8.5	111		
	0.5%	2.5%	262	7.5	95		
	1.5%	2.5%	177	6	79	170	3.4
KYbW	1%		(~ 490)		(~ 115)		3.2
	3%		(~ 410)		(~ 105)		3.8
glass	–	15.5%	1200 [65]	–	–	–	–
	2.75%	22%	12	–	–		8.5 [65]
GdCOB	–	10%	2300	–	–	–	–
	2.5%	28%	34	–	–	35	1.16

Table 9.2. Lifetimes and rise times of the Yb ($^2F_{5/2}$), Er ($^4S_{3/2}$) and Er ($^4I_{13/2}$) levels in Er-Yb-doped crystals.

low power levels [77,78]. At high power, a dependence of the upconversion to a power less than two would be expected. The results of the measured rise times and lifetimes are shown in Table 9.2 and are discussed below.

First, we measured the dynamics of Yb^{3+} in Yb:KGW and Er:Yb:KGW. The presence of radiation trapping [79,80] for this quasi-three-level transition around 1 μm can affect the measured lifetimes. Radiation trapping is caused by reabsorption of the initial emission by ions in the ground state, which is followed by reemission and results in lengthening of the measured lifetime. Circulating radiation caused by total internal reflection at the end surfaces of the crystal further increases the probability of reabsorption. Due to radiation trapping, the lifetime-measurement results depend on the acceptance angle of the detecting system [81] and indeed, the measured relaxation time with a 0.8 mm^2 area detector was 6% to 21% smaller than with a 13 mm^2 detector, with the smallest difference observed for samples with shorter lifetimes. Consequently, we used the small-area detector for the dynamics measurements. In Fig. 9.2, the fluorescence dynamics of the Yb ($^2F_{5/2}$) level in Yb:KGW and various Er:Yb:KGW crystals is shown in a semilogarithmic scale. The measured lifetimes are showing a decreasing trend from 438 μs to 170 μs for an increasing Er-to-Yb-concentration ratio in the samples. The relaxation of the Yb^{3+} fluorescence in all investigated crystals is determined by the resonant energy transfer, back transfer and the relaxation rate of the Er ($^4I_{11/2}$) level. In fact, the ratio of the Yb ($^2F_{5/2}$) relaxation time in singly Yb^{3+}-doped hosts to that measured in the codoped hosts can serve as an indication for the pumping efficiency of the eye-safe laser transition. In the phosphate glass, we found this ratio to be 100, in GdCOB it decreased to 68, while in the measured double tungstates, this ratio was only 2.6 (obtained in the KGW sample with almost equal Er^{3+} and Yb^{3+} concentrations). A very similar trend have been obtained in several different Er:Yb:KYW crystals. The dynamics of the Yb fluorescence in stoichiometric double tungstates $KYb_{1-x}Er_x(WO_4)_2$ (Er:KYbW) was also measured. Due to the high Yb^{3+} excitation and the strong upconversion in these samples, the decay was non-exponential. Still, a single-exponential fit can be done in the tail after about 0.5 ms. The resulting "tail-lifetimes" are around 490 μs and 410 μs for Er 1%:KYbW and Er 3%:KYbW, respectively. These lifetimes are as expected close to the lifetime of 440 μs in singly-doped Yb 5%:KYW, due to the small Er-to-Yb-concentration ratio in Er:KYbW.

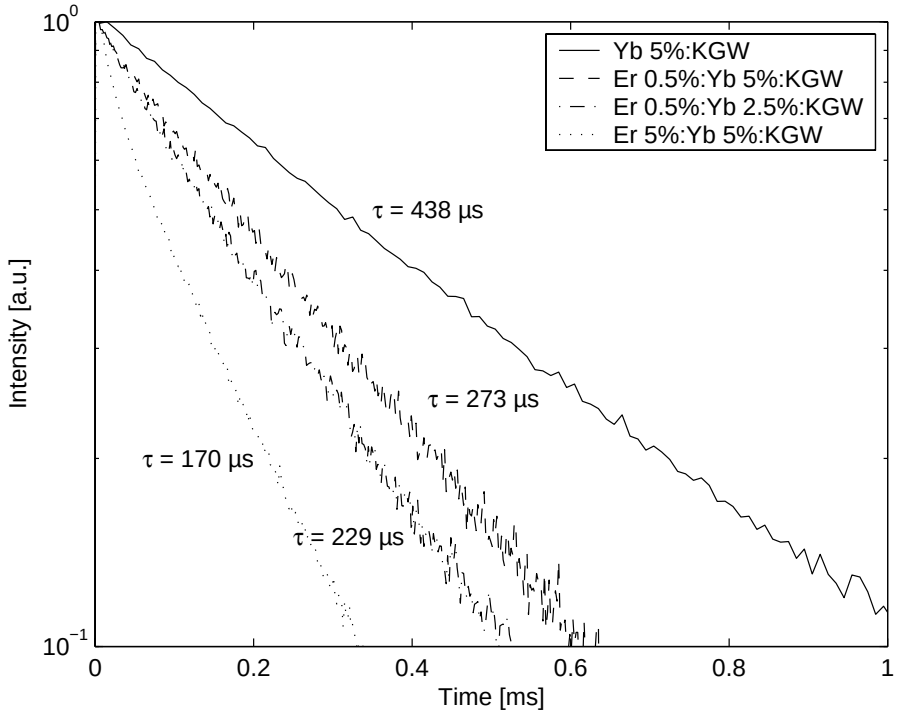

Fig. 9.2. Fluorescence dynamics from the Yb ($^2F_{5/2}$) level around 1 µm in Yb:KGW and Er:Yb:KGW.

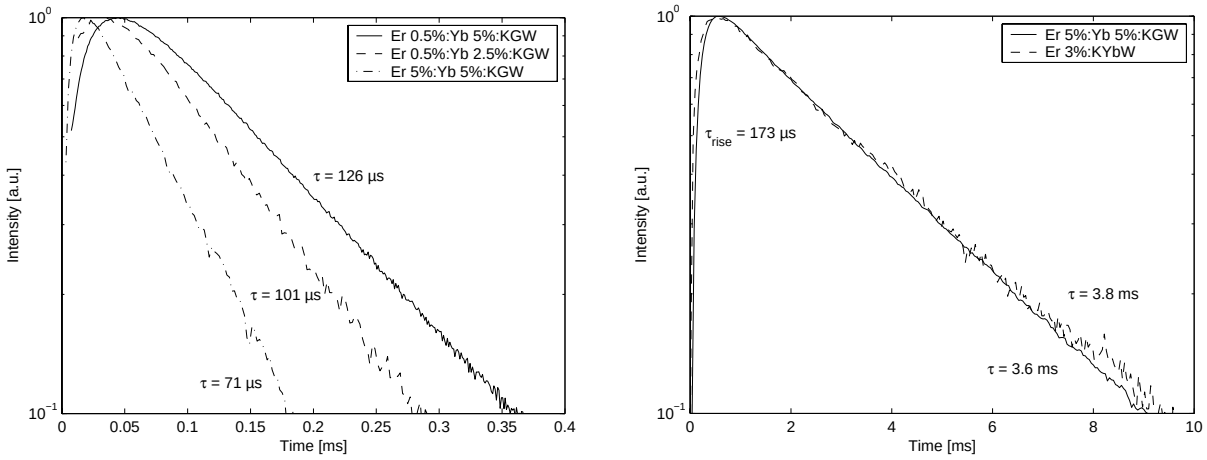

(a) **(b)**

Fig. 9.3. (a) Dynamics of the green emission from the Er ($^4S_{3/2}$) level at 0.55 µm in Er:Yb:KGW. (b) Dynamics from the Er ($^4I_{13/2}$) level around 1.5 µm in Er 5%:Yb 5%:KGW (*solid line*) and in Er 3%:KYbW (*dashed line*).

The green upconversion fluorescence originating from the Er ($^4S_{3/2}$) level is very strong in the codoped samples. There are two reasons for strong upconversion in double tungstates: a relatively long lifetime of the Er ($^4I_{11/2}$) level and a large efficiency of the dipole-dipole interaction between ions, resulting in large coupling constants in the transfer processes. Fast redistribution of the excitation between Yb^{3+} and Er^{3+} means that the relaxation dynamics of the upconversion to a large extent follows that of the long-lived Yb^{3+} subsystem. The lifetime increases from around 20 µs in singly-doped Er:KGW to 126 µs in Er 0.5%:Yb 5%:KGW, as can be seen in Fig. 9.3 (a). For some samples, we could also measure the short rise times of around 4 to 8 µs.

Finally, all samples showed substantial fluorescence in the 1.5 μm eye-safe spectral region. The fluorescence lifetime measurements (two examples are shown in Fig. 9.3 b) showed that the relaxation-time constants are mostly unaffected by the doping concentrations in the samples which were available to us. The fluorescence lifetime of about 3.2–3.8 ms in Er:Yb:KREW is about three times longer than in Er:Yb:GdCOB (1.16 ms) and more than two times shorter than in Er:Yb:phosphate glass (8.5 ms). The fluorescence rise time in the 1.53 μm spectral region, originating from the Er ($^4I_{13/2}$) → Er ($^4I_{15/2}$) transition, is important as it reflects the decay time of the Er ($^4I_{11/2}$) level. The measured rise times are about the same as the Yb ($^2F_{5/2}$) lifetimes, and hence the decays of the Yb ($^2F_{5/2}$) and Er ($^4I_{11/2}$) levels are in balance.

9.4 Rate equations analysis

In order to model the population levels in Yb and Er and to explain the observed dynamics in the previous section, a set of rate equations shown in Eqs. (9.1)–(9.6) below is used [82–84]. The model includes the energy transfer from Yb ($^2F_{5/2}$) to Er ($^4I_{11/2}$), as well as back transfer and cumulative and cooperative upconversion losses to Er ($^4F_{7/2}$). As the $^4F_{7/2}$, $^2H_{11/2}$, $^4F_{9/2}$ and $^4I_{9/2}$ levels in Er, shown in Fig. 9.1, relax rapidly to the next lower-lying level by multiphonon decay, these states have been excluded in the rate equations.

$$\frac{dN_{Yb,2}}{dt} = R_P - \frac{N_{Yb,2}}{\tau_{Yb}} - k_{FT} N_{Er,1} N_{Yb,2} + k_{BT} N_{Yb,1} N_{Er,3} - k_C N_{Er,3} N_{Yb,2}, \tag{9.1}$$

$$\frac{dN_{Er,6}}{dt} = -W_{NR,6} N_{Er,6} - \frac{N_{Er,6}}{\tau_{Er,6}} + k_C N_{Yb,2} N_{Er,3} + C_{up} N_{Er,3}^2, \tag{9.2}$$

$$\begin{aligned} \frac{dN_{Er,3}}{dt} = &-W_{NR,3} N_{Er,3} - \frac{N_{Er,3}}{\tau_{Er,3}} - k_{BT} N_{Yb,1} N_{Er,3} + k_{FT} N_{Er,1} N_{Yb,2} \\ &- k_C N_{Yb,2} N_{Er,3} - 2C_{up} N_{Er,3}^2 + W_{NR,6} N_{Er,6} + \beta_{63} \frac{N_{Er,6}}{\tau_{Er,6}} \end{aligned}, \tag{9.3}$$

$$\frac{dN_{Er,2}}{dt} = -\frac{N_{Er,2}}{\tau_{Er,2}} + W_{NR,3} N_{Er,3} + \beta_{32} \frac{N_{Er,3}}{\tau_{Er,3}} + \beta_{62} \frac{N_{Er,6}}{\tau_{Er,6}}, \tag{9.4}$$

$$N_{Yb} = N_{Yb,1} + N_{Yb,2}, \tag{9.5}$$

$$N_{Er} = N_{Er,1} + N_{Er,2} + N_{Er,3} + N_{Er,6}. \tag{9.6}$$

The population densities $N_{Yb,1–2}$ and $N_{Er,1–6}$ correspond to the level numbers shown in Fig. 9.1. R_P is the pump rate density from Yb (1) to Yb (2); τ_{Yb}, $\tau_{Er,2}$, $\tau_{Er,3}$ and $\tau_{Er,6}$ are the radiative lifetimes from the Yb (2), Er (2), Er (3) and Er (6) levels, respectively; $W_{NR,3}$ and $W_{NR,6}$ are the nonradiative decay rates from the Er (3) and the Er (6) levels, respectively; k_{FT} is the (forth) energy-transfer coefficient, k_{BT} is the back-transfer coefficient, k_C is the cumulative-

upconversion coefficient, C_{up} is the cooperative-upconversion coefficient, β_{ij} are the branching ratios from the Er (i) to the Er (j) levels, and N_{Yb} and N_{Er} are the respective total Yb^{3+} and Er^{3+} ion concentrations in the material.

To study the influence of the transfer and back transfer on the relaxation times of the Yb (2) and Er (3) levels under short-pulse pumping, a system of simplified rate equations generating single-exponential decays are derived from Eqs. (9.1) and (9.3), where low excitation is assumed and upconversion is neglected. At low excitation, the ground-state populations in Er and Yb are left almost unchanged, so that a transfer rate $W_{FT} = k_{FT} N_{Er}$ and a back-transfer rate $W_{BT} = k_{BT} N_{Yb}$ can be used. Furthermore, the radiative decay from Er (6) and Er (3) is ignored as these levels relax predominantly by nonradiative processes. With these assumptions, $N_{Yb,2}$ and $N_{Er,3}$ can be solved from an independent linear system:

$$\frac{dN_{Yb,2}}{dt} = -(W_{Yb} + W_{FT})N_{Yb,2} + W_{BT} N_{Er,3}, \tag{9.7}$$

$$\frac{dN_{Er,3}}{dt} = W_{FT} N_{Yb,2} - (W_{NR,3} + W_{BT})N_{Er,3}, \tag{9.8}$$

where $W_{Yb} = 1/\tau_{Yb}$. As the pump pulse is on a nanosecond scale, compared to the other dynamical processes that are on at least a microsecond scale, the initial excitation $N_{Yb,2}(0)$ is taken as constant. No initial excitation of Er^{3+} is assumed ($N_{Er,3}(0) = 0$). The solution to this linear system (9.7) and (9.8) is then written as

$$N_{Yb,2}(t) = C_{11} e^{-W_{eff,1} t} + C_{12} e^{-W_{eff,2} t}, \tag{9.9}$$

$$N_{Er,3}(t) = C_{21} e^{-W_{eff,1} t} + C_{22} e^{-W_{eff,2} t}, \tag{9.10}$$

where the effective rates determining the population evolutions are

$$W_{eff,1} = \frac{W_{FT} + W_{BT} + W_{Yb} + W_{NR,3}}{2} + \frac{1}{2}\sqrt{(W_{FT} - W_{BT} + W_{Yb} - W_{NR,3})^2 + 4W_{FT}W_{BT}}, \tag{9.11}$$

$$W_{eff,2} = \frac{W_{FT} + W_{BT} + W_{Yb} + W_{NR,3}}{2} - \frac{1}{2}\sqrt{(W_{FT} - W_{BT} + W_{Yb} - W_{NR,3})^2 + 4W_{FT}W_{BT}}, \tag{9.12}$$

and the constants C_{ij} are given by

$$C_{11} = N_{Yb,2}(0)\frac{W_{FT} + W_{Yb} - W_{eff,2}}{W_{eff,1} - W_{eff,2}}, \tag{9.13}$$

$$C_{12} = N_{Yb,2}(0) - C_{11}, \tag{9.14}$$

$$C_{21} = C_{11}\frac{W_{FT} + W_{Yb} - W_{eff,1}}{W_{BT}}, \tag{9.15}$$

$$C_{22} = -C_{21}. \tag{9.16}$$

$W_{eff,1}$ can be seen as both the effective decay rate of Yb (2) and the effective rise rate of Er (3) at the initial time. At later times, the slower effective decay rate $W_{eff,2}$ is dominant, which leads to an equal single-exponential decay from Yb (2) and Er (3), according to this model. For our situation with W_{Yb} and $W_{NR,3}$ of the same order, a Taylor expansion around $W_{NR,3} = W_{Yb}$ gives the following approximation of $W_{eff,2}$ from Eq. (9.12):

$$W_{eff,2} \approx W_{Yb} + \frac{W_{NR,3} - W_{Yb}}{1 + (W_{FT}/W_{BT})^{-1}}. \tag{9.17}$$

From Eq. (9.17) we can see that the effective lifetime $1/W_{eff,2}$ is dependent on the ratio W_{FT}/W_{BT}, and thus on the [Er] / [Yb] concentration ratio. It is further seen that $W_{eff,2} \to W_{NR,3}$ when $W_{FT}/W_{BT} \to \infty$, and therefore the nonradiative lifetime of the Er ($^4I_{11/2}$) level is limiting the effective lifetime and hence the transfer efficiency that is possible to achieve by optimisation of the doping concentrations.

In Fig. 9.4 (a), the Yb ($^2F_{5/2}$) fluorescence relaxation time is displayed in circles as a function of the [Er] / [Yb] concentration ratio in different KGW crystals. It shows an initial fast decrease as Er^{3+} is added to the sample, but then it tends to saturation towards the nonradiative lifetime of 151 µs in Er:KGW as the Yb^{3+} and Er^{3+} concentrations become approximately equal as predicted by Eq. (9.17). Equation (9.12) can be fitted by a least-squares approximation to the measured effective lifetimes with a constant ratio k_{FT}/k_{BT}. The result is shown as a solid line for $k_{FT}/k_{BT} = 4.2$. This result is affected by the presence of radiation trapping in the lifetime measurements, but still Eq. (9.12), and Eq. (9.17) to a very good approximation, explain the observed behaviour in the lifetimes' dependence of the doping concentrations. In Fig. 9.4 (a), the solid line also corresponds well to the rise time of the Er ($^4I_{13/2}$) level (triangles), which is populated by electrons relaxing from the Er ($^4I_{11/2}$) level. The green upconversion decay from Er ($^4S_{3/2}$) is expected to follow $\exp(-2W_{eff,2}t)$, as this level is populated by the terms $k_C N_{Yb,2} N_{Er,3}$ and $C_{up} N_{Er,3}^2$ in Eq. (9.2), where both $N_{Yb,2}$ and $N_{Er,3}$ decay as $\exp(-W_{eff,2}t)$. In Fig. 9.4 (a), the green-upconversion relaxation times (squares) are actually 8% to 16% lower than the predicted half values of the Yb lifetimes. This can be explained by the fact that ions excited by radiation trapping outside the pumped volume may not contribute to the upconversion, as the average distance between excited ions is large at very low excitation, whereas for the energy transfer, excited Yb^{3+} ions and Er^{3+} ions in the ground state are involved, making this process more likely. The same calculations were done for Er:Yb:KYW, shown in Fig. 9.4 (b). The results are a little different as the Er ($^4I_{11/2}$) lifetime is shorter in KYW (123 µs) and the k_{FT}/k_{BT} ratio is here calculated to 2.3.

It is difficult to unambiguously distinguish which one of the two upconversion processes, the cumulative or the cooperative one is the most efficient in codoped samples. There was, however, a recent report on strong suppression of the upconversion fluorescence in an Er:Yb:KYW crystal with large [Er] / [Yb] concentration ratio (Er 18.8%, Yb 1.6%) [85]. For comparison, we investigated green upconversion fluorescence in KGW samples pumped

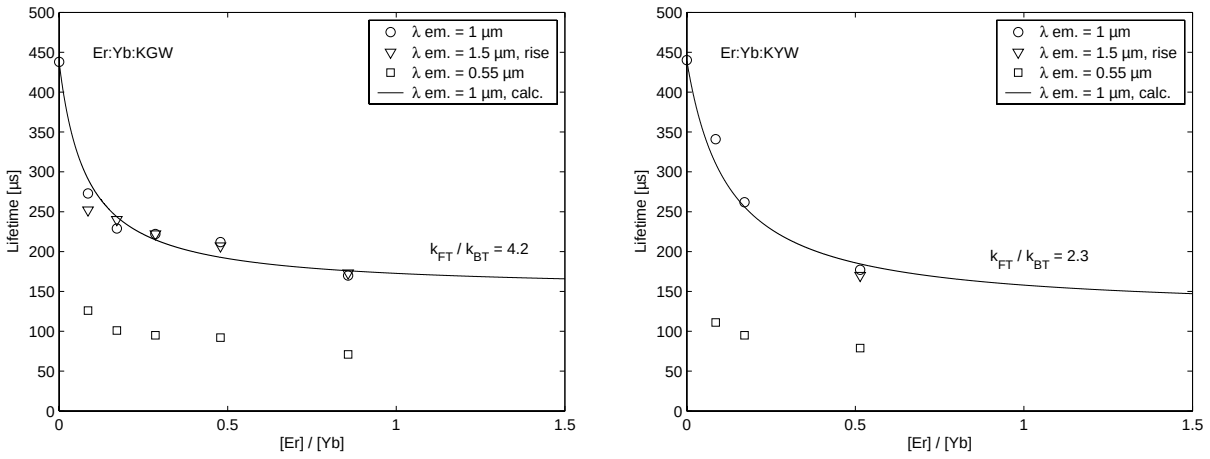

(a) **(b)**

Fig. 9.4. Measured lifetimes vs. doping-concentration ratio [Er] / [Yb]: (a) in Er:Yb:KGW, (b) in Er:Yb:KYW. *Circles:* Yb ($^2F_{5/2}$) level at 1 µm, *triangles:* rise time of Er ($^4I_{13/2}$) level at 1.5 µm, *squares:* Er ($^4S_{3/2}$) level at 0.55 µm, *solid line:* calculated lifetime of Yb ($^2F_{5/2}$) level: (a) with $k_{FT}/\,k_{BT} = 4.2$, (b) with $k_{FT}/\,k_{BT} = 2.3$.

by a CW laser diode at 975 nm. For the same absorbed power, the intensity was much larger (by visual inspection) for the codoped sample with the weakest green fluorescence (Er 0.5%:Yb 2.5%:KGW) than for any of the singly Er-doped crystals. Both the observation in Ref. 9 and our own investigation indicate that the cooperative upconversion constant C_{up} is much smaller than the cumulative upconversion constant k_C. In the following, the cooperative upconversion is therefore neglected.

Knowing the transfer coefficient k_{FT} is crucial for proper optimisation of the doping concentrations, especially in Er, Yb doped tungstates, where the lifetime of the intermediate Er ($^4I_{11/2}$) level is relatively long. A value of k_{FT} can be estimated from the measured rise time in the Er ($^4S_{3/2}$) fluorescence. For the sample with the longest rise time of 8.5 µs (Er 0.5%:Yb 5%:KYW), the rate equations (9.1)–(9.6) were solved numerically for different values of k_{FT}. Due to the similarity between the transfer and cumulative upconversion processes, k_C was assumed to be equal to k_{FT} and in this way a fit of the transfer coefficient to about $(5 \pm 2) \times 10^{-15}$ cm^{3}s^{-1} was achieved. It should be noted that this value is about one order of magnitude larger than the measured values in Er:Yb:phosphate glass (4.1×10^{-16} cm^{3}s^{-1}) and Er:Yb:GdCOB (2.9×10^{-16} cm^{3}s^{-1}). The transfer coefficients for glass and GdCOB were calculated from the transfer rate $W_{FT} = k_{FT} N_{Er}$, which for an Er-Yb-system with rapid Er ($^4I_{11/2}$) relaxation is given by

$$W_{FT} = \frac{1}{\tau_{eff}} - \frac{1}{\tau_{Yb}}, \tag{9.18}$$

where τ_{eff} is the measured Yb relaxation time.

As we are interested in finding the optimum doping concentrations for laser action in double tungstates, we have performed calculations of the gain for the Er ($^4I_{13/2} \rightarrow {}^4I_{15/2}$) transition around 1.5 µm in Er:Yb:KYW. For CW pumping, we take the pump-rate density as in Eq. (2.25), but we now include the population density in the upper Yb state:

$$R_P = W_P (N_{Yb,1} - N_{Yb,2}), \tag{9.19}$$

where the pumping-transition probability W_P is approximated by a homogeneous pump-intensity distribution over an area of πw_P^2 and given by Eq. (2.18) as

$$W_P = \frac{\sigma_P P_P}{h\nu_P \pi w_P^2}, \tag{9.20}$$

where σ_P, P_P, $h\nu_P$ and w_P are the absorption cross section, power, photon energy and beam radius of the pump, respectively. We can then solve the rate equations (9.1)–(9.6) at steady state, where the radiative decay from the levels Er (6) and Er (3) has been ignored. First, the population density of the Er (6) level is solved from Eq. (9.2) as

$$N_{Er,6} = \frac{k_C N_{Yb,2} + C_{up} N_{Er,3}}{W_{NR,6}} N_{Er,3}, \tag{9.21}$$

and is then inserted into Eq. (9.3), and together with $N_{Yb,1} = N_{Yb} - N_{Yb,2}$, the excited Yb population is solved:

$$N_{Yb,2} = \frac{W_{NR,3} + k_{BT} N_{Yb} + C_{up} N_{Er,3}}{k_{FT} N_{Er,1} + k_{BT} N_{Er3}} N_{Er,3}. \tag{9.22}$$

Equation (9.21) is now inserted into Eq. (9.1) and solved for the Er ground-state population:

$$N_{Er,1} = \frac{(2W_P + W_{Yb} + k_C N_{Er,3})(k_{BT} N_{Yb} + W_{NR,3} + C_{up} N_{Er,3})}{k_{FT}(W_P N_{Yb} - W_{NR,3} N_{Er,3} - C_{up} N_{Er,3}^2)} N_{Er,3} - \frac{k_{BT}}{k_{FT}} N_{Er,3}. \tag{9.23}$$

The Er (2) population density is solved from Eq. (9.2) as

$$N_{Er,2} = \frac{W_{NR,3}}{W_{Er,2}} N_{Er,3}. \tag{9.24}$$

The expressions (9.21)–(9.24) can then be inserted into Eq. (9.6) and solved for $N_{Er,3}$. If the cooperative upconversion is ignored ($C_{up} = 0$), the resulting expression is a cubic equation, which in principle can be solved analytically (with a lengthy expression), but instead has been solved numerically.

If we assume a homogenous pumping over a crystal of length l, the nonlasing *single-pass* gain at the emission peak (where the stimulated-emission and absorption cross sections are about the same) of the eye-safe transition is given by a similar expression as in Eq. (2.75), but now without a factor of two:

$$\sigma(N_{Er,2} - N_{Er,1})l. \tag{9.25}$$

Figure 9.5 shows the calculated single-pass gain versus Er concentration for an Er:Yb:KYW crystal of length 1 mm, pumped homogeneously with 0.25 W in a 100 µm diameter top-hat pump spot at 981 nm. A narrow-band pump source such as a Ti:sapphire laser polarised in the N_m principal optical direction is assumed. In this direction, $\sigma_P = 11.7 \times 10^{-20}$ cm^2 and the maximum stimulated-emission cross section is $\sigma = 2.7 \times 10^{-20}$ cm^2 at 1534 nm [86]. The calculated curves correspond to four different Yb concentrations: 1%, 2.5%, 5% and 20%,

respectively. As can be seen, the result is that the gain increases with higher Yb concentration, and that there is clearly an optimum Er concentration for each case of Yb doping.

To calculate the gain for Er:Yb:glass, we use similar rate equations [87–89] but due to the short lifetime of the Er ($^4I_{11/2}$) level, back transfer and upconversion involving this level can be neglected. Instead, the possible cumulative upconversion Yb ($^2F_{5/2}$) + Er ($^4I_{13/2}$) → Yb ($^2F_{7/2}$) + Er ($^4F_{9/2}$) and the cooperative upconversion Er ($^4I_{13/2}$) + Er ($^4I_{13/2}$) → Er ($^4I_{9/2}$) + Er ($^4I_{15/2}$) are usually included in the modelling:

$$\frac{dN_{Yb,2}}{dt} = R_P - \frac{N_{Yb,2}}{\tau_{Yb}} - k_{FT} N_{Er,1} N_{Yb,2} - k_C N_{Er,2} N_{Yb,2}, \tag{9.26}$$

$$\frac{dN_{Er,2}}{dt} = -\frac{N_{Er,2}}{\tau_{Er,2}} + k_{FT} N_{Er,1} N_{Yb,2} - C_{up} N_{Er,2}^2 . \tag{9.27}$$

These rate equations (9.26) and (9.27) are solved at steady state, which for the excited Yb population gives

$$N_{Yb,2} = \frac{W_{Er,2} + C_{up} N_{Er,2}}{k_{FT} N_{Er,1}} N_{Er,2} . \tag{9.28}$$

As the cooperative upconversion is usually weak, C_{up} is set to zero and with the pump rate (9.19), $N_{Yb,1} = N_{Yb} - N_{Yb,2}$ and $N_{Er,1} = N_{Er} - N_{Er,2}$, the Er population in the upper laser level is solved from the quadratic equation

$$aN_{Er,2}^2 - bN_{Er,2} + c = 0, \tag{9.29}$$

where the constants a, b and c are given by

$$a = W_{Er,2}(k_{FT} - k_C), \tag{9.30}$$

$$b = W_{Er,2}(2W_P + W_{Yb} + k_{FT} N_{Er}) + W_P N_{Yb} k_{FT}, \tag{9.31}$$

$$c = W_P N_{Yb} k_{FT} N_{Er} . \tag{9.32}$$

In Fig. 9.6, the single-pass gain is shown versus pump power for 1 mm long Er:Yb:KYW crystals of different doping concentrations compared to Er:Yb:phosphate glass with 2.75% Er and 22% Yb. It is seen that for Er 0.5%:Yb 5%:KYW used by Kuleshov *et al.* [50], the gain is rather low with respect to present cavity losses, lower than in the Er:Yb:glass sample. These results suggest that higher Er concentrations should be used for higher gain. Even though the threshold increases, tungstate crystals are more resistant to thermal fracture than phosphate glass, allowing for higher pump powers where higher gain is achieved. This allows for out-coupling mirrors with higher transmission resulting in suppression of residual losses and higher slope efficiency. Still, due to the long Er ($^4I_{11/2}$) lifetime, significant upconversion losses are expected and the calculated gain is highly dependent on the value of the cumulative-upconversion constant k_C (here assumed to be equal to $k_{FT} = 5 \times 10^{-15}$ cm^{3}s^{-1}).

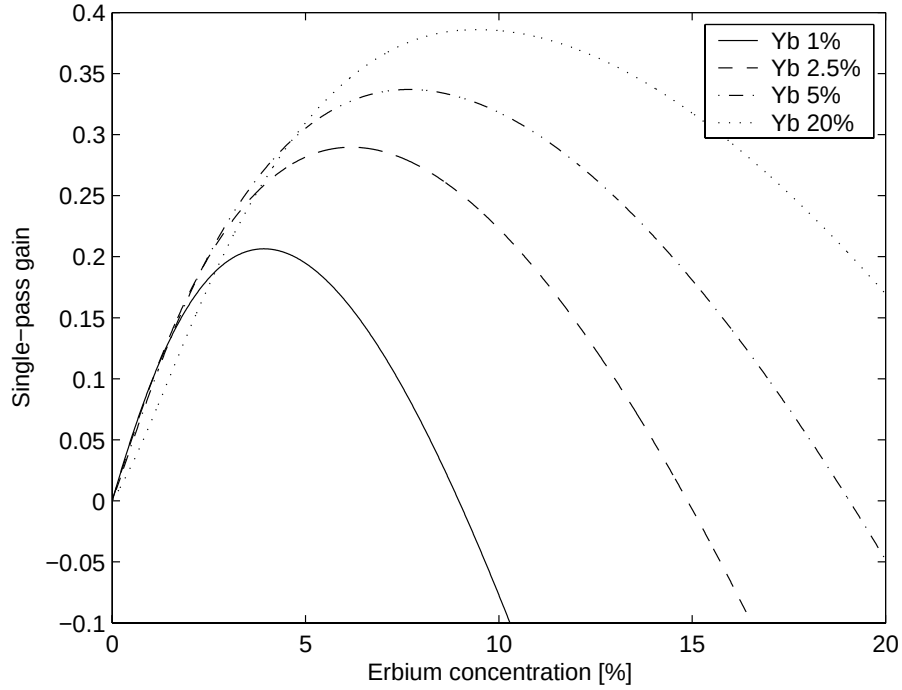

Fig. 9.5. Calculated single-pass gain in Er:Yb:KYW crystals of 1 mm thickness at 0.25 W pump power vs. Er concentration.

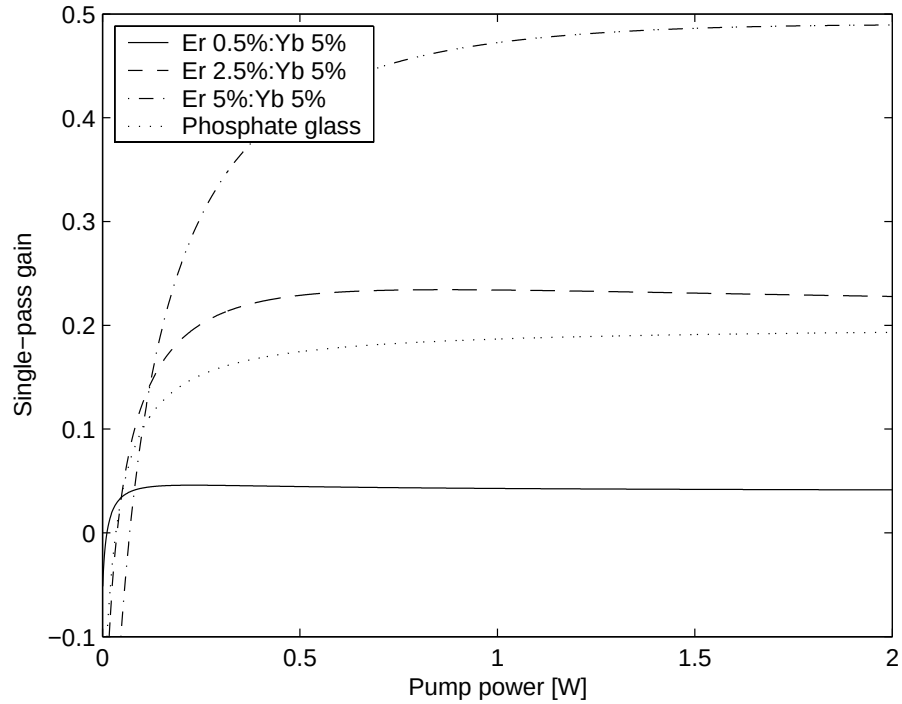

Fig. 9.6. Calculated single-pass gain in Er:Yb:KYW and Er 2.75%:Yb 22%:phosphate glass of 1 mm thickness vs. pump power.

10 Description of original work and author contribution

Paper I

Generation of blue light at 469 nm by efficient frequency doubling of a diode-pumped Nd:YAG laser

S. Bjurshagen, D. Evekull, and R. Koch, Electron. Lett. **38**, 324–325 (2002)

This paper describes a quasi-three-level Nd:YAG laser, where the 938.5 nm transition is selected by inserting a thin quartz etalon in the cavity. The achieved output power of 3.9 W was the highest reported for this laser line at that time. Single-pass extra-cavity and intracavity SHG in PPKTP generated blue light of this line for the first time at 469 nm.

Contributions by the candidate: I was responsible for the experimental work and building the laser with help from D. Evekull and assisted R. Koch in writing the manuscript.

Paper II

Efficient generation of blue light by frequency doubling of a Nd:YAG laser operating on $^4F_{3/2} \rightarrow {}^4I_{9/2}$ transitions

S. Bjurshagen, D. Evekull, and R. Koch, Appl. Phys. B **76**, 135–141 (2003).

A summary of the experiments on quasi-three-level lasers at 946 nm and 938.5 nm in Nd:YAG and their SHG to blue light in PPKTP. The thermal lensing was measured and frequency doubling was performed in both single-pass extra-cavity and intracavity configurations. A model of the laser performance in quasi-three-level lasers including ETU was developed.

Contributions by the candidate: I was responsible for the experiments and wrote the manuscript with help from D. Evekull and R. Koch.

Paper III

Modeling of energy-transfer upconversion and thermal effects in end-pumped quasi-three-level lasers

S. Bjurshagen and R. Koch, Appl. Opt. **43**, 4753–4767 (2004).

In this paper, I developed an analytical model of the output performance and thermal effects of CW quasi-three-level lasers including the influence of ETU. The results of the general output modelling were applied to a Nd laser with Gaussian beams, and the influence of pump and laser mode overlap, reabsorption loss and upconversion effects on threshold, output power and spatial distribution of the population-inversion density was studied. The influence of ETU on the fractional thermal loading was modelled and studied under lasing conditions for different mode overlaps. The model was applied to a diode-pumped laser operating at 946 nm in Nd:YAG, where the output power, thermal lensing and the degradation in beam quality were calculated.

Contributions by the candidate: I developed the models and wrote the manuscript with help from R. Koch.

Paper IV

Quasi-three-level Nd:YAG laser under diode pumping directly into the emitting level

S. Bjurshagen, R. Koch, and F. Laurell, submitted to Opt. Commun., September 2005.

Direct pumping into the emitting level at 869 nm of 946-nm Nd:YAG lasers has been investigated. We have, what we believe is for the first time, demonstrated a quasi-three-level Nd laser directly pumped by diodes and we achieved 1.6 W of output power.

Contributions by the candidate: I performed the experiments and wrote the manuscript with help from R. Koch and F. Laurell.

Paper V

Polymer encapsulated miniature Nd:YAG lasers

D. Evekull, S. Johansson, S. Bjurshagen, M. Olson, R. Koch, and F. Laurell, Electron. Lett. **39**, 1446–1448 (2003).

As it is a goal to make the lasers compact, a concept of miniature Nd:YAG lasers in micro-structured carriers has been developed at Acreo and KTH. In this paper, microchip lasers in carriers of polymer materials have been realised. An output power of 2 W at 1064 nm was achieved.

Contributions by the candidate: I assisted D. Evekull in the first experiments and helped D. Evekull, S. Johansson and R. Koch in writing the manuscript.

Paper VI

High power Q-switched Nd:YAG laser mounted in a silicon microbench

D. Evekull, J. Rydholm, S. Bjurshagen, L. Bäcklin, M. Kindlundh, L. Kjellberg, R. Koch, and M. Olson, Opt. Laser Tech. **36**, 383–385 (2004).

An optical microbench has been developed. It consists of an etched V-groove in a silicon carrier, where microchip composite-crystals diced in rhombic shapes from mirror-coated wafers are used. The composite crystals were Nd:YAG crystals diffusion-bonded with undoped end-caps at the in-coupling side and Cr:YAG saturable absorbers bonded at the out-coupling side. An average power of 2 W at 1064 nm and a pulse length of 1.4 ns were obtained.

Contributions by the candidate: I assisted D. Evekull and J. Rydholm in some of the experiments.

Paper VII

Laser performance and thermal lensing in high-power diode pumped Yb:KGW with athermal orientation

J. E. Hellström, S. Bjurshagen, and V. Pasiskevicius, submitted to Appl. Phys. B, October 2005.

Here, we report on laser experiments with Yb-doped KGW. A comparative, experimental study of the laser performance and thermal-lensing properties between standard b-cut Yb:KGW and Yb:KGW cut along a novel athermal direction was made. The results show that

the thermal lens is about two times weaker and less astigmatic in the athermal-direction-cut crystal for the same absorbed power. The weaker thermal lens also resulted in better beam quality.

Contributions by the candidate: I performed the laser experiments together with J. E. Hellström and assisted J. E. Hellström and V. Pasiskevicius in writing the manuscript.

Paper VIII

Fluorescence dynamics and rate-equations analysis in Er^{3+}, Yb^{3+} doped double tungstates

S. Bjurshagen, J. E. Hellström, V. Pasiskevicius, M.C. Pujol, M. Aguiló, and F. Díaz, submitted to Appl. Opt., November 2005.

In this paper, Er-Yb-doped KGW and KYW samples with a variety of doping concentrations have been investigated and the fluorescence dynamics have been measured for the Yb ($^2F_{5/2}$), Er ($^4I_{13/2}$) and Er ($^4S_{3/2}$) levels around 1 μm, 1.5 μm and 0.55 μm, respectively. Due to the relatively long nonradiative lifetime of the Er ($^4I_{11/2}$) level (around 150 μs in KGW and 120 μs in KYW), strong green Er ($^4S_{3/2}$) upconversion fluorescence was observed and the Yb ($^2F_{5/2}$) lifetimes are showing a decreasing trend towards the limiting Er ($^4I_{11/2}$) lifetime with increasing Er-to-Yb-concentration ratio, whereas the Er ($^4I_{13/2}$) lifetimes of around 3.5 ms are mostly unaffected by the doping concentrations. A rate equations analysis has been performed to explain the observed behaviour and the energy-transfer and back-transfer coefficients have been estimated. With these results, we have calculated gain for an eye-safe CW laser at 1534 nm with KYW crystals of different doping concentrations to find the optimum concentrations for high gain.

Contributions by the candidate: I performed the fluorescence-dynamics measurements together with J. E. Hellström and V. Pasiskevicius. I developed the rate-equation models and was responsible for the manuscript with help from V. Pasiskevicius and J. E. Hellström.

11 Conclusions

In conclusion, experimental and theoretical progress in diode-pumped rare-earth-doped solid-state lasers has been achieved. Crystals doped with the trivalent rare earth ions neodymium (Nd^{3+}), ytterbium (Yb^{3+}) and erbium (Er^{3+}) have been used, and lasers at the quasi-three-level transitions in Nd and Yb have been realised.

Nd:YAG lasers at the quasi-three-level transition at 946 nm have been built and an output power of at most 7.0 W was obtained. This is close to the highest CW power level achieved on this transition in a compact Nd:YAG rod laser (7.4 W) [90]. By inserting a thin quartz etalon in the laser cavity, the 938.5 nm laser line could be selected. An output power of 3.9 W was then obtained. This was the highest power achieved at 938.5 nm at that time. Recently, high powers on the quasi-three-level transitions in Nd:YAG in a thin-disk laser with multi-pass of the pump light have been demonstrated by Gao *et al.* [91]. 25.4 W simultaneously at 946 nm and 938.5 nm, 14 W at 946 nm only and 6 W at 938.5 nm only was then achieved.

Direct pumping into the emitting level at 869 nm of 946-nm Nd:YAG lasers has also been investigated. We have, what we believe is for the first time, demonstrated a quasi-three-level Nd laser directly pumped by diodes and we achieved 1.6 W of output power.

By using nonlinear crystals, frequency-doubling of laser light at both 946 nm and 938.5 nm was achieved. SHG of the 946 nm transition gives blue light at 473 nm. Efficient generation of blue light has been achieved in periodically poled KTP, both in single-pass and intracavity configurations. More than 0.5 W was obtained at 473 nm by intracavity doubling. Intracavity SHG of the 938.5 nm transition gave slightly more than 200 mW at 469 nm. We believe it was the first time that frequency-doubled solid-state lasers at this line were demonstrated.

An analytical model of the output performance and thermal effects of continuous-wave quasi-three-level lasers including the influence of energy-transfer upconversion has been developed. The results of the general output modelling were applied to a Nd laser with Gaussian beams, and the influence of pump and laser mode overlap, reabsorption loss and upconversion effects on threshold, output power and spatial distribution of the population-inversion density was studied. One conclusion is that the impact of upconversion is large particularly on the threshold, and that the effect is stronger for a quasi-three-level laser than for a four-level laser. The influence of ETU on the fractional thermal loading was modelled and studied under lasing conditions for different mode overlaps. Finally, the model was applied to a diode-pumped laser operating at 946 nm in Nd:YAG, where the output power, thermal lensing and the degradation in beam quality were calculated. The dependence of laser-beam size was investigated in particular, and a simple model for the degradation of laser-beam quality from a transversally varying saturated gain was proposed. The modelling of the beam quality was in very good agreement with measurements of the laser in a plane-plane cavity.

In an EU project, double-tungstate crystals like KGW and KYW have been studied. During recent years, Yb-doped double tungstates have shown efficient laser operation. At most, we obtained 9 W of CW output power from a Yb:KGW crystal. A comparative, experimental study of the laser performance and thermal-lensing properties between standard b-cut Yb:KGW and Yb:KGW cut along a novel athermal direction proposed by Biswal *et al.* [59,60] have been presented. The results show that the thermal lens is about two times weaker and less astigmatic in the athermal-direction-cut crystal for the same absorbed power. The weaker thermal lens also resulted in better beam quality.

Also, Er-Yb-doped KGW and KYW samples with a variety of doping concentrations have been investigated and the fluorescence dynamics have been measured for the Yb ($^2F_{5/2}$),

Er ($^4I_{13/2}$) and Er ($^4S_{3/2}$) levels around 1 µm, 1.5 µm and 0.55 µm, respectively. Due to the relatively long nonradiative lifetime of the Er ($^4I_{11/2}$) level (around 150 µs in KGW and 120 µs in KYW), strong green Er ($^4S_{3/2}$) upconversion fluorescence was observed and the Yb ($^2F_{5/2}$) lifetimes are showing a decreasing trend towards the limiting Er ($^4I_{11/2}$) lifetime with increasing Er-to-Yb-concentration ratio, whereas the Er ($^4I_{13/2}$) lifetimes of around 3.5 ms are mostly unaffected by the doping concentrations. A rate equations analysis has been performed to explain the observed behaviour and the energy-transfer and back-transfer coefficients have been estimated. With these results, we have calculated gain for an eye-safe CW laser at 1534 nm with KYW crystals of different doping concentrations to find the optimum concentrations for high gain. Our results suggest that higher Er concentrations should be used for high gain than in the previous Er 0.5%:Yb 5%:KYW crystal evaluated in laser experiments by Kuleshov *et al.* [50].

Appendix A

Complete set of rate equations for the populations in the nine energy levels in a neodymium-doped laser including energy-transfer upconversion (ETU), as modelled by Pollnau *et al.* [9,10] (Sect. 2.10):

$$\frac{dN_8}{dt} = -\frac{N_8}{\tau_8} + W_3 N_4^2, \tag{A.1}$$

$$\frac{dN_7}{dt} = \frac{N_8}{\tau_8} - \frac{N_7}{\tau_7} + W_2 N_4^2, \tag{A.2}$$

$$\frac{dN_6}{dt} = \frac{N_7}{\tau_7} - \frac{N_6}{\tau_6} + W_1 N_4^2, \tag{A.3}$$

$$\frac{dN_5}{dt} = R_{05} r_P + \frac{N_6}{\tau_6} - \frac{N_5}{\tau_5}, \tag{A.4}$$

$$\frac{dN_4}{dt} = \frac{N_5}{\tau_5} - \frac{N_4}{\tau_4} - \frac{c\sigma}{n} \Delta N \Phi \phi_0 - 2(W_1 + W_2 + W_3) N_4^2, \tag{A.5}$$

$$\frac{dN_3}{dt} = \beta_{43} \frac{N_4}{\tau_4} - \frac{N_3}{\tau_3} + W_1 N_4^2, \tag{A.6}$$

$$\frac{dN_2}{dt} = \beta_{42} \frac{N_4}{\tau_4} + \frac{N_3}{\tau_3} - \frac{N_2}{\tau_2} + W_2 N_4^2, \tag{A.7}$$

$$\frac{dN_1}{dt} = \beta_{41} \frac{N_4}{\tau_4} + \frac{N_2}{\tau_2} - \frac{N_1}{\tau_1} + \frac{c\sigma}{n} \Delta N \Phi \phi_0 + W_3 N_4^2, \tag{A.8}$$

$$N_d = \sum_{i=0}^{8} N_i, \tag{A.9}$$

where $\beta_{ij} = \tau_i / \tau_{ij}$ are the branching ratios and W_1, W_2 and W_3 are the rate parameters for the three upconversion processes. Equation (A.9) indicates conservation of the doping concentration N_d.

References

[1] T. Y. Fan and R. Byer, "Continuous-wave operation of a room-temperature, diode-laser-pumped, 946-nm Nd:YAG laser," Opt. Lett. **12**, 809–811 (1987).

[2] W. P. Risk and W. Length, "Room-temperature, continuous-wave, 946-nm Nd:YAG laser pumped by laser-diode arrays and intracavity frequency doubling to 473 nm," Opt. Lett. **12**, 993–995 (1987).

[3] P. Zeller and P. Peuser, "Efficient, multiwatt, continuous-wave laser operation on the $^4F_{3/2} \rightarrow {}^4I_{9/2}$ transitions of Nd:YVO_4 and Nd:YAG," Opt. Lett. **25**, 34–36 (2000).

[4] C. Czeranowsky, E. Heumann, and G. Huber, "All-solid-state continuous-wave frequency-doubled Nd:YAG–BiBO laser with 2.8-W output power at 473 nm," Opt. Lett. **28**, 432–434 (2003).

[5] W. P. Risk, T. R. Gosnell, and A. V. Nurmikko, *Compact Blue-Green Lasers* (Cambridge University Press, Cambridge, 2003).

[6] Y. Guyot, H. Manan, J. Y. Rivoire, R. Moncorgé, N. Garnier, E. Descroix, M. Bon, and P. Laporte, "Excited-state-absorption and upconversion studies of Nd^{3+}-doped single crystals $Y_3Al_5O_{12}$, $YLiF_4$ and $LaMgAl_{11}O_{19}$," Phys. Rev. B **51**, 784–799 (1995).

[7] T. Chuang and H. R. Verdún, "Energy-transfer up-conversion and excited-state absorption of laser-radiation in Nd:YLF laser crystals," IEEE J. Quantum Electron. **32**, 79–91 (1996).

[8] S. Guy, C. L. Bonner, D. P. Shepherd, D. C. Hanna, A. C. Tropper, and B. Ferrand, "High-inversion densities in Nd:YAG: upconversion and bleaching," IEEE J. Quantum Electron. **34**, 900–909 (1998).

[9] M. Pollnau, P. J. Hardman, W. A. Clarkson, and D. C. Hanna, "Upconversion, lifetime quenching, and ground-state bleacing in Nd^{3+}:$LiYF_4$," Opt. Commun. **147**, 203–211 (1998).

[10] M. Pollnau, P. J. Hardman, M. A. Kern, W. A. Clarkson, and D. C. Hanna, "Upconversion-induced heat generation and thermal lensing in Nd:YLF and Nd:YAG," Phys. Rev. B **58**, 16076–16092 (1998).

[11] P. J. Hardman, W. A. Clarkson, G. J. Friel, M. Pollnau, and D. C. Hanna, "Energy-transfer upconversion and thermal lensing in high-power end-pumped Nd:YLF laser crystals," IEEE J. Quantum Electron. **35**, 647–655 (1999).

[12] A. E. Siegman, *Lasers* (University Science, Mill Valley, Calif., 1986).

[13] A. Yariv, *Quantum Electronics* 3rd edn. (John Wiley & Sons, New York, 1989).

[14] W. Koechner, *Solid-State Laser Engineering* 5th edn. (Springer, Berlin, 1999).

[15] W. P. Risk, "Modeling of longitudinally pumped solid-state lasers exhibiting reabsorption losses," J. Opt. Soc. Am. B **5**, 1412–1423 (1988).

[16] K. Kubodera and K. Otsuka, "Single-transverse-mode $LiNdP_4O_{12}$ slab waveguide laser," J. Appl. Phys. **50**, 653–659 (1979).

[17] W. A. Clarkson and D. C. Hanna, "Effects of transverse-mode profile on slope efficiency and relaxation oscillations in a longitudinally-pumped laser," J. Mod. Opt. **27**, 483–498 (1989).

[18] T. Y. Fan and R. L. Byer, “Modelling and CW operation of a quasi-three-level 946 nm Nd:YAG laser,” IEEE J. Quantum Electron. **23**, 605–612 (1987).

[19] T. Taira, W. M. Tulloch, and R. L. Byer, “Modelling of quasi-three-level lasers and operation of cw Yb:YAG lasers,” Appl. Opt. **36**, 1867–1874 (1997).

[20] Y. F. Chen, Y. P. Lan, and S. C. Wang, “Influence of energy-transfer upconversion on the performance of high-power diode-end-pumped CW lasers,” IEEE J. Quantum Electron. **36**, 615–619 (2000).

[21] Y. F. Chen, “Pump-to-mode size ratio dependence of thermal loading in diode-end-pumped solid-state lasers,” J. Opt. Soc. Am. B **17**, 1835–1840 (2000).

[22] C. Pfistner, R. Weber, H. P. Weber, S. Merazzi, and R. Gruber, “Thermal beam distortions in end-pumped Nd:YAG, Nd:GSGG, and Nd:YLF rods,” IEEE J. Quantum Electron. **30**, 1605–1615 (1994).

[23] S. C. Tidwell, J. F. Seamans, M. S. Bowers, and A. K. Cousins, “Scaling CW diode-end-pumped Nd:YAG lasers to high average powers,” IEEE J. Quantum Electron. **28**, 997–1009 (1992).

[24] A. K. Cousins, “Temperature and thermal stress scaling in finite-length end-pumped laser rods,” IEEE J. Quantum Electron. **28**, 1057–1068 (1992).

[25] M. E. Innocenzi, H. T. Yura, C. L. Fincher, and R. A. Fields, “Thermal modeling of continous-wave end-pumped solid-state lasers,” Appl. Phys. Lett. **56**, 1831–1833 (1990).

[26] P. F. Moulton, “An investigation of the Co:MgF, laser system,” IEEE J. Quantum Electron. **21**, 1582–1595 (1985).

[27] S. Singh, R. G. Smith, and L. G. Van Uitert, “Stimulated-emission cross section and fluorescent quantum efficiency of Nd^{3+} in yttrium aluminum garnet at room temperature,” Phys. Rev. B **10**, 2566–2572 (1974).

[28] J. Frauchiger, P. Albers, and H. P. Weber, “Modelling of thermal lensing and higher order ring mode oscillation in end-pumped CW Nd:YAG lasers,” IEEE J. Quantum Electron. **28**, 1046–1056 (1992).

[29] A. E. Siegman, “Analysis of laser beam quality degradation caused by quartic phase aberrations,” Appl. Opt. **32**, 5893–5901 (1993).

[30] N. Hodgson and H. Weber, *Optical Resonators* (Springer, Berlin, 1996).

[31] T. Y. Fan, “Aperture guiding in quasi-three-level lasers,” Opt. Lett. **19**, 554–556 (1994).

[32] R. Koch, W. A. Clarkson, and D. C. Hanna, “Diode pumped CW Nd:YAG laser operating at 938.5 nm,” Electron. Lett. **32**, 553–554 (1996).

[33] R. Lavi, S. Jackel, Y. Tzuk, M. Winik, E. Lebiush, M. Katz, and I. Paiss, “Efficient pumping scheme for neodymium-doped materials by direct excitation of the upper lasing level,” Appl. Opt. **38** 7382–7385 (1999).

[34] R. Lavi and S. Jackel, “Thermally boosted pumping of neodymium lasers,” Appl. Opt. **39**, 3093–3098 (2000).

[35] R. Lavi, S. Jackel, A. Tal, E. Lebiush, Y. Tzuk, and S. Goldring, “885 nm high-power diodes end-pumped Nd:YAG laser,” Opt. Commun. **195**, 427–430 (2001).

[36] V. Lupei, N. Pavel, and T. Taira, "1064 nm laser emission of highly doped Nd: Yttrium aluminum garnet under 885 nm diode laser pumping," Appl. Phys. Lett. **80**, 4309–4311 (2002).

[37] V. Lupei, G. Aka, and D. Vivien, "Quasi-three-level 946 nm CW laser emission of Nd:YAG under direct pumping at 885 nm into the emitting level," Opt. Commun. **204**, 399–405 (2002).

[38] V. Lupei, N. Pavel, and T. Taira, "Highly efficient continuous-wave 946-nm Nd:YAG laser emission under direct 885-nm pumping," Appl. Phys. Lett. **81**, 2677–2679 (2002).

[39] H. Karlsson, *Fabrication of periodically poled crystals from the KTP family and their applications in nonlinear optics*, Phd Thesis, TRITA-FYS 2197 (Royal Institute of Technology, Stockholm, 1999).

[40] J. Hellström, *Nanosecond optical parametric oscillators and amplifiers based on periodically poled $KTiOPO_4$*, Phd Thesis, TRITA-FYS 2001:5, ISBN 91-7283-214-2 (Royal Institute of Technology, Stockholm, 2001).

[41] G. D. Boyd and D. A. Kleinman, "Parametric interaction of focused Gaussian light beams," J. Appl. Phys. **39**, 3597–3639 (1968).

[42] M. M. Fejer, G. A. Magel, D. H. Jundt, and R. L. Byer, "Quasi-phase-matched second harmonic generation: tuning and tolerances," IEEE J. Quantum Electron. **28**, 2631–2654 (1992).

[43] T. Baer, "Large-amplitude fluctuations due to longitudinal mode coupling in diode-pumped intracavity-doubled Nd:YAG lasers," J. Opt. Soc. Am. B **3**, 1175–1180 (1986).

[44] J. J. Zayhowski and A. Mooradian, "Single-frequency microchip Nd lasers," Opt. Lett. **14**, 24–26 (1989).

[45] Å. Claesson, J. Holm, R. Koch, M. Olson, A. Olsson, C. Vieder, H. Åhlfeldt, and F. Laurell, "Diode-pumped miniature lasers using microstructured silicon carriers," Electron. Lett. **36**, 433–434 (2000).

[46] R. Solé, V. Nikolov, X. Ruiz, Jna. Gavaldà, X. Solans, M. Aguiló, and F. Díaz, "Growth of β-$KGd_{1-x}Nd_x(WO_4)_2$ single crystals in $K_2W_2O_7$ solvents," J. Cryst. Growth **169**, 600–603 (1996).

[47] M. C. Pujol, R. Solé, J. Massons, Jna. Gavaldà, X. Solans, C. Zaldo, F. Díaz, and M. Aguiló, "Structural study of monoclinic $KGd(WO_4)_2$ and effects of lanthanide substitution," J. Appl. Cryst. **34**, 1–6 (2001).

[48] S. V. Borisov and R. F. Kletsova, "Crystal structure of $KY(WO_4)_2$," Sov. Phys. Cryst. **13**, 517–519 (1968).

[49] M. C. Pujol, X. Mateos, R. Solé, J. Massons, Jna. Gavaldà, X. Solans, F. Díaz, and M. Aguiló, "Structure, crystal growth and physical anisotropy of $KYb(WO_4)_2$, a new laser matrix," J. Appl. Cryst. **35**, 108–112 (2002).

[50] N. V. Kuleshov, A. A. Legatsky, V. G. Scherbitsky, E. Heumann, T. Jensen, A. Diening, and G. Huber, "CW laser performance of Yb and Er,Yb doped tungstates," Appl. Phys. B **64**, 409–413 (1997).

[51] A. A. Lagatsky, N. V. Kuleshov, and V. P. Mikhailov, "Diode-pumped CW lasing of Yb:KYW and Yb:KGW," Opt. Commun. **165**, 71–75 (1999).

[52] A. Brenier, “A new evaluation of Yb^{3+}-doped crystals for laser applications,” J. of Luminesc. **92**, 199–204 (2001).

[53] A. Brenier and G. Boulon, “Overview of the best Yb^{3+}-doped laser crystals,” J. of Alloys and Comp. **323–324**, 210–213 (2001).

[54] P. Klopp, V. Petrov, U. Griebner, and G. Erbert, “Passively mode-locked Yb:KYW laser pumped by a tapered diode laser,” Opt. Express **10**, 108–113 (2002).

[55] H. Liu, J. Nees, and G. Mourou, “Diode-pumped Kerr-lens mode-locked $YbKY(WO_4)_2$ laser,” Opt. Lett. **26**, 1723–1725 (2001).

[56] M. C. Pujol, M. A. Bursukova, F. Güell, X. Mateos, R. Solé, Jna. Gavaldà, M. Aguiló, J. Massons, F. Díaz, P. Klopp, U. Griebner, and V. Petrov, “Growth, optical characterization, and laser operation of a stoichiometric crystal $KYb(WO_4)_2$,” Phys. Rev. B **65**, 165121-1–165121-11 (2002).

[57] A. Beyertt, D. Nickel, and A. Giesen, “Femtosecond thin-disk Yb:KYW regenerative amplifier,” Appl. Phys. B **80**, 655–660 (2005).

[58] S. Chénais, F. Druon, F. Balembois, G. Lucas-Leclin, P. Georges, A. Brun, M. Zavelani-Roosi, F. Augé, J. P. Chambaret, G. Aka, and D. Vivien, “Multiwatt, tunable diode-pumped CW Yb:GdCOB laser,” Appl. Phys. B **72**, 389–393 (2001).

[59] S. Biswal, S. P. O’Connor, and S. R. Bowman, “Thermo-optical parameters measured in potassium-gadolinium-tungstate,” in *Technical Digest of Conference on Lasers and Electro-Optics* (San Francisco, Calif., 2004), paper CThT62.

[60] S. Biswal, S. P. O’Connor, and S. R. Bowman, “Thermo-optical parameters measured in ytterbium-doped potassium gadolinium tungstate,” Appl. Opt. **44**, 3093–3097 (2005).

[61] M. C. Pujol, M. Rico, C. Zaldo, R. Solé, V. Nikolov, X. Solans, M. Aguiló, and F. Díaz, “Crystalline structure and optical spectroscopy of Er^{3+}-doped $KGd(WO_4)_2$ single crystals,” Appl. Phys. B **68**, 187–197 (1999).

[62] J. Zhang, K. Wang, J. Wang, H. Zhang, W. Yu, X. Wang, Z. Wang, Q. Lu, M. Ba, D. G. Ran, Z. C. Ling, and H. R. Xia, “Anisotropic thermal properties of monoclinic $Yb:KLu(WO_4)_2$ crystals,” Appl. Phys. Lett. **87**, 061104-1–061104-3 (2005).

[63] G. Karlsson, *Diode-pumped Er-Yb lasers for eye-safe applications*, Phd Thesis, TRITA-FYS 2003:2, ISBN 91-7283-455-2 (Royal Institute of Technology, Stockholm, 2003).

[64] G. Karlsson, V. Pasiskevicius, F. Laurell, J. A. Tellefsen, B. Denker, B. I. Galagan, V. Osiko, and S. Sverchkov, “Diode-pumped Er-Yb:glass laser passively Q-switched by use of $Co^{2+}:MgAl_2O_4$ as a saturable absorber,” Appl. Opt. **39**, 6188–6192 (2000).

[65] G. Karlsson, F. Laurell, J. Tellefsen, B. Denker, B. Galagan, V. Osiko, and S. Sverchkov, “Development and characterization of Yb-Er laser glass for high average power laser diode pumping,” Appl. Phys. B **75**, 1–6 (2002).

[66] G. Karlsson, V. Pasiskevicius, F. Laurell, and J. A. Tellefsen, “Q-switching of an Er-Yb:glass microchip laser using an acousto-optical modulator,” Optics Commun. **217**, 317–327 (2003).

[67] B. Denker, B. Galagan, L. Ivleva, V. Osiko, S. Sverchkov, I. Voronina, J.E. Hellström, G. Karlsson, and F. Laurell, “Luminescent and laser properties of Yb–$Er:GdCa_4O(BO_3)_3$: a new crystal for eye-safe 1.5-μm lasers,” Appl. Phys. B **79**, 577–581 (2004).

[68] J. E. Hellström, G. Karlsson, V. Pasiskevicius, F. Laurell, B. Denker, S. Sverchkov, B. Galagan, and L. Ivleva, "Passive Q-switching at 1.54 μm of an Er–Yb:$GdCa_4O(BO_3)_3$ laser with a CO^{2+}:$MgAl_2O_4$ saturable absorber," Appl. Phys. B **81**, 49–52 (2005).

[69] P. A. Burns, J. M. Dawes, P. Dekker, J. A. Piper, H. Jiang, and J. Wang, "Optimization of Er, Yb:YCOB for CW laser operation," IEEE J. Quantum Electron. **40**, 1575–1582 (2004).

[70] M.. Rico, M. C. Pujol, X. Mateos, J. Massons, C. Zaldo, M. Aguilló, and F. Díaz, "Yb sensitising of Er^{3+} up-conversion emission in $KGd(WO_4)_2$:Er:Yb single crystals," J. Alloys and Comp. **323–324**, 362–366 (2001).

[71] N. V. Kuleshov, A. A. Legatsky, A.V. Podlipensky, V. P. Mikhailov, A. A. Kornienko, E. B. Dunina, S. Hartung, and G. Huber, "Fluorescence dynamics, excited-state absorption and stimulated emission of Er^{3+} in $KY(WO_4)_2$," J. Opt. Soc. Am. B **15**, 1205–1212 (1998).

[72] C. B. Layne, W. H. Lowdermilk, and M. J. Weber, "Multiphonon relaxation of rare-earth ions in oxide glasses," Phys. Rev. B **16**, 10–20 (1977).

[73] F. Mougel, G. Aka, A. Kahn-Harari, H. Hubert, J. M. Benitez, and D. Vivien, "Infrared laser performance and self-frequency doubling of Nd^{3+}:$Ca_4GdO(BO_3)_3$ (Nd:GdCOB)," Opt. Mater. **8**, 161–173 (1997).

[74] A. Lupei, G. Aka, E. Antic-Fidancev, B. Viana, D. Vivien, and P. Aschehoug, "Selective excitation study of Yb^{3+} in $GdCa_4O(BO_3)_3$ and $YCa_4O(BO_3)_3$," J. Physics: Cond. Matter **14**, 1107–17 (2002).

[75] L. Macalik, J. Hanuza, and A. A. Kaminskii, "Polarized infrared and Raman spectra of $KGd(WO_4)_2$ and their interpretation based on normal coordinate analysis," J. Raman Spectrosc. **33**, 92–103 (2002).

[76] J. Hanuza and L. Macalik, "Polarized infra-red and Raman spectra of monoclinic α-$KLn(WO_4)_2$ single crystals (Ln = Sm–Lu, Y)," Spectrochim. Acta **43A**, 361–373 (1987).

[77] M. Pollnau, D. R. Gamelin, S. R. Lüthi, H. U. Güdel, M. P. Hehlen, "Power dependence of upconversion luminescence in lanthanide and transition-metal-ion systems," Phys. Rev. B **61**, 3337–3346 (2000).

[78] J. F. Suyver, A. Aebischer, S. García-Revilla, P. Gerner, and H. U. Güdel, "Anomalous power dependence of sensitized upconversion luminescence," Phys. Rev. B **71**, 125123-1–125123-9 (2005).

[79] D. S. Sumida and T. Y. Fan, "Effect of radiation trapping on fluorescence lifetime and emission cross section measurements in solid-state laser media," Opt. Lett **19**, 1343–1345 (1994).

[80] C. D. Marshall, S. A Payne, L. K. Smith, H. T. Powell, W. F. Krupke, and B. H. T. Chai, "1.047-μm Yb:$Sr_5(PO_4)_3F$ energy storage optical amplifier," IEEE J. Quantum Electron **1**, 67–77 (1995).

[81] R. Peters, J. Johannsen, M. Mond, K. Petermann, and G. Huber, "Yb:$NaGd(WO_4)_2$: spectroscopic characterisation and laser demonstration," in *Conference Digest of CLEO/Europe-EQEC* (Munich, Germany, 2005), paper CA9-4-TUE.

[82] L. F. Johnson, H. J. Guggenheim, T. C. Rich, and F. W. Ostermayer, "Infrared-to-visible conversion by rare-earth ions in crystals," J. Appl. Phys. **43**, 1125–1137 (1972).

[83] J. A. Hutchinson, H. R. Verdun, B. H. T. Chai, B. Zandi, and L. D. Merkle, "Spectroscopic evaluation of $CaYAlO_4$ doped with trivalent Er; Tm, Yb and Ho for eyesafe laser applications," Opt. Mater. **3**, 287–306 (1994).

[84] B. Simondi-Teisseire, B. Viana, D. Vivien, and A. M. Lejus, "Yb^{3+} to Er^{3+} energy transfer and rate-equations formalism in the eye safe laser material Yb:Er:$Ca_2Al_2SiO_7$," Opt. Mater. **6**, 267–274 (1996).

[85] X. Han, G. Wang, and T. Tsuboi, "Growth and spectral properties of Er^{3+}/Yb^{3+}-codoped $KY(WO_4)_2$ crystal," J. Crystal Growth **242**, 412–420 (2002).

[86] X. Mateos, R. Solé, Jna. Gavaldà, M. Aguiló, J. Massons, and F. Díaz, "Crystal growth, optical and spectroscopic characterisation of monoclinic $KY(WO_4)_2$ co-doped with Er^{3+} and Yb^{3+}," Opt. Mater., available online June 2005.

[87] P. Laporta, S. Longhi, S. Taccheo, and O. Svelto "Analysis and modelling of the erbium-ytterbium glass laser," Opt. Commun. **100**, 311–321 (1993).

[88] S. Taccheo, P. Laporta, S. Longhi, O. Svelto, and C. Svelto "Diode-pumped bulk erbium-ytterbium lasers," Appl. Phys. B **63**, 425–436 (1996).

[89] E. Tanguy, C. Larat, and J. P. Pocholle, "Modelling of the erbium–ytterbium laser," Opt. Commun. **153**, 172–183 (1998).

[90] M. Abraham, A. Bar-Lev, H. Epshtein, A. Goldring, Y. Zimmerman, E. Lebiush, and R. Lavi, "7.4W CW output power of Nd:YAG laser radiation at 946nm and 500mW of 473nm laser by extra cavity doubling using periodically poled KTP," in *Technical Digest of Advanced Solid-State Lasers*, (Seattle, Washington, 2001), pp. 357–359.

[91] J. Gao, J. Speiser, and A. Giesen, "25-W diode-pumped continuous-wave quasi-three-level Nd:YAG thin disk laser," in *Technical Digest of Advanced Solid-State Photonics*, (Vienna, Austria, 2005), paper TuB34.